Stony Brook University

Application of Lattice Boltzmann Methods in Complex Mass Transfer Systems

A Dissertation Presented

by

Ning Sun

to

The Graduate School

in Partial Fulfillment of the

Requirements

for the Degree of

Doctor of Philosophy

in

Materials Science and Engineering

Stony Brook University

May 2016

Stony Brook University

The Graduate School

Ning Sun

We, the dissertation committee for the above candidate for the

Doctor of Philosophy degree, hereby recommend

acceptance of this dissertation.

Dilip Gersappe – Dissertation Advisor
Professor, Graduate Program Director, Department of Materials Science and Engineering

T.A. Venkatesh - Chairperson of Defense
Associate Professor, Department of Materials Science and Engineering

Amy Marschilok
Research Associate Professor, Department of Materials Science and Engineering

Alexej Jerschow
Professor, Director of Undergraduate Studies, Chemistry Department, New York University

This dissertation is accepted by the Graduate School

Charles Taber
Dean of the Graduate School

Abstract of the Dissertation

Application of Lattice Boltzmann Methods in Complex Mass Transfer Systems

by

Ning Sun

Doctor of Philosophy

in

Materials Science and Engineering

Stony Brook University

2016

Lattice Boltzmann Method (LBM) is a novel computational fluid dynamics method that can easily handle complex and dynamic boundaries, couple local or interfacial interactions/reactions, and be easily parallelized allowing for simulation of large systems. While most of the current studies in LBM mainly focus on fluid dynamics, however, the inherent power of this method makes it an ideal candidate for the study of mass transfer systems involving complex/dynamic microstructures and local reactions. In this thesis, LBM is introduced to be an alternative computational method for the study of electrochemical energy storage systems (Li-ion batteries (LIBs) and electric double layer capacitors (EDLCs)) and transdermal drug design on mesoscopic scale. Based on traditional LBM, the following in-depth studies have been carried out:

(1) For EDLCs, the simulation of diffuse charge dynamics is carried out for both the charge and the discharge processes on 2D systems of complex random electrode geometries (pure random, random spheres and random fibers). Steric effect of concentrated solutions is considered by using modified Poisson-Nernst-Plank (MPNP) equations and compared with regular Poisson-Nernst-Plank (PNP) systems. The effects of electrode microstructures (electrode density, electrode filler morphology, filler size, etc.) on the net charge distribution and charge/discharge time are studied in detail. The influence of applied potential during discharging process is also discussed.

(2) For the study of dendrite formation on the anode of LIBs, it is shown that the Lattice Boltzmann model can capture all the experimentally observed features of microstructure evolution at the anode, from smooth to mossy to dendritic. The mechanism of dendrite formation process in mesoscopic scale is discussed in detail and compared with the traditional Sand's time theories. It shows that dendrite formation is closely related to the inhomogeneous reactively at the electrode-electrolyte interface. When the inhomogeneity is small, dendrites form mainly under high current densities, in which the mass transfer is dominated by electromigration; when the inhomogeneity is very large, dendrites may form under both high and low current densities, which is dominated by electromigration in high current density and by surface reactivity in low current density. We show that the critical current density for dendrite formation is sensitive to

surface inhomogeneous reactivity and the onset time of dendrite formation is sensitive to the initial roughness of electrode. A new analysis method is introduced, which can predict the formation of dendrites in batteries at a very early stage even before large dendrites form. Charge/discharge cyclic properties of the system are also studied, which shows that electrode roughness will increase during cycles and the break-off of dendritic structures is inevitable once big dendrites form; however, it is possible to minimize the amount of break-off materials by optimizing the rate of discharge.

(3) The LBM is also used to simulate intercalation reactions in a Li-Ion battery with graphite as anode and pure Li metal as counter electrode. Both galvanostatic and potentiostatic conditions were studied. The relation between operation parameters (current and potential) and electrode parameters (porosity, thickness and diffusivity) and plating times were discussed. Different equilibrium potentials forms (empirical fitting, fitting of SONY 18650 cell, and staged profiles) were also compared. By modifying the morphology of electrode with a density gradient, it was shown that much better electrode performance can be obtained, which can be helpful for the designing and manufacturing of better batteries.

(4) The transdermal drug delivery system is also simulated by using LBM. Two kinds of transdermal structures are discussed: "brick and mortar" structure and a simple homogenized structure. It is demonstrated that the homogenized system is able to obtain similar steady state flux as the "brick and mortar" structure; however, in the early transient region, their flux value can be different. The influence of different system parameters (amount of drug in patch, patch thickness, partition coefficient at patch/ Stratum Corneum (SC) interface, and the diffusion coefficient of drug in each component) is discussed in details. It turns out that in this system, the rate-determine step for mass transfer should be the partition between patch and SC layers and the diffusion in the SC layer. The influence of enhancer is also tested. It is shown that by adding enhancers, the drug flux can be significantly increased. However, the peak time of drug does not necessarily match the peak flux time of enhancer. The peak time of drug could be adjusted (pushed earlier or dragged later) by using different kinds of enhancers, which has higher/smaller diffusivity than drug in the SC layer.

Table of Contents

List of Tables

Chapter 5

Chapter 6

List of Figures

Chapter 2

Chapter 3

Chapter 4

Chapter 5

Chapter 6

List of Abbreviations

Bhatnagar–Gross–Krook	BGK
Boltzmann Equation	BE
Boltzmann Transport Equation	BTE
Butler-Volmer Equation	BVE
Computational Fluid Dynamics	CFD
Electric Double Layer	EDL
Electric Double Layer Capacitor	EDLC
Electric Vehicle	EV
Equilibrium Distribution Function	EDF
Finite Difference Method	FDM
Finite Element Method	FEM
Finite Volume Method	FVM
Laplace Transform Method	LTM
Lattice Boltzmann	LB
Lattice Boltzmann Method	LBM
Lattice Gas Automata	LGA
Li-ion Battery	LIB
Meso Carbon Micro Beads	MCMB
Modified Poisson-Nernst-Plank	MPNP
Molecular Dynamics	MD
Monte Carlo	MC
Open-Circuit Potential	OCP
Partial Differential Equation	PDE

Poisson-Boltzmann	PB
Poisson-Nernst-Plank	PNP
Random Walk Method	RWM
Solid Electrolyte Interphase	SEI
Stratum Corneum	SC

List of Symbols

f	distribution function
D	ambipolar diffusion constant for the salt
t_a	anionic transport number
V_{ext}, V_{app}	applied potential
k	Boltzmann constant
e	charge of an electron
z_i	charge on species i
$\boldsymbol{\Omega}$	collision operator
ρ_{out}	concentration at outflux boundary
c_s	concentration of lithium in solid phase
c_i	concentration of species i
σ_j	conductivtiy of species j
J^*	crossover current density
J	current density
$\boldsymbol{K}$	curvature constant
λ_D	Debye length
J_{dep}	deposition current density
ε_0	dielectric constant in vacuum
D_i	diffusion constant of species i
J_{diff}	diffusion limiting current density
J_{diss}	disoultion current density
f_i	distribution function in i^{th} direction
μ_j	electrical mobility of species j
ψ	electrical potential
$\Delta\mu_e$	electrochemical potential change in the electrons
C^{eq}	equilibirun concentration at potential of 0
f^{eq}	equilibrium distribution function
f_i^{eq}	equilibrium distribution function in i^{th} direction
V_{eq}	equilibrium potential
E_p^{eq}	equilibrium potential for plating at open-circuit condition
i_0^{eq}	exchange current density at open-circuit condition
$\boldsymbol{F}$	external force
$\boldsymbol{F_i}$	external force in i^{th} direction
F	Faradic constant
$\boldsymbol{j}$, $\boldsymbol{J}$	Flux
J_{trans}	flux in transverse direction
H	H-function (entropy)

R	ideal gas constant
c_0	initial concentration
ε	Knudsen number / dielectric constant / relative dielectri constant
v_i	lattice velocity in i^{th} direction
C_c	local concentration at interface
C_{en}	local concentration of enhancer
Φ, ρ	local density of particles
Φ	local electrical potential
i_0	local exchange current density
f_S	local solid fraction
$\boldsymbol{u}$	macriscopic velocity / advective velocity / electric permittivity
m	Mass
c_t	maximum concentration in intercalation material
V_M	molar volume of metal
$\boldsymbol{p}$	momenta
$\boldsymbol{p_i}$	momenta in i^{th} direction
q_s	net charge at electrode-electrolyte interface
ρ_f	net charge density
δ	normalized effective thickness of the surface insulating layer
N	number of particles
δ_t	one time step
η	overpotential
η_p	overpotential for plating
$\boldsymbol{c}$	particle velocity
$\boldsymbol{r}$	position vector
k	reaction speed constant
τ	relaxation time / Sand's time
S	source term
c_s	speed of sound in lattice
E	state of energy
υ	steric effects / normalized apply potential
κ	surface curvature
γ	surface energy
σ	surface roughness / conductivity
α_1, α_2	symmetry factors
L	system size
ly	system size in y direction
T	temperature

t	Time
q_a	total net charge (positive) in the whole electrolyte
$\boldsymbol{e}_i$	velocity vector in i^{th} direction of a lattice
ω_i , t_i	weight in the i^{th} direction in a lattice

**Bold italic symbols are vectors*

Acknowledgments

First and foremost, I would like to express my special appreciation and thanks to my Ph.D. advisor, Prof. Dilip Gersappe, who has been a tremendous mentor for me. His wide knowledge and helpful guidance is priceless for me in both academic research and my career. He is also a very kind friend who always encourages me to do the things that I'm interested in.

Second, I would like to thank my parents in China, who are always there for me, support me, and share all the joys and sorrows with me during my whole life.

I would also like to thank Prof. Clare P. Grey in University of Cambridge and Prof. Alexej Jerschow in New York University for their precious discussion in the dendrite formation project. Also, the collaborations with their students and postdoctoral researchers, Hee Jung Chang, Andrew J. Ilott, and Nicole M. Trease, provide me with lots of insights in both the experiment and the theories.

I would like to thank Zhiwei Zhang in RES Group, Inc. for his useful discussion in the transdermal drug delivery system. The collaborations with the RES Group, Inc. on several projects give me the opportunity to practice my knowledge in the industrial field.

I would also like to thank Prof. Alexej Jerschow, Prof. Amy Marschilok and Prof. T.A. Venkatesh for being my dissertation committee members and their valuable advice on my thesis.

I would like to thank my colleagues in our group: Dr. Joseph Ortiz, Di Xu, and Jiangjiao Long for their help and discussion during my research.

During my Ph.D. study, my housemates give me lots of help and we shared lots of happy time together so that I never feel lonely even though I'm thousands miles far away from home. Thanks to them and we will be good friends forever.

I would also like to thank all the financial support for my research. Thanks to the Institute for Advanced Computation Science (IACS) in Stony Brook University for providing me with abundant computation time. Also thanks to the developers of the open source software Palabos, which is the main software package that I'm using in my study.

Last but not least, the deepest appreciation goes to my best friend, soul mate, and love - Yupeng, who is the best person out there for me. Even though most of the time we are separated apart physically, he is always sticking by my side to encourage me, help me and care about me. I know he is always there for me. Thanks for being in my life, and more importantly, thanks for sharing the rest of life together with me to the fullest.

Publications

1. Modeling Tablet Dissolution in Complex Hydrodynamic Environments, **Ning Sun**, Arpon Raksit, Taeshin Park, Glen H. Ko, and Dilip Gersappe, *J. Chem. Biol. Interfaces*, (**2**)1-11, **2014**

Chapter 1. Introduction

Mass transfer, known as a "non-equilibrium" dynamic process, is one of the most commonly observed phenomena in our daily lives. The examples of mass transfer problems are diffusion of mass according to concentration gradient, electromigration of charged particles in electric field, fluid flows, etc. The dynamics involving these processes are usually very complicated, particularly when combined with external fields, complex geometries, moving boundaries, interactions and reactions both at the interfaces and in the bulk phases. From an experimental point of view, these systems represent several challenges as they require the ability to follow the mass transport in complex environments while following all the different reactions and changes in the local environment. "Operando" type analysis has resulted in the ability to follow these different effects simultaneously, but these studies could be significantly enhanced by the development of computational methods for these complex systems, In this thesis, we develop mesoscopic computational methods to look systems where mass transfer is critical to the operation of the device. We focus mainly on energy related applications, such as supercapacitors and batteries, but to show the range of our method, we also apply it to transport in biomedical systems, and study the transport of drugs in transdermal patches.

The most commonly developed numerical methods to solve the mass transfer problems can usually be divided into two: macroscopic scale simulation, such as conventional Computational Fluid Dynamics (CFD)[1, 2], and atomistic scale simulation, such as Molecular Dynamics (MD) and direct simulation Monte Carlo (MC))[3]. In conventional CFD, the continuum fluid mechanics are described by a set of partial differential equations (PDEs), and the state of the system is obtained by solving such PDEs under different discretization methods, such as finite volume method (FVM), finite element method (FEM), finite difference method (FDM), etc. These analysis tools are widely used to solve the unsteady, three-dimensional, compressible Euler or Navier-Stokes equations. The Euler solutions are found to be valid for inviscous flow, while the Navier-Stokes solution can be used for the system that includes viscous effects. Therefore, the Euler solutions are less costly in CFD calculations compared to the Navier-Stokes solution. But there are still some problems in CFD based on different discretization methods. For example, FDM has difficulty in satisfying conservation laws and also is hard to apply for irregular geometries; FVM tends to be biased toward edges and one-dimensional physics; and it is difficult to solve hyperbolic equations by using FEM.

MD and MC simulations of fluid dynamics, on the other hand, are carried out in a bottom-up manner. In these models, the dynamics of the atoms or molecules are explicitly calculated, and the fluid properties, such as the flow velocity or density field, can be calculated as averages over the trajectories of the particles[3]. It is possible to extend the modeling accuracy to a wider range of scales and regimes, and exhibit nonlinear transport effects and small-scale fluctuations. But for pure MD, it is difficult to model the reaction-dependent processes, such as electrochemical reactions, in a reasonable timescale, because these processes are not driven by force field. For MC methods, they do not explicitly contain the time variable, and they are not truly dynamic methods. Also, these methods are computationally expensive, and it is problematic to be extended to large systems.

Even though these numerical methods are powerful in handling some targeted (usually simplified) systems, they may fail in the simulation of complex systems that require tracking the properties of the system both microscopically and macroscopically. Therefore, we need a mesoscopic numerical method that can bridge these two scales. In this thesis, we are trying to develop a mesoscopic method, Lattice Boltzmann Method (LBM), to simulate complex mass transfer problems. LBM was introduced two decades ago[5, 6], and now it has been developed into a powerful tool for CFD. From numerical calculation side, the kinetic nature of LBM has three important features. First, the convection operator (streaming process) of LBM in phase space (velocity space) is linear, contrasting with the

nonlinear convection terms in other approaches. Second, the pressure in LBM can be obtained by an equation of state in the nearly incompressible limit, compared to the direct numerical simulation, where the pressure has to be calculated by solving a Poisson equation with velocity strains acting as sources, which usually requires special treatment, such as iteration or relaxation. Third, comparing with the traditional kinetic theory with the Maxwell-Boltzmann equilibrium distribution, the LBM uses a smaller set of velocities in phase space. Therefore, the transformation between the microscopic distribution function and macroscopic quantities is greatly simplified. This method is particularly successful in fluid flow applications involving interfacial dynamics and complex boundaries[7]. Even though it is based on a particle picture, rather than concentrating on the microscopic behavior of particles, LBM focuses on the averaged microscopic behavior. Thus, the computational cost is lower than the atomistic methods.

The popularity of LBM is based in part on its simple formulation and application to flow problems compared with solving the Navier-Stokes equations, and in part on the high level of scalability on parallel processing systems[8]. Therefore, it is possible to use this method to simulate a comparatively large system. In this thesis, we are particularly interested in the electrochemical energy storage systems and transdermal drug delivery system. In the following chapters, this thesis will be constructed in the following way:

Chapter 2 gives a brief introduction of the LBM. We briefly show that how Lattice Boltzmann Equation (LBE) is derived from traditional Boltzmann Equation, Chapman-Enskog Expansion and asymptotic analysis of LBE, lattice arrangement and boundary conditions of LBM.

Chapter 3 shows the LBM model for EDLCs. The simulation of diffuse charge dynamics is carried out for both the charge and the discharge processes on complex random electrode geometries of 2D symmetric systems. We accounted for the steric effect and compared the influence of microstructures of electrodes in the systems.

Chapter 4 focuses on the LBM model for the dendrite formation process on the anode of LIBs. A half-cell 2D simulation is carried out to simulate the dendrite formation on the Li metal electrode during charge and discharge cycles. The mechanism of dendrite formation process is discussed in detail and compared with the traditional Sand's time theories. A new analysis method is introduced, which can predict the formation of dendrites in batteries at a very early stage even before large dendrites form.

Chapter 5 introduces the LBM model for simulating the intercalation reactions in graphite electrode of LIBs. A 3D half-cell is used for the simulation of intercalation reactions of randomly distributed graphite electrode with different electrode densities. Both galvanostatic and potentiostatic conditions were studied. The relation between operation parameters (current and potential) and electrode parameters (porosity, thickness and diffusivity) and plating times were discussed.

Chapter 6 shows the LBM model for transdermal drug delivery system. We compared two commonly used structures for the simulation - "brick and mortar" and homogenized structures. The influence of different system parameters (amount of drug in patch, patch thickness, partition coefficient at patch/ Stratum Corneum (SC) interface, and the diffusion coefficient of drug in each component) is discussed in details. The influence of enhancer is also tested.

Finally, we will end with the discussion of future work.

Chapter 2. Introduction to Lattice Boltzmann Method

The LBM was originally used as a class of Computational Fluid Dynamics methods to simulate the dynamics of fluids. LBM has its origins in the lattice gas automata (LGA) method. LGA can be considered as a simplified fictitious molecular dynamics model in which the fluid particles move and collide on the regular lattices and the macroscopic variables, such as the density and velocity, satisfy the equation similar to the Navier-Stokes equations[9]. While Lattice Gas methods have been used to study different flow conditions[10-12], there are a number of problems associated with this method, such as lacking of Galilean invariance and noisy simulations which require a great deal of averaging[13].

LBM improves on the ideas in LGA. Rather than following the evolution of "particles", LBM traces the evolution of "ensemble-averaged distribution function" which represents the probability of finding a particle at a particular site. Using this approach, the macroscopic Navier-Stokes equations can be obtained from the Lattice Boltzmann Equation (LBE). Even though LBM is a widely used CFD method, it also has lots of applications in complex dissolution processes[14-17], electroosmotic/electrokinetic flows[18-20], crystallization[21, 22], electrochemical systems[23, 24], and even the simulation of the Schrödinger equation[25, 26]. In this chapter, we start by introducing the Boltzmann equation and then discuss how the Lattice Boltzmann Equations can be obtained from it. Finally, we will show how to construct lattice and deal with the boundary conditions for the Lattice Boltzmann Method, so that it can be applied to the problems dealing with mass transport and local reactions.

2.1 The Boltzmann Equation

In 1872, the famous Austrian physicist Ludwig Eduard Boltzmann devised the Boltzmann Equation (BE) or Boltzmann Transport Equation (BTE) to describe the statistical behavior of a thermodynamic system not in thermodynamic equilibrium. In the BE, instead of tracing all the individual positions and momenta of each particle in a system, it considers the probability that a number of particles in a volume of $d^3\boldsymbol{r}d^3\boldsymbol{p}$ phase space. This probability distribution function is denoted as $f(\boldsymbol{r}, \boldsymbol{p}, t)$, where $\boldsymbol{r}$ and $\boldsymbol{p}$ are the position and momenta at the time t. The number of particles N which all have $\boldsymbol{r}$ and $\boldsymbol{p}$ at time t has the following relationship with the probability distribution function:

$$dN = f(\boldsymbol{r}, \boldsymbol{p}, t)d^3\boldsymbol{r}d^3\boldsymbol{p} \qquad (2.1.1)$$

Now, consider an external force $\boldsymbol{F}$ acting on the particles. At time $t + \Delta t$, particle position will be $\boldsymbol{r} + \Delta\boldsymbol{r} = \boldsymbol{r} + \boldsymbol{p}\Delta t/m$, and momentum will be $\boldsymbol{p} + \Delta\boldsymbol{p} = \boldsymbol{p} + \boldsymbol{F}\Delta t$. If there are no internal collisions, the phase space volume element should be constant, which gives:

$$f\left(\boldsymbol{r} + \frac{\boldsymbol{P}}{m}\Delta t, \boldsymbol{p} + \boldsymbol{F}\Delta t, t + \Delta t\right)d^3\boldsymbol{r}d^3\boldsymbol{p} = f(\boldsymbol{r}, \boldsymbol{p}, t)d^3\boldsymbol{r}d^3\boldsymbol{p} \qquad (2.1.2)$$

However, if internal collisions take place, there will be a net difference of particle numbers in the phase space volume element $d^3\boldsymbol{r}d^3\boldsymbol{p}$. The change rate of distribution function due to collisions is called collision operator, Ω. Now we can write out the evolution equation for the probability distribution function:

$$f\left(\boldsymbol{r} + \frac{\boldsymbol{P}}{m}\Delta t, \boldsymbol{p} + \boldsymbol{F}\Delta t, t + \Delta t\right)d^3\boldsymbol{r}d^3\boldsymbol{p} - f(\boldsymbol{r}, \boldsymbol{p}, t)d^3\boldsymbol{r}d^3\boldsymbol{p} = \boldsymbol{\Omega}(f)\Delta t d^3\boldsymbol{r}d^3\boldsymbol{p} \qquad (2.1.3)$$

Dividing the above equation by $d^3\boldsymbol{r}d^3\boldsymbol{p}$ and let $\Delta t \rightarrow 0$, then:

$$\frac{df}{dt} = \Omega(f) \qquad (2.1.4)$$

Since the probability distribution function *f* is a function of $\boldsymbol{r}$, $\boldsymbol{p}$, and *t*, therefore,

$$\frac{df}{dt} = \frac{\partial f}{\partial \boldsymbol{r}}\frac{d\boldsymbol{r}}{dt} + \frac{\partial f}{\partial \boldsymbol{P}}\frac{d\boldsymbol{P}}{dt} + \frac{\partial f}{\partial t} \qquad (2.1.5)$$

Replace $d\boldsymbol{r}/dt$ with $\boldsymbol{p}/m$, $d\boldsymbol{p}/dt$ with $\boldsymbol{F}$, and take ∇ as the gradient operator. Then we will obtain the Boltzmann Equation as:

$$\frac{\boldsymbol{p}}{m}\nabla f + \boldsymbol{F}\frac{\partial f}{\partial \boldsymbol{P}} + \frac{\partial f}{\partial t} = \Omega(f) \qquad (2.1.6)$$

Note that this equation is still not complete because the collision term $\Omega(f)$ is unknown. This term should be a statistical representation of particle collisions, which has a relationship with the statistic distributions of particles, such as Maxwell–Boltzmann, Fermi–Dirac or Bose–Einstein distributions.

2.2 H-theorem and The Bhatnagar–Gross–Krook (BGK) Approximation

As is shown in the equ.2.1.6, the key factor to solve Boltzmann equation is to determine the collision term that specifies how the distribution function changes after a two-particle collision. However, the forms of this term in most physical systems are too complicated to be used. So simplifications are needed to approximate the collision process.

Boltzmann made an assumption that the collision term is determined from two-body interaction that is uncorrelated before the collision. This is also known as the *Stosszahlansatz* or molecular chaos assumption. Under this assumption, the continual process of collisions is associated with irreversibility, which reflects the second law of thermodynamics. Boltzmann discovered a quantitative measure of the irreversibility, which is referred as the H-function[27]:

$$H(t) = -\int f \ln f \, d^3\boldsymbol{p} d^3\boldsymbol{r} \qquad (2.2.1)$$

This is a monotonically increasing function of time, regardless of the underlying microscopic potential (H-theorem). Therefore, when designing the approximation of the collision term, at least two main properties should be kept[28]: first, the same quantities that are conserved under collisions must also be conserved in the approximation; second, Boltzmann's H-theorem must be fulfilled for the approximated collision operator.

Bhatnagar, Gross and Krook introduced a simple but widely used collision operator that is known as BGK collision operator. The BGK approximation states that the main effect of the collision term is to bring the local distribution function to the local equilibrium distribution. If f and f^{eq} denote the distribution function and local equilibrium distribution function respectively, and let τ be the relaxation time which reflects the rate of this process, then the collision operator $\Omega(f)$ can be explicitly expressed as:

$$\Omega(f) = -\frac{1}{\tau}(f - f^{eq}) \qquad (2.2.2)$$

Therefore, the Boltzmann equation can be simplified as:

$$\frac{\boldsymbol{p}}{m}\nabla f + \boldsymbol{F}\frac{\partial f}{\partial \boldsymbol{P}} + \frac{\partial f}{\partial t} = -\frac{1}{\tau}(f - f^{eq}) \quad (2.2.3)$$

2.3 Discretization and The Lattice Boltzmann Equation

The equ.2.2.1 is a continuum differential equation. If we assume this equation is valid along specific directions and linkages *i* in space, the discrete Boltzmann equation can be written as,

$$\frac{\partial f_i}{\partial t} + \frac{\boldsymbol{p}_i}{m}\nabla f_i + \boldsymbol{F}_i\frac{\partial f_i}{\partial \boldsymbol{p}_i} = -\frac{1}{\tau}(f_i - f_i^{eq}) \quad (2.3.1)$$

or,

$$\frac{\partial f_i}{\partial t} + \frac{\boldsymbol{p}_i}{m}\nabla f_i = -\frac{1}{\tau}\left(f_i - f_i^{eq}\right) - \boldsymbol{F}_i\frac{\partial f_i}{\partial \boldsymbol{p}_i} \quad (2.3.2)$$

If we check the above equation carefully, we can find that the equation looks like an advection equation with source term. The left-hand side of the equation represents the advection and the right-hand side term represents the source. With a small time interval Δt, and let F_i^l be a generalization of the force in the equation, such as $F_i^l \leftrightarrow \boldsymbol{F}_i\frac{\partial f_i}{\partial \boldsymbol{p}_i}$, then we can obtain:

$$\frac{f(x + v_i\Delta t, v_i, t + \Delta t) - f(x, v_i, t)}{\Delta t} = -\frac{1}{\tau}\left(f_i - f_i^{eq}\right) - F_i^l \quad (2.3.3)$$

Where $v_i = \frac{\boldsymbol{p}_i}{m}$ is velocity in i^{th} direction. Here, if we discrete velocity space to a finite number of velocity vectors v_i, and discrete the space to lattices where $x + v_i\Delta t$ is again a lattice position, then the velocity vectors are fixed. Therefore, the Lattice Boltzmann Equation can be obtained as,

$$f(x + v_i\Delta t, t + \Delta t) - f(x, t) = -\frac{\Delta t}{\tau}\left(f_i - f_i^{eq}\right) - F_i^l\Delta t \quad (2.3.4)$$

If there is no external force, this equation can be simplified as,

$$f(x + v_i\Delta t, t + \Delta t) - f(x, t) = -\frac{\Delta t}{\tau}\left(f_i - f_i^{eq}\right) \quad (2.3.5)$$

This simple equation can be applied for many physics by specifying proper equilibrium distribution function, relaxation time and source term (external force) if needed.

2.4 Equilibrium Distribution Functions

In 1859, Maxwell constructed a distribution function of particles with the velocity of *c* in phase space. If the average kinetic energy and the temperature of the gas satisfy the following equation:

$$\overline{\frac{1}{2}mc^2} = \frac{3}{2}kT \quad (2.4.1)$$

Then the distribution function is written as[29]:

$$f(c) = 4\pi(\frac{m}{2\pi kT})^{\frac{3}{2}}c^2 e^{-\frac{mc^2}{2kT}} \quad (2.4.2)$$

Where *T* is temperature, *k* is Boltzmann constant, and *m* is the mass of particle. We should note that when constructing the distribution function, Maxwell did not assume the equilibrium is reached.

To devise the equilibrium distribution function, Boltzmann assumed that for any system large or small in thermal equilibrium at temperature *T*, the probability of particles being in a particular state of energy *E* is proportional to $e^{\frac{-E}{kT}}$. Then the equilibrium distribution function can be written as[29],

$$f(c) = (\frac{m}{2\pi kT})^{\frac{3}{2}}e^{-\frac{mc^2}{2kT}} \quad (2.4.3)$$

If we multiply the Boltzmann distribution function by $4\pi c^2$, which is the surface area of a sphere in phase space, the Maxwell distribution function can be recovered. Therefore, this equilibrium distribution function is also called the Maxwell – Boltzmann distribution. We can therefore use this distribution function for the equilibrium distribution function in lattice Boltzmann equation.

For particles with density ρ moving in a medium with macroscopic velocity $\boldsymbol{u}$ and particle velocity $\boldsymbol{c}$, the normalized Maxwell's distribution function can be written as[29],

$$f = \frac{\rho}{2\pi/3}e^{-\frac{3}{2}c^2}\, e^{\frac{3(\boldsymbol{c}\cdot\boldsymbol{u}-u^2)}{2}} \quad (2.4.4)$$

Where c^2 and u^2 are $\boldsymbol{c}\cdot\boldsymbol{c}$ and $\boldsymbol{u}\cdot\boldsymbol{u}$ respectively. By using the Taylor expansion around the stationary state, we can obtain,

$$f = \frac{\rho}{2\pi/3}e^{-\frac{3}{2}c^2}\,[1 + 3(\boldsymbol{c}\cdot\boldsymbol{u}) - \frac{3}{2}\,u^2 + \cdots] \quad (2.4.5)$$

If we regard that this equation is also valid along specific directions and linkages *i* in space, and note that the Maxwell distribution also reflects the equilibrium distribution, by discarding the higher order terms, then we can obtain the discrete form of the equilibrium distribution,

$$f_i^{eq} = \Phi\omega_i\,[A + B(\boldsymbol{c_i}\cdot\boldsymbol{u}) + C(\boldsymbol{c_i}\cdot\boldsymbol{u})^2 + D\boldsymbol{u}^2] \quad (2.4.6)$$

A, *B*, *C* and *D* are constants and can be calculated out from conservation of mass, momentum and energy, etc. ω_i is the weight in the i^{th} linkage and it is related to the lattice arrangements, which we will introduce in the section 2.7. The summation of all ω_i of the lattice links at a certain lattice is unity,

$$\sum_{i=0}^{n}\omega_i = 1 \quad (2.4.7)$$

Φ is a scalar which represents the local density of the "particles" that we are investigating. Note that the "particles" here are generalized particles that can be mass, temperature or thermal energy, etc. depending on the physical system we are interested in. Φ can be obtained by the summation of all the distribution functions of the lattice links at a certain lattice,

$$\Phi = \sum_{i=0}^{n} f_i^{eq} \quad (2.4.8)$$

For different physical systems, different equilibrium distribution functions can be constructed. For example, for a pure diffusion process, the macroscopic velocity of flow is zero, therefore the distribution function is,

$$f_i^{eq} = \Phi A \omega_i \qquad (2.4.9)$$

Putting equ.2.4.9 back to equ.2.4.8, it is easy to get the value of A, which is 1.

2.5 The Chapman-Enskog Expansion

The distribution of the particles can also be regarded as a mean field picture emerging from a perturbative treatment of the kinetic equations[27]. Let the perturbation parameter be the *Knudsen number* ϵ, which is the ratio of mean free path and the characteristic length of the system, by Chapman-Enskog Expansion, the distribution function f_i and f_i^{eq} can be expressed as,

$$f_i = f_i^{(0)} + \epsilon f_i^{(1)} + \epsilon^2 f_i^{(2)} + \mathcal{O}(\epsilon^3) \qquad (2.5.1)$$

$$f_i^{eq} = f_i^{(eq,0)} + \epsilon f_i^{(eq,1)} + \epsilon^2 f_i^{(eq,2)} + \mathcal{O}(\epsilon^3) \qquad (2.5.2)$$

The Taylor expansion of the LBE equ.2.3.5 can be written as,

$$\epsilon(\boldsymbol{c}_i \cdot \nabla f_i) + \epsilon^2 \left(\partial_t f_i + \frac{(\boldsymbol{c}_i \cdot \nabla f_i)^2}{2} \right) + \mathcal{O}(\epsilon^3) = -\omega[f_i - f_i^{eq}] \qquad (2.5.3)$$

Where $\omega = \frac{\Delta t}{\tau}$ is the relaxation parameter and $\boldsymbol{c}_i = \frac{\delta_{x,i}}{\delta_t}$ is the lattice speed.
By inserting equ.2.5.1 and equ.2.5.2 to equ.2.5.3, for each leading orders in ϵ we have,

$$0 = -\omega \left[f_i^{(0)} - f_i^{(eq,0)} \right] \qquad (2.5.4)$$

$$\boldsymbol{c}_i \cdot \nabla f_i^{(0)} = -\omega \left[f_i^{(1)} - f_i^{(eq,1)} \right] \qquad (2.5.5)$$

$$\boldsymbol{c}_i \cdot \nabla f_i^{(1)} + \partial_t f_i^{(0)} + \frac{\left(\boldsymbol{c}_i \cdot \nabla f_i^{(0)} \right)^2}{2} = -\omega \left[f_i^{(2)} - f_i^{(eq,2)} \right] \qquad (2.5.6)$$

Note that the order of ϵ can be extended to higher orders if needed, and the method will be the same. Now for an equation of a particular order in ϵ, it is possible to use collision invariants and replace $f_i^{(n)}$ of higher order in ϵ by the equations of lower order in ϵ. In the end, macroscopic variables of differential equations can be obtained by moments of the distribution functions.

2.6 Asymptotic Analysis for Advection-Diffusion Equation

Now we take the advection-diffusion equation as an example to illuminate the idea of Chapman-Enskog Expansion introduced in the former section. The advection-diffusion equation can be written as,

$$\frac{\partial \rho}{\partial t} + \nabla(\boldsymbol{u}\rho - D\nabla\rho) = 0 \qquad (2.6.1)$$

The LBE is written as,

$$f(x + c_i\delta_t, t + \delta_t) - f(x,t) = -\omega\left(f_i(x,t) - f_i^{eq}(x,t)\right) \qquad (2.6.2)$$

with the equilibrium distribution function,

$$f_i^{eq} = w_i\rho[1 + \frac{\boldsymbol{c}_i \cdot \boldsymbol{u}}{c_s^2}] \qquad (2.6.3)$$

where c_s is the speed of sound in the lattice which reflects an effective propagation velocity of the lattice. Now expand density, flux and advective velocity according to Chapman-Enskog Expansion,

$$\rho = \rho^{(0)} + \epsilon\rho^{(1)} + \epsilon^2\rho^{(2)} + \mathcal{O}(\epsilon^3) \qquad (2.6.4)$$

$$\boldsymbol{j} = \boldsymbol{j}^{(0)} + \epsilon\boldsymbol{j}^{(1)} + \epsilon^2\boldsymbol{j}^{(2)} + \mathcal{O}(\epsilon^3) \qquad (2.6.5)$$

$$\boldsymbol{u} = \boldsymbol{u}^{(0)} + \epsilon\boldsymbol{u}^{(1)} + \epsilon^2\boldsymbol{u}^{(2)} + \mathcal{O}(\epsilon^3) \qquad (2.6.6)$$

Insert these equations into the equilibrium distribution function, and then the expansion of the equilibrium distribution function can be obtained. It has been proved[29] that if the advective velocity $\boldsymbol{u}$ is initialized properly, $\boldsymbol{u}^{(0)} = 0$. Therefore,

$$f_i^{(0)} = w_i\rho^{(0)} \qquad (2.6.7)$$

For the distribution function of order one in ϵ,

$$f_i^{(1)} = -\frac{1}{\omega}\left(\boldsymbol{c}_i \cdot \nabla\left(w_i\rho^{(0)}\right)\right) + w_i(\rho^{(1)} + \rho^{(0)}\frac{\boldsymbol{c}_i \cdot \boldsymbol{u}^{(1)}}{c_s^2}) \qquad (2.6.8)$$

Taking the first moment of $f_i^{(1)}$ gives,

$$\boldsymbol{j}^{(1)} = \rho^{(0)}\boldsymbol{u}^{(1)} - \frac{c_s^2}{\omega}\nabla\rho^{(0)} \qquad (2.6.9)$$

Note that $\boldsymbol{j}^{(0)} = 0$, since $\boldsymbol{u}^{(0)} = 0$.
Going on to the order two in ϵ, we get:

$$\nabla\boldsymbol{j}^{(1)} + \partial_t\rho^{(0)} + \frac{c_s^2}{2}\nabla^2\rho^{(0)} = 0 \qquad (2.6.10)$$

and inserting equ.2.6.9 will lead to,

$$\partial_t\rho^{(0)} + \nabla\left[\rho^{(0)}\boldsymbol{u}^{(1)} - c_s^2\left(\frac{1}{\omega} - \frac{1}{2}\right)\nabla\rho^{(0)}\right] = 0 \qquad (2.6.11)$$

which is an advection diffusion equation with a diffusion constant satisfying,

$$D = c_s^2\left(\frac{1}{\omega} - \frac{1}{2}\right) \qquad (2.6.12)$$

2.7 Lattice Arrangements

When applying LBE to simulate physical systems, we have to specify the arrangement of lattices for the numerical calculation. The common terminology used in LBM is to refer to the dimension of the problem and the number of speed by using DnQm, where n represent the dimension of the problem (1 for 1-D, 2 for 2-D and 3 for 3-D) and m refers to the speed model, number of linkages[29]. The lattices cannot be setup arbitrarily because a certain degree of isotropy should be satisfied in order to retrieve the desired equation. We will not dig into this topic here. Some references[27, 30] are available if you are interested. In this thesis we will just introduce some widely used lattice arrangements that can be applied to our systems.

2.7.1 Two-Dimensional System

In general two models are used in simulation of two-dimensional system, D2Q5 and D2Q9. Fig.2.1[31] shows the arrangement of these two lattices.

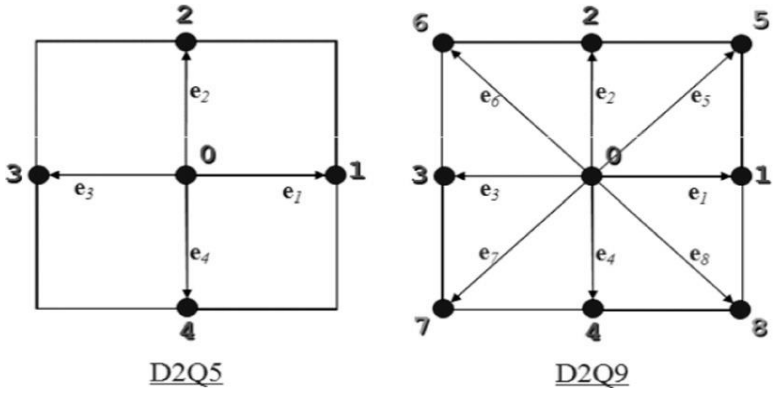

Fig. 2. 1 Arrangement of D2Q5 (left) and D2Q9 (right) lattices

As is shown in the Fig.2.1, D2Q5 lattice has 4 velocity vectors, $\boldsymbol{e_1}$, $\boldsymbol{e_2}$, $\boldsymbol{e_3}$, and $\boldsymbol{e_4}$, and one more velocity for the distribution function resides at the central node, which is zero. There are 5 distribution functions in a lattice, f_0, f_1, f_2, f_3, and f_4. Each of the distribution functions represents the amount of particles moving along with the corresponding lattice velocity vectors. This distribution functions can be regarded as a histogram representing the frequency of occurrence, which denotes the direction-specific fluid densities. The weighting factors w_i, which we have mentioned in the previous chapters, are 1/3 for f_0 and 1/6 for f_1, f_2, f_3, and f_4. It is worthy to mention that this arrangement cannot be used to simulate fluid flows[29]. However, the advection-diffusion problems can be simulated with this simple lattice.

The D2Q9 lattice is very commonly used for solving fluid flow problem. The velocities in the lattice can be grouped into 3 categories: $\boldsymbol{e}_0$ has a velocity of 0; $\boldsymbol{e}_1$ through $\boldsymbol{e}_4$ have a velocity of 1 lattice unit per time step (1 *lu ts*$^{-1}$); $\boldsymbol{e}_5$ through $\boldsymbol{e}_8$ have a velocity of $\sqrt{2}$ *lu ts*$^{-1}$, as is shown in the Fig.2.1. The weights of distribution are 0 for direction 4/9 (original position), 1/9 for directions of 1, 2, 3, 4, and 1/36 for directions of 5, 6, 7, and 8.

2.7.2 Three-Dimensional system

The most widely used 3D lattice for advection-diffusion systems is D3Q7, while for Navier-Stokes systems is D3Q19[27].

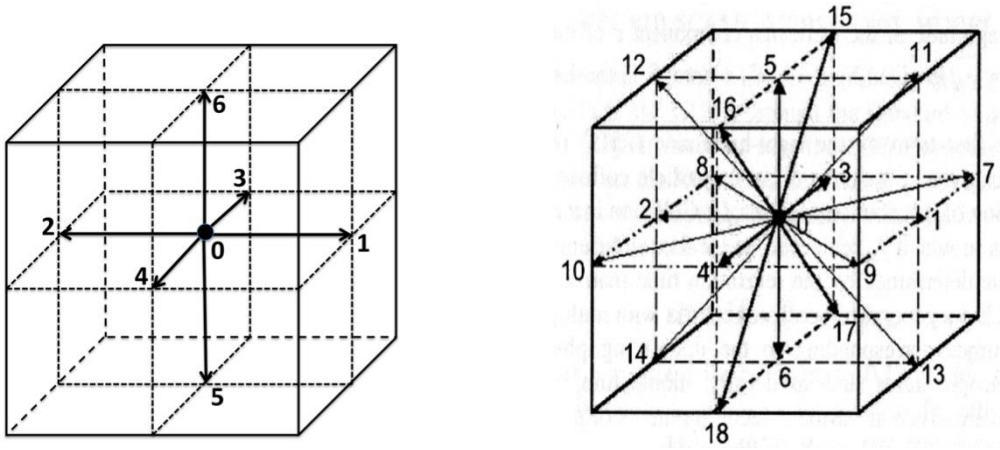

Fig. 2. 2 Arrangement of D3Q7 (left) and D3Q19 (right) lattices

The way we discrete 3D system is much similar to the 2D system. For D3Q7 lattice, there are 7 velocity vectors. The weights are 1/4 for direction of 0 and 1/8 for the rest directions. For D3Q19 lattice, there are 19 velocity vectors. The weights are 1/3 for direction of 0, 1/18 for directions from 1 to 6, and 1/36 for the rest directions.

2.8 Boundary Conditions

While the equ.2.3.4 and equ.2.3.5 define the evolution of distribution functions, on the boundaries, the process can be different according to different boundary conditions. There are various boundary conditions proposed by many investigators for different applications[32-37]. Here, we will only focus on four basic kinds of boundaries that are commonly used: Periodic, Bounce-back, Neumann, and Dirichlet Boundaries.

2.8.1 Periodic Boundary Condition

The periodic boundary condition is used when the surface effects play a negligible role, or when only the properties of the bulk are concerned. It is very easy to implement periodic boundary condition in the LBM system. Only a buffer boundary is needed to get the information on the opposite side and the streaming step will update the information directly on the boundary nodes. Here, we need to the update the buffer boundary in every time step before the streaming happens. The basic idea of periodic boundary condition is shown in Fig.2.3. The solid nodes denote the simulation domain and the hollow nodes denote the buffer boundary. When particles leave from the right, they will fill in the left buffers and vice versa.

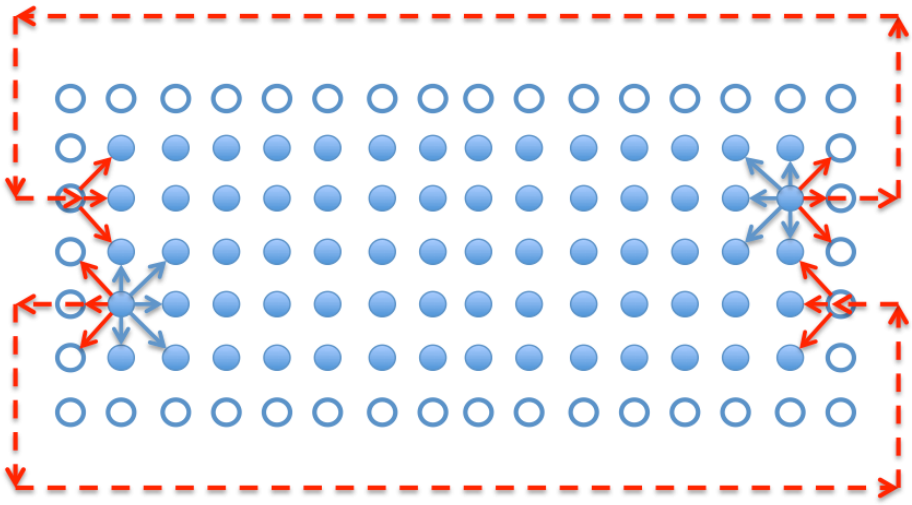

Fig. 2. 3 Illustration of Periodic boundary condition

2.8.2 Bounce-back Boundary Condition

Bounce-back boundary is also called no-slip Bounce-back boundary. It is commonly used when the solid wall is sufficient rigid so that there is no net fluid motion at the wall. Two distinct types of implementations can be used for Bounce-back nodes: On-grid and Mid-grid.

In the On-grid Bounce-back boundary condition, the physical boundary lies exactly on a grid line. Therefore, what we need to do is just to reverse all populations sitting on a boundary node in a certain collide and the stream step.

In the Mid-grid Bounce-back boundary condition, the physical boundary lies in between two grid lines, so that solid nodes are at one side of the boundary line and fluid nodes are at the other side. The bounce-back process can be divided into 4 steps shown in Fig.2.4.

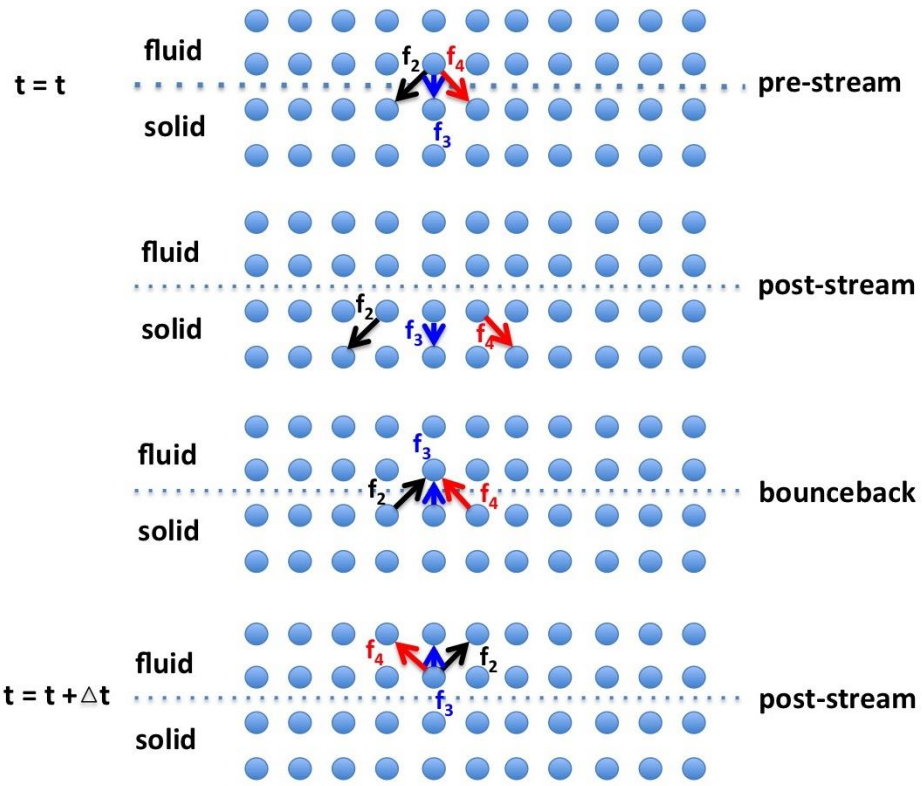

Fig. 2. 4 Illustration of Mid-grid Bounce-back boundary condition

It is proved that the On-grid Bounce-back is generally first-order accurate while the Mid-grid Bounce-back has second-order accuracy[27].

2.8.3 Neumann Boundary Condition

Neumann boundary conditions usually define the flux value at the boundaries. For a known flux value, a velocity vector $\boldsymbol{u}$ is specified at the boundary. After the streaming step, the unknown direction densities at each boundary node, pointing from the boundary into the domain, should be solved based on the velocity information. Taking a D2Q9 lattice as an example (shown in Fig.2.5), densities f_4, f_7, and f_8 are unknown after steaming.

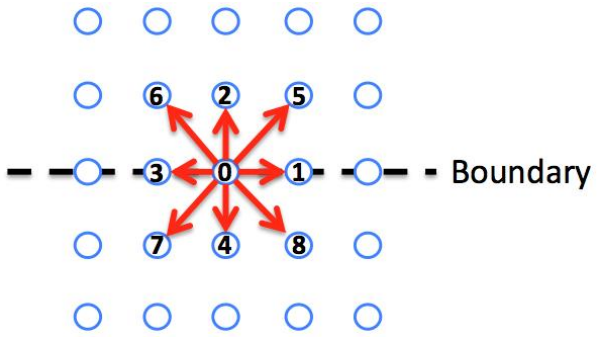

Fig. 2. 5 Illustration of boundary nodes for D2Q9 lattice

The macroscopic density is defined as:

$$\rho = \sum_{i=0}^{q-1} f_i \qquad (2.8.1)$$

If the velocity at the boundary is defined as $\boldsymbol{u} = \begin{bmatrix} u_x \\ u_y \end{bmatrix}$, it is possible to decompose the contribution of individual distribution function f_i to the velocity in x and y directions:

$$\rho u_x = f_1 - f_3 + f_5 - f_6 + f_8 - f_7 \qquad (2.8.2)$$

$$\rho u_y = f_2 - f_4 + f_5 - f_8 + f_6 - f_7 \qquad (2.8.3)$$

Right now, we have four unknowns but only three equations. To solve for these unknowns, we need a proper assumption to construct the fourth equation. Zou and He[38] proposed an assumption that the Bounce-Back condition can be applied in the direction normal to the boundary, therefore:

$$f_2 - f_2^{eq} = f_4 - f_4^{eq} \qquad (2.8.4)$$

The equilibrium distribution functions can be calculated based on equ.2.4.6 mentioned in section 2.4. Until now, there are linear equations for four unknowns, and it is easy to solve these linear equations to obtain the unknown distributions.

We should note that the Zou and He's assumption is just one of the commonly used method for this boundary condition. There are several assumptions worked for the Neumann boundary conditions. The reader can refer to other papers for further readings[39-41].

2.8.4 Dirichlet Boundary Condition

Similar to Neumann boundary conditions, in Dirichlet boundary conditions the unknown direction densities at each boundary node should be solved based on the pressure/density information that is predefined at the boundaries. Also here we use a D2Q9 lattice in Fig.2.5 as an example, and densities f_4, f_7, and f_8 are unknown after steaming.

The Dirichlet boundary condition imply that the density at the boundary is known, $\rho = \rho_0$:

$$\rho_0 = \sum_{i=0}^{q-1} f_i \qquad (2.8.5)$$

The velocity at the boundary is defined as $\boldsymbol{u} = \begin{bmatrix} 0 \\ u_y \end{bmatrix}$. Here we assume the velocity that is tangent to the boundary is zero and the velocity that is normal to the boundary is unknown. Then we have,

$$0 = f_1 - f_3 + f_5 - f_6 + f_8 - f_7 \qquad (2.8.6)$$

$$\rho_0 u_y = f_2 - f_4 + f_5 - f_8 + f_6 - f_7 \qquad (2.8.7)$$

And also assume the Bounce-back condition can be applied in the direction normal to the boundary:

$$f_2 - f_2^{eq} = f_4 - f_4^{eq} \qquad (2.8.8)$$

Now we have four equations for four unknowns, which can be solved easily.

Similar to Neumann boundary conditions, there are other assumptions worked for the Dirichlet boundary conditions. The reader can refer to other papers for further reading. [42-48].

Chapter 3. Simulation of Diffuse-charge Capacitance in Electric Double Layer Capacitors by Using Lattice Boltzmann Method

3.1 Introduction

The rapidly growing demand for energy storage has brought considerable attention to the study of batteries and Electric Double Layer Capacitors (EDLCs)[49]. Generally speaking, batteries store energy in the form of electrochemical reactions known as the faradaic processes, while EDLCs store energy by physical separation of ions. Comparing to batteries, EDLCs have much better cyclic reversibility, faster charge/discharge rate and wider working temperature range, which makes them a very attractive option as energy storage devices in lots of applications, such as electrical and hybrid vehicles[50], smart grid management[51, 52], renewable energy generation[53], and piezo-electric[54]. However, one of the biggest shortcomings of EDLCs is its low energy density. In order to increase energy density, lots of attempts have been made[55-62], and the key point that has been identified is to synthetize porous electrode materials with high surface area while at the same time improving the accessibility of the pores to the electrolyte[63]. The development of numerical tools to study EDLCs can be of great help for us to understand the physical phenomena and identify the design parameters for the electrode in order to obtain optimal performance[64]. In this chapter, we will introduce a LBM model to simulate the diffuse-charge dynamics in the EDLCs, which can handle complicated geometries of capacitors and include the steric effects of concentrated charged particles. The model can be helpful for the capacitor design from the mesoscopic point of view.

3.2 Background

While there are many attempts to model the EDLCs systems by using equivalent electrical circuits method[65-69], which are useful to monitor the performance of macroscopic EDLCs systems, the lack of detailed information of electrode structures and mass transfer mechanisms in these models makes them insufficient for us to understand the inherent physical processes and to design optimal materials for EDLCs. To tackle these problems, microscopic[70-75] and mesoscopic[64, 76-83] electric double layer (EDL) models have been developed. Microscopically, people have focused on studying the electrode-electrolyte interphase (Stern layer) that is influenced by adsorption, dielectric property of the media and particle-solvent interactions. This is usually simulated by using Molecular Dynamics (MD) and can give us information of the charge distribution in the Stern layer and thus the double layer capacitance. These studies are performed at a length scale too small to allow for design of electrode structures. To increase the length scale involved, mesoscopic numerical models based on solving Poisson-Boltzmann (PB) equation or Poisson-Nernst-Plank (PNP) equations are used to obtain charge distributions beyond the Stern layer. The Stern layer effect is either ignored or simplified by a Stern layer capacitance to take account of a potential drop in that thin layer. The diffuse charge dynamics in these systems are usually solved analytically or by asymptotic analysis[78-80, 83], or numerically for simple electrode morphologies or porous electrode with homogenization[64, 76, 82, 84, 85]. Current models, however, do not account for details in the electrode structure. Since the electrode materials in EDLCs are highly randomized porous structures (and may have locally ordered structures), the mass transfer inside of the porous structure plays a critical role in the system. Therefore, we need a mesoscopic numerical method to take the consideration about the structure of the electrode materials. More recently, Chirkov and Rostokin simulated the active layers in EDLCs with 3D random morphologies[86, 87], but they mainly focused on the effective properties of the porous electrode itself rather than the whole capacitor system and they also did not consider the local ordered structures (spheres and fibers). Because of the large difference in the length scale (stern layer to the whole cell), it is hard to use a single simulation method to get the detailed charge distributions in both the stern layer and the whole capacitor system at the same time. Our work will focus on the mesoscopic simulation by using Lattice Boltzmann Method (LBM).

LBM was introduced three decades ago and was originally used as a powerful method for Computational Fluid Dynamics (CFD)[6, 88]. Extensions to the LBM have also been developed to simulate mass transfer systems of advection-diffusion type[89, 90], electroosmosis flow[91-93], and electrochemical reactions[23, 24]. It has been proved to be particularly successful in fluid flow applications involving interfacial dynamics and complex boundaries[7]. The diffuse-charge dynamics in EDLCs is very similar to electroosmosis flow system. However, instead of solving Poisson-Boltzmann equation for the equilibrium state, here we try to solve Poisson-Nernst-Plank equations directly for the time-dependent diffuse charge dynamics in the absence of electro-osmotic flow. In this chapter, both charge and discharge processes on complex random electrode geometries of 2D systems (pure random, random spheres and random fibers) will be investigated; steric effects of concentrated solutions will be considered by using modified Poisson-Nernst-Plank (MPNP) equations; and two different collision operations for LBM will be compared, one is to treat the electromigration as the advective term of regular advection diffusion equation, and the other is to treat it as the source or force term.

3.3 Simulation Model

3.3.1 Charge Transfer Dynamics

The charge transfer in the electrolyte can be expressed by the Poisson-Nernst-Plank (PNP) equations if no steric effect is considered:

$$\frac{\partial c_i}{\partial t} = D_i \nabla\left(\nabla c_i + \frac{z_i e c_i}{kT}\nabla\psi\right) \qquad (3.3.1)$$

$$\nabla^2\psi = -\frac{\rho_f}{\in} \qquad (3.3.2)$$

where c_i is the concentration of species *i*; D_i is the diffusion coefficient of the species; z_i is the charge on species *i; e* is the charge of an electron; *k* is Boltzmann constant; *T* is temperature; and ψ is electrical potential; ρ_f is the net charge density; and $\in$ is dielectric constant.

The steric effect can be considered by adding a steric term into the equ.3.3.1:

$$\frac{\partial c_i}{\partial t} = D_i \nabla\left(\nabla c_i + \frac{z_i e c_i}{kT}\nabla\psi + \frac{c_i \nabla(\sum_j c_j)}{\frac{1}{a^3} - (\sum_j c_j)}\right) \qquad (3.3.3)$$

where *a* is the mean spacing of ions at the maximum concentration, $a = c_{max}^{-1/3}$; and $\sum_j c_j$ represents total local concentration of ions.

To solve these equations numerically, we firstly normalize them according to previous work by Kilic, etc[79]. The resulting equations are as followings for PNP system:

$$\frac{\partial c_+}{\partial t} = \varepsilon \frac{\partial}{\partial x}\left(\frac{\partial c_+}{\partial x} + c_+ \frac{\partial \phi}{\partial x}\right) \qquad (3.3.4)$$

$$\frac{\partial c_-}{\partial t} = \varepsilon \frac{\partial}{\partial x}\left(\frac{\partial c_-}{\partial x} - c_- \frac{\partial \phi}{\partial x}\right) \quad (3.3.5)$$

$$-\varepsilon^2 \nabla^2 \phi = c_+ - c_- \quad (3.3.6)$$

For MPNP system (the Poisson equation will be kept the same as equ.3.3.6), and the Nernst-Plank equations become:

$$\frac{\partial c_+}{\partial t} = \varepsilon \frac{\partial}{\partial x}\left(\frac{\partial c_+}{\partial x} + c_+ \frac{\partial(\phi - \ln(1 - \upsilon(c_+ + c_-)))}{\partial x}\right) \quad (3.3.7)$$

$$\frac{\partial c_-}{\partial t} = \varepsilon \frac{\partial}{\partial x}\left(\frac{\partial c_-}{\partial x} - c_- \frac{\partial(\phi + \ln(1 - \upsilon(c_+ + c_-)))}{\partial x}\right) \quad (3.3.8)$$

where $c_+ = c_+'/2c_0$, $c_- = c_-'/2c_0$, c_+' and c_-' are original concentration of cation and anion in equ.3.3.1 and 3.3.3, $c_0$is the initial ion concentration. $\varepsilon = \lambda_D/L$, is the ration of Debye length λ_D to the system size L. ϕ is normalized electrostatic potential calculated from the Poisson equation. $\upsilon = 2a^3 c_0$, quantifies the role of steric effects.

The Poisson equation was solved by using traditional Successive Over-Relaxation (SOR) method, which readers can find in other publications[94].

There are two kinds of total diffuse charge in this system: one is the total net charge at the electrode-electrolyte interface, q_s, and the other is the total net charge (positive or negative) in the whole electrolyte q_a. They are scaled by $2zec_0L$ and calculated as:

$$q_s = \int_{\Omega_{anode/cathode}} (c_+ - c_-)dx \quad (3.3.9)$$

$$q_a = \int \delta(c_+ - c_-)dx, \qquad \begin{cases} \delta = 0, & if\ c_+ - c_- \le 0 \\ \delta = 1, & otherwise \end{cases} \quad (3.3.10)$$

where $\Omega_{anode/cathode}$ denotes the electrode-electrolyte interface of anode or cathode. Since we used symmetric electrodes, the integration will be the same for anode and cathode. Similarly, the integration of all the positive net charge and negative net charge will be the same because of the conservation of charge in the whole system.

The simulation of charge and discharge processes will stop when the system reaches equilibrium. Numerically speaking, we regard that when the error of q_a at a certain time *t* (not time step) satisfies the following relationship:

$$\left|\frac{q_{a,t} - q_{a,t-1}}{q_{a,t}}\right| \le 10^{-6} \quad (3.3.11)$$

the system is regarded to reach equilibrium.

3.3.2 Boundary Conditions

The boundary condition for electrical potential can take accounts of the possible presence of a thin insulating layer of fixed capacitance, and in the normalized form it reads:

$$\emptyset \pm \varepsilon\delta\frac{\partial\phi}{\partial x} = \pm v \qquad (3.3.12)$$

where δ represents the normalized effective thickness of the surface insulating layer; $v = zeV/kT$, is the normalized apply potential on anode and cathode. Since we do not know the exact value of δ in a system, in this paper, unless specified, we will ignore this layer and regard $\delta = 0$. However, it is possible to obtain the value for a specific system by microscopic simulations such as MD.

We used Bounce-back boundary condition for electrode boundaries. In the direction parallel to electrodes, we applied periodic boundary condition.

3.3.3 LBM Collision Operations

Generally speaking, there are two ways to solve the PNP equations in the framework of LBM. One is to treat the electromigration as the advective term of regular advection diffusion equation[18], and the other is to treat it as the source or force term[20]. These two methods should be able to give identical result for the system. Since we are interested in 2D system in this stage, D2Q5 lattice is used for the LBM.

A typical advection-diffusion equation has the following form:

$$\frac{\partial c}{\partial t} = \frac{\partial}{\partial x}(\varepsilon\frac{\partial c}{\partial x} - \vec{\boldsymbol{u}}c) \qquad (3.3.13)$$

If comparing the equ.3.3.13 with equ.3.3.4, 3.3.5, 3.3.7, and 3.3.8 term by term, it is easy to find that for PNP system:

$$\overrightarrow{u_+} = -\varepsilon\frac{\partial\phi}{\partial x} \qquad (3.3.14)$$

$$\overrightarrow{u_-} = \varepsilon\frac{\partial\phi}{\partial x} \qquad (3.3.15)$$

and for MPNP system:

$$\overrightarrow{u_+} = -\varepsilon\frac{\partial(\phi - \ln(1 - v(c_+ + c_-)))}{\partial x} \qquad (3.3.16)$$

$$\overrightarrow{u_-} = \varepsilon\frac{\partial(\phi + \ln(1 - v(c_+ + c_-)))}{\partial x} \qquad (3.3.17)$$

Therefore, we can solve the PNP/MPNP equations according to the well-developed advection-diffusion system in LBM directly. In a single-relaxation-time LB model, this physical system can be expressed as:

$$f_i(\boldsymbol{r} + \Delta t\boldsymbol{v}_i, t + \Delta t) = \left(1 - \frac{1}{\tau}\right) f_i + \frac{1}{\tau} f_i^{eq} \quad (3.3.18)$$

Where f_i (**r**, t) is the local density distribution function in the *i* direction; τ is the relaxation time. The velocity $\mathbf{v}_i$ is chosen so that, in one time step Δt, a particle can reach one of its nearest neighbors. f_i^{eq} is the equilibrium density distribution function. With a simple BGK dynamics, it can be calculated based on the expression:

$$f_i^{eq} = t_i\rho\,(1 + \frac{1}{c_s^2}\,\mathbf{v}_i \cdot \mathbf{u}) \quad (3.3.19)$$

Where c_s is the sound of speed in the lattice, and t_i is the weight factor in the *i* direction.

The PNP and MPNP systems could also be regarded as the diffusion of charged particles biased by electrical forces. Generally, people consider the influence of electrical force as a source term. Here we follow the method developed by Yang, etc.[20] but ignore the Navier-Stokes equations for the movement of electrolyte. The evolution equation of the model can be expressed as:

$$f_i(\boldsymbol{r} + \Delta t\boldsymbol{v}_i, t + \Delta t) = \left(1 - \frac{1}{\tau}\right) f_i + \frac{1}{\tau} f_i^{eq} - \delta_t S(\boldsymbol{r}, t) \quad (3.3.20)$$

where δ_t is the time step, and the local equilibrium distribution function is defined by equ.3.3.19, but in our case the velocity $\mathbf{u} = \mathbf{0}$, because the electrolyte is assume to be static in the whole simulation.

The source term distribution function can be expressed as:

$$S(\boldsymbol{r}, t) = t_i\mathbf{v}_i \cdot \boldsymbol{S} \quad (3.3.21)$$

Where $\boldsymbol{S} = \left(\frac{\tau - \frac{1}{2}}{\tau}\right)\rho\nabla\phi$ for PNP system, and the steric effects can be added into the electrical potential term for the MPNP system. The advantage of this method is that the advection and the force terms are separated so that it is possible to add the influence of electrolyte movement into the system.

If two numerical operations can lead to the same results for the same system, there must be some mathematical relationship between them. If we compare the equ.3.3.18 and equ.3.3.20 more carefully, put equ.3.3.19 and equ.3.3.21 back to the original equations, and suppose the potential gradient in the certain direction *i* is $d\phi_i$ and the lattice velocity is v_i, taking the PNP system as an example, we can obtain the following equations.

For advection-diffusion form:

$$f_i(\boldsymbol{r} + \Delta t\boldsymbol{v}_i, t + \Delta t) = \left(1 - \frac{1}{\tau}\right) f_i + \frac{1}{\tau} t_i\rho - \frac{\varepsilon}{\tau c_s^2}\, t_i\rho\mathrm{v}_i d\phi_i \quad (3.3.22)$$

For the source term method ($\mathbf{u} = \mathbf{0}, \delta_t = 1$):

$$f_i(\boldsymbol{r} + \Delta t\boldsymbol{v}_i, t + \Delta t) = \left(1 - \frac{1}{\tau}\right) f_i + \frac{1}{\tau} t_i\rho - \left(\frac{\tau - \frac{1}{2}}{\tau}\right) t_i\rho\mathrm{v}_i d\phi_i \quad (3.3.23)$$

Note that ε and τ have the following relation:

$$\tau = \frac{\varepsilon}{c_s^2} + \frac{1}{2} \qquad (3.3.24)$$

Put equ.3.3.24 back to equ.3.3.22 and 3.3.23, not surprisingly, we get identical equations. Therefore, mathematically speaking, these two collision operations are the same. So in this paper, we will use the advection-diffusion form for the simulations.

3.4 Results and Discussion

3.4.1 Validation of Model for Flat Electrodes

Firstly, we tested our LBM model by using flat electrodes. Fig.3.1 shows the net charge and potential distribution in the PNP system for two different applied potentials ($v = 0.1$ and $v = 2.0$). In both cases, charges will accumulate at the surface of electrode gradually, until the system reaches equilibrium. As expected, a higher applied potential will lead to higher charge density at the interface. The space charge distribution will then influence the potential distribution in the system. As is shown in Fig.3.1, a high potential gradient is observed near the electrode-electrolyte interface. The electrical migration resulting from potential field and the diffusion resulting from concentration gradient will have opposing influences on the movement of charged particles, and the equilibrium of the system is reached when these two factors balance each other. The same results can be obtained by using finite difference method (FDM) in the previous work by Bazant, etc[78].

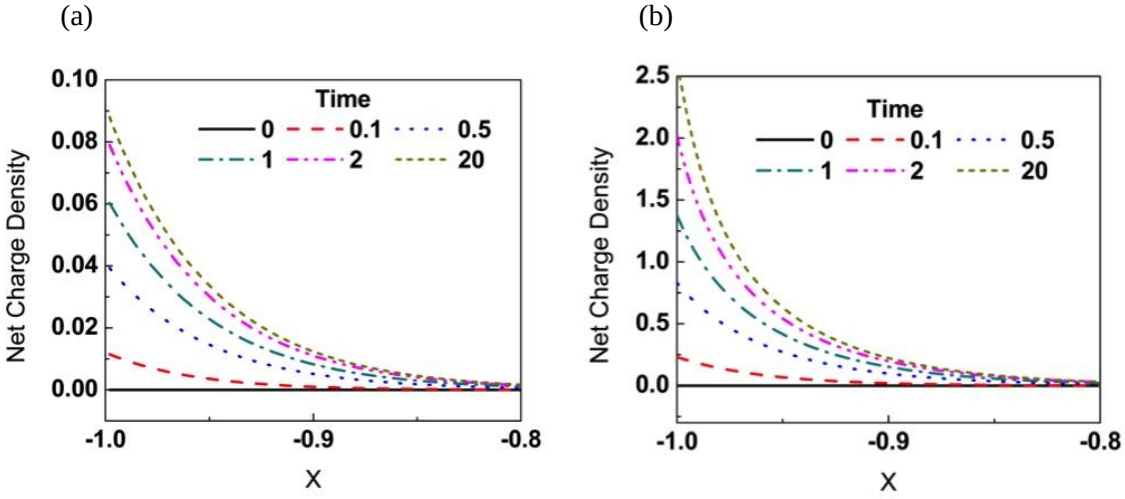

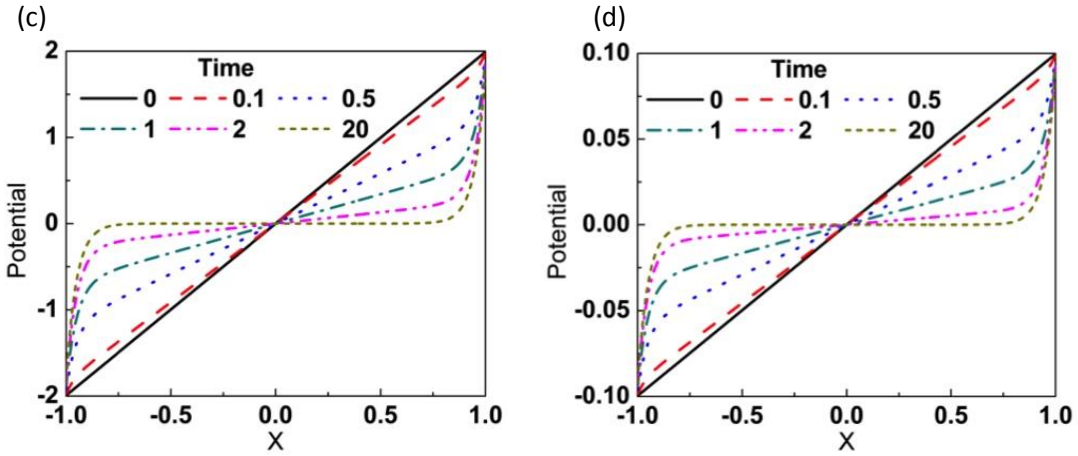

Fig. 3. 1 Profiles of the dimensionless charge density and potential ϕ (for $\varepsilon = 0.05$, $\delta = 0.1$). (a) net charge density with dimensionless voltage $v = 0.1$, (b) net charge density with dimensionless voltage $v = 2.0$, (c) dimensionless potential distribution with dimensionless voltage $v = 0.1$, and (d) dimensionless potential distribution with dimensionless voltage $v = 2.0$.

For MPNP system, we validated our model according to the parameters that used by Kilic, etc[79]. Fig.3.2 shows the total bulk concentration and net charge in both the PNP and MPNP systems for comparatively large applied potential $v = 10$. The steric effects parameter $\upsilon = 0.25$ reflects that the maximum dimensionless bulk concentration in the system is $1/\upsilon = 4.0$. As is shown in Fig.3.2, the interface concentration of the MPNP system will accumulate to the maximum bulk concentration, and then the system will reach equilibrium, while the interface concentration for PNP system will accumulate to a unreasonably large value due to the high applied potential. The consequence is that salt depletion in bulk is weaker in the MPNP system than the PNP system. Also, the same results can be obtained by using finite difference method (FDM) in the previous work by Kilic, etc[79].

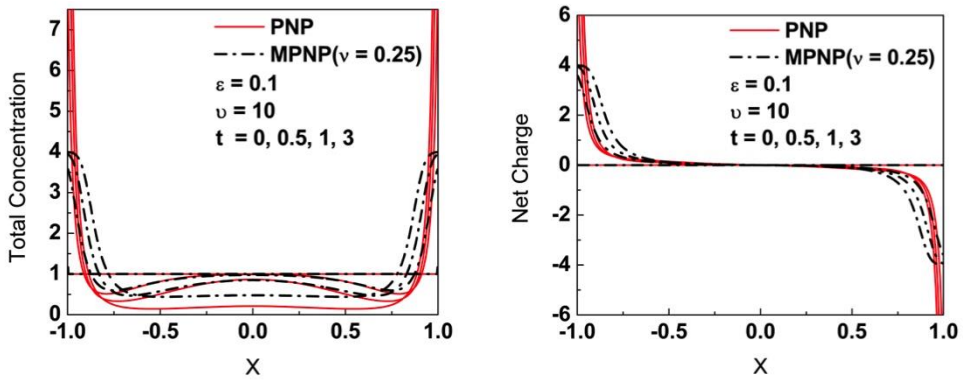

Fig. 3. 2 The numerical solution to the PNP (red) and MPNP (black) systems. The left figure shows the dimensionless bulk concentration field; the right figure shows the dimensionless charge density.

3.4.2 Charging and Discharging Processes for Electrodes with Random Morphologies

Since our LB model has been validated against other literature models, for the next set of simulations we included the effect of the electrode morphology and studied the charging and discharging

process for these capacitors. For charging, we fixed the applied potential of the system as v = 2.0, and ignored the Stern layer effect ($\delta = 0$). The ration of Debye length λ_D to the system size L, ε is fixed as 0.1.

We use the same system parameters for the discharge process as the charge process, and let the discharge begin right after the same system being fully charged under the potential of v = 2.0. By applying different potentials (v = 1.5, 1.25, 1.0, 0.75, and 0.5) at the electrode, we tested the diffuse charge dynamics of discharging process on different electrode morphologies.

What we are mostly interested in the capacitor system are the total net charge, which represents the total energy stored, the total interface charge, which denotes the net charge accumulated at the solid liquid interface (without stern layer), and the charge time, which reflects the speed of charge. For simplicity, in this paper, we will call the total net charge in the whole capacitor system as total charge, and the total interface charge will be kept as it is.

Three kinds of random morphologies were tested: pure random, random spheres and random fibers. Different electrode densities (from 20% to 50%) and different sizes (radius r for spheres and length L for fibers) of random structures were compared. r and L are in the unit of lattice length. The morphology of anode and cathode are symmetric. **Fig.3.3** shows the morphologies of anode at the density of 30%. Also, in order to reduce the errors resulted from a certain random morphology, every data point in this paper has been averaged over 5 different random morphologies.

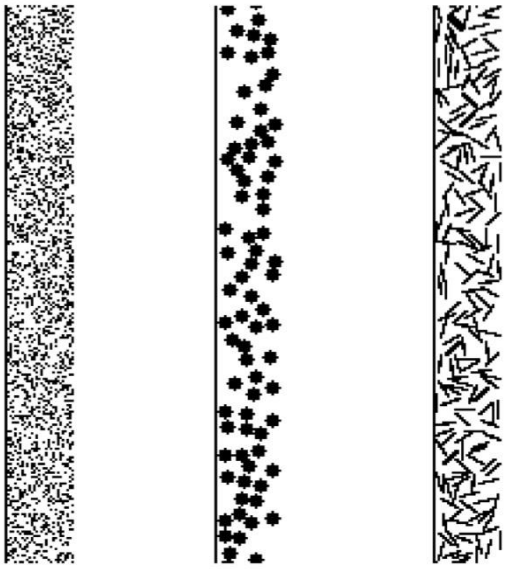

Fig. 3. 3 Electrode morphologies of density of 30%: random (left), random spheres with r = 3 (middle), and random fibers with L = 8 (right).

Fig.3.4 shows the number of interface nodes on different electrodes, which represents their surface area. It indicates that when electrode density is small, random electrode has larger surface area. When electrode density is high, random sphere electrode with larger radius has larger surface area.

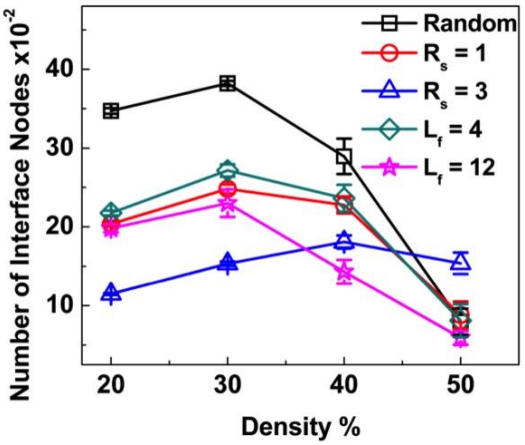

Fig. 3. 4 Comparation of number of interface nodes on different electrodes.

For our first set of simulations, we assumed a random morphology for the electrode and varied the density of the electrode. The 2D system is 512 by 256 lattice units. In real units this corresponds to a distance of 20 times of the Debye length. The thickness of electrodes is 28 lattices (1.1 times of the Debye length in real units). Fig.3.4 indicates that as the electrode density increases, surface area of pure random electrode will increase and then decrease. The maximum surface area of the system is the electrode density of about 30%.

Fig.3.5 shows the total charge and the total interface charge under both PNP and MPNP systems for the random electrodes. It turns out that the total charge is negatively correlated with electrode density, and the system with the highest surface area will not necessarily lead to the highest total charge. This is because of the smaller volume of pores in the electrode material for the electrode with larger densities. Basically speaking, charges have to be saved in the pores, and the volume of available pores will confine the total charge that can be saved in the structure. The total interface charge is highly positively correlated with electrode surface area, instead of the volume of pores, which means at this length scale, the size of the pores does not have very large influence on the distribution of charge at the electrode-electrolyte interface. The MPNP system shows the similar tendencies in both total charge and total interface charge as the PNP system, except that MPNP system tends to have smaller charge values, due to the steric effects, which may hinder the accumulation of local charge (as is shown in Fig.3.6). Also, system with larger electrode density tends to have smaller steric effects. This might be because that most of the accumulation of charge happens in the porous structures, and the electrodes with larger densities have much less pores for this accumulation.

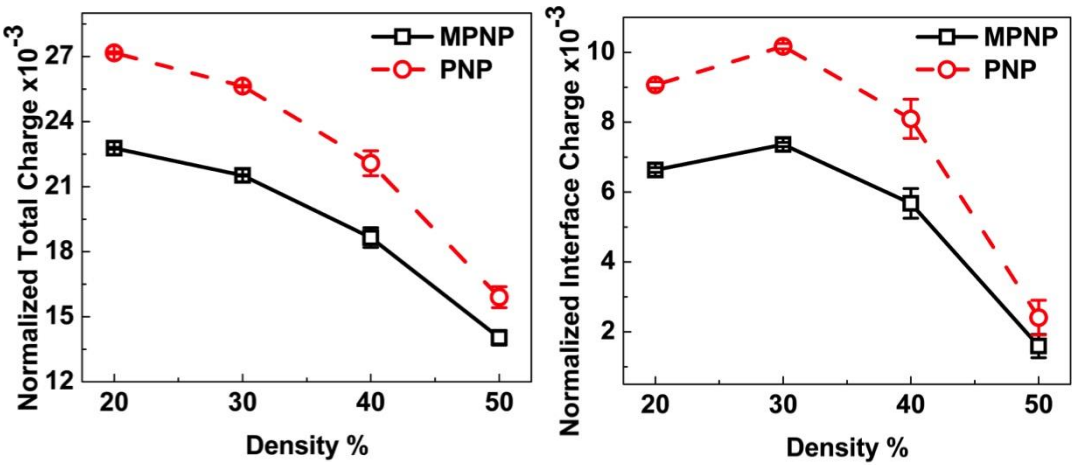

Fig. 3. 5 Total net charge in the whole capacitor system (left) and total interface charge (right)

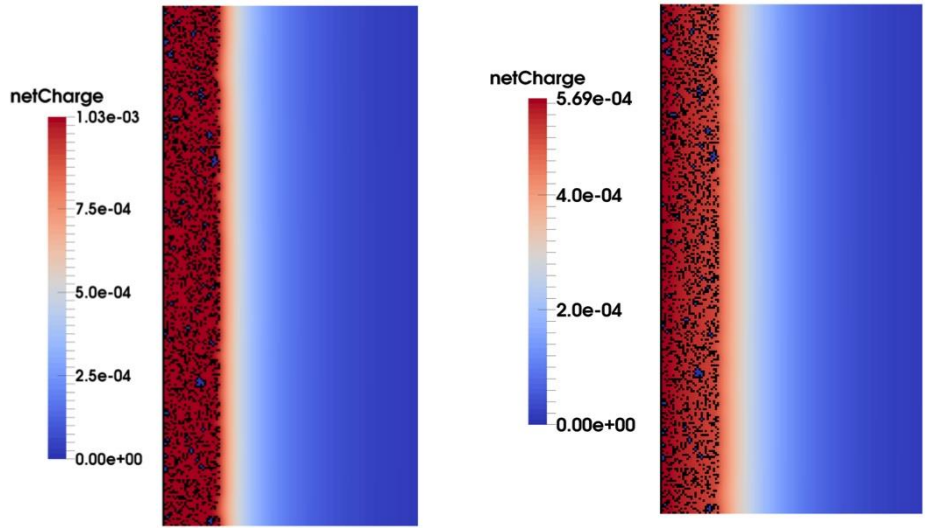

Fig. 3. 6 Net charge distribution in electrode of random morphology with density of 30%, for PNP system (left) and MPNP system (right).

Fig.3.7 shows the time to reach full charge (charge time) in the system. The result shows that charge time will decrease with an increase of electrode density. This is because electrodes with higher densities will have fewer pores to be "filled up" by charges. It is known that mass transfer in porous structures will be slower than in the bulk solution. Therefore, the charge time will decrease with the increase of electrode density. However, when electrode density is below a certain threshold (for example 30% in this case), the averaged charge time will not change too much, indicating smaller influence of pores on the charge transfer dynamics. The variation in the data (at smaller densities) indicates that, in this limit, the charge time is sensitive to the morphology of electrode materials. The MPNP system shows similar tendency of charge time as the PNP system, but with shorter charge time. This is because the steric effects will require less charge to be "filled up" in the porous structure, and therefore, require less charging time.

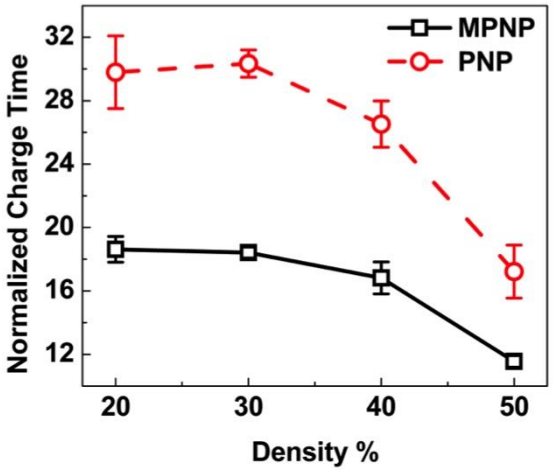

Fig. 3. 7 Normalized charge time in the random electrode system for both PNP and MPNP conditions.

Fig.3.8 shows the equilibrium total charge during the discharge process for both PNP and MPNP systems. Similar to charging processes, the total charge will decrease as the electrode density increases for a fixed applied potential. Higher applied potential will lead to higher total space charge. The total space charge seems to have a linear relation with applied potential under both PNP and MPNP systems. This is mainly due to the very small potential applied in the system. Mathematically speaking, when the applied potential is small, the exponential part of the Poisson distribution can be linearized as a function of local potentials. Therefore the bias could be linear with applied potentials. The slope of the lines indicates the sensitivity of space charge to the change of applied potential. It turns out that the smaller the electrode density, the more sensitive is the total space charge. This might be a result of the larger total volume of pores in the electrode with smaller densities. In this case as well, the MPNP system still has similar tendencies as the PNP system in the charge distribution, but MPNP system will have smaller net charge due to steric effects.

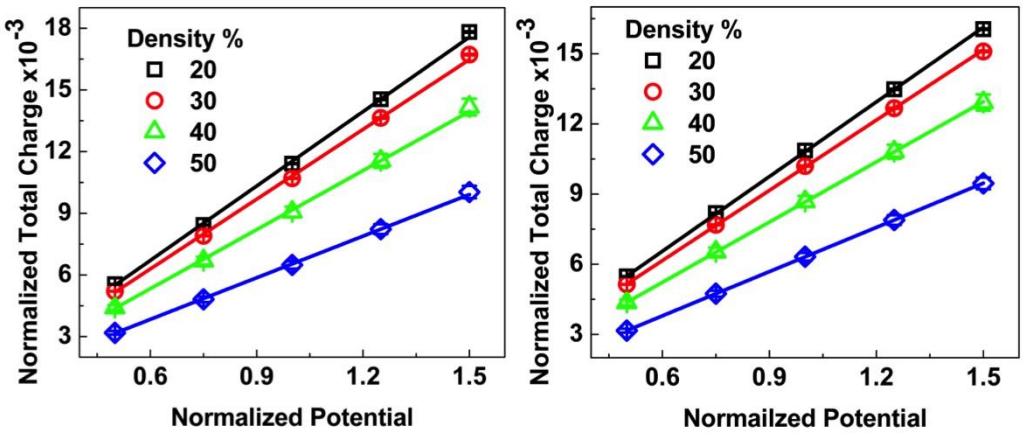

Fig. 3. 8 Total charge during the discharge process for both PNP (left) and MPNP (right) systems on random electrodes.

A big difference between the MPNP and PNP systems, however, is observed when we calculate the discharge time, as is shown in Fig.3.9. Here, we see opposite trends (slopes) in these two systems. In MPNP system, steric effects will push the accumulated charge to move back to the bulk solution at a

faster speed, therefore, it can discharge faster. For PNP system, mass transfer is purely driven by concentration gradient. But in the porous structure, the comparatively slow speed of diffusion will hinder the mass transfer of the inner part of the electrode. In reality, during discharge process, systems with higher potentials should reach equilibrium faster, because they are nearer to the initial state (= 2.0, in our case). Therefore, from the discharge time point of view, only MPNP system gives the right tendency.

Since both systems shows similar tendencies in charge distribution, but MPNP shows the right tendency in discharge time, in the following sections, we will only show the simulation data from MPNP systems.

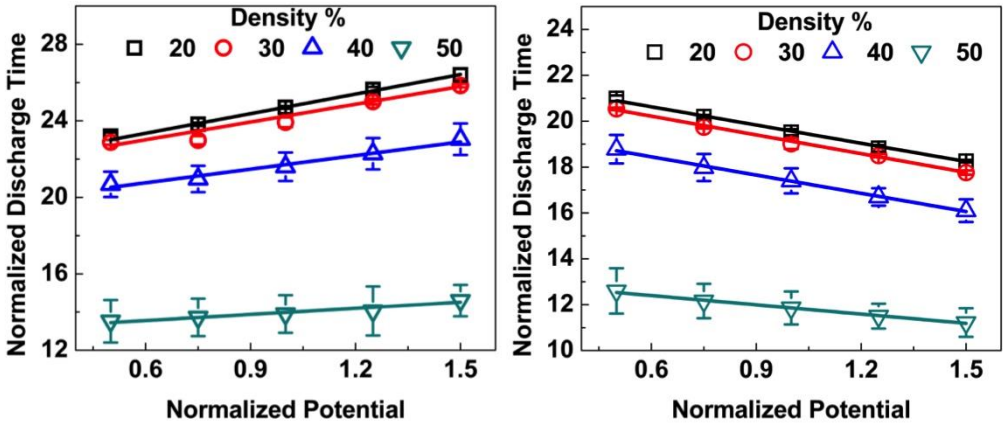

Fig. 3. 9 Discharge time for PNP (left) and MPNP (right) systems on random electrodes.

Fig.3.10 shows the total charge and total interface charge for different electrodes. Total charge will monotonically decrease as electrode density increases, regardless of the electrode morphologies. For the same electrode density, it is possible to optimize total charge by adjusting the morphology of electrode. When electrode density is small, random morphology has more total charge. When electrode density is high, random sphere electrode with larger radius has more total charge. Further, the larger spherical morphology electrode shows the least variation as a function of density. We believe that this is a result of the accessibility of pores in this system being the least affected by density, as we are not near the close packing limit for spheres. Once we go to densities of greater than 40% however, all electrodes show a marked decrease in the total charge.

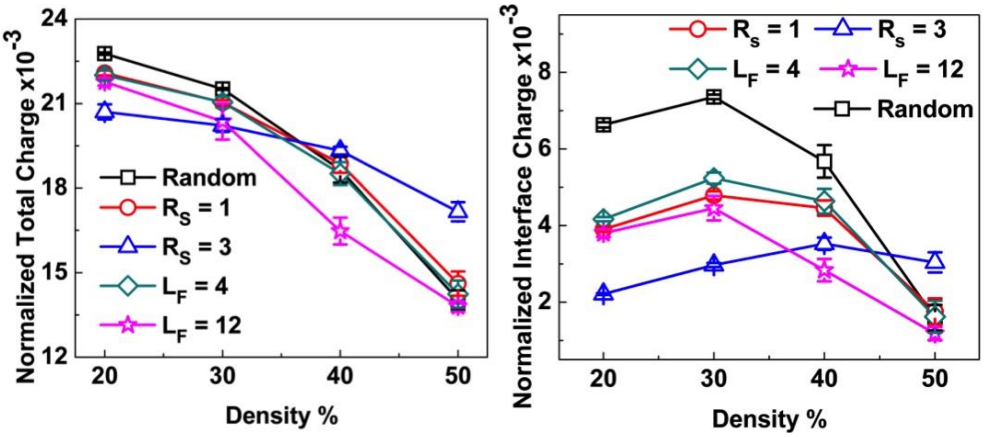

Fig. 3. 10 Total charge (left) and total interface charge (right) for different electrodes.

Fig.3.4 and Fig.3.10 indicate that the total interface charge is governed by electrode surface area. When electrode density is small, random morphology has more total interface charge. When electrode density is high, random sphere electrode with larger radius has more total interface charge.

Finally, we investigate the effect of electrode morphology on the charge time. Fig.3.11 shows the charge time for different electrode morphologies. The result indicates that when electrode density is small, the morphology influence on charge time is not very large. When electrode density is high, large variations can be observed in the charge time, which is mainly resulted from the poor accessibility of some pores inside of the electrode materials. This effect appears to be most pronounced for fiber shaped electrodes, as the accessibility of pores is the most limited in this case.

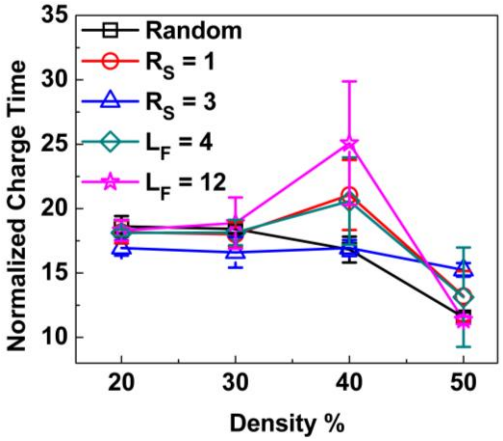

Fig. 3. 11 A comparison of charge time for different electrode morphologies.

3.5 Conclusion

In this chapter, by using Lattice Boltzmann Method, both charge and discharge processes in 2D systems of complex random electrode geometries (pure random, random spheres and random fibers) are investigated. The results show that when electrode density is low, pure random electrode will have higher total space charge in electrolyte, while when electrode density is large, larger sphere electrodes tend to have higher total space charge. The total charge in electrolyte seems to increase linearly with the applied potential in the small applied potential region for both PNP and MPNP systems. Deviation should be observed in larger potential systems, which we will investigate in the future. The total interface charge is governed by the total interface area in the systems.

Steric effect of concentrated solutions is considered by using modified Poisson-Nernst-Plank (MPNP) equations. The MPNP systems tend to have very similar properties as the PNP systems, except that MPNP systems will have smaller charge values due to the steric effects introduced into the systems. However, our results show that the discharge time turns to decrease as the applied potential increases in the MPNP systems, while the opposite tendency can be observed in the PNP systems. This is because the accumulation of charged particles in the pores will block the mass transfer in the inner part of the electrode in the PNP systems, and therefore elongate the discharge time.

Chapter 4. Simulation of Dendrite Formation Process on the Anode of Li-ion Batteries by Using Lattice Boltzmann Method

4.1 Introduction

Lithium ion batteries (LIBs) are one of the most widely used energy storage systems for electrical vehicles and portable devices. Despite the advances made in the battery technology[95-97], a primary failure mechanism in LIBs is the formation of dendrites on the anode during the charging process[98, 99]. This dendrite formation has two importance impacts on the performance of LIB. First, the needle-like dendrite can penetrate through the separator between the anode and cathode, resulting in an internal short. Second, dendrites may break off from the surface of electrode in the discharging process, resulting in capacity fading. Efforts to suppress dendrite formation involve adding additives into electrolyte to either adsorb on the surface of electrode or adjusted the formation of SEI layer[100, 101], coating the separator to maintain a uniform ionic flux and decreasing the surface tension of lithium metal[102], using physical protective layers[103, 104], and designing 3D current collector to confine the growth of dendrite[105]. These methods have not completely alleviated dendrite formation and in order to design better battery systems, we need to have a better understanding of the mechanisms of dendrite formation during battery cycling. In this chapter, we will introduce a LBM model to simulate the dendrite formation process, in order to understand the fundamental processes that control the formation. Our model is able, in contrast to available models in literature, to study both the charge and discharge process, and thus we can observe dendrite formation (and subsequent break-off) and design strategies to optimize battery performance.

4.2 Background

Theoretical models of dendrite formation can generally be categorized into either microscopic or macroscopic models, depending on the length scale of the model. Microscopically, many of the nucleation processes have been simulated by using Molecular Dynamics (MD), which can be used to model the stress and strain effects such as torsion-induced grain growth[133, 134] and additives influences during electrodeposition[135, 136]. In order to include electrochemical reactions into the system, several hybrid methods are developed, such as Molecular dynamics-Monte Carlo (MD-MC) method[137-139] and First-principles molecular dynamics (FPMD)[140]. Another atomic level (or particle level) simulation that is used in electrodeposition system is Monte Carlo (MC). Simulations based on Monte Carlo methods have been developed to investigate the evolution of lattice formation at the atomic level[141], the early stages of electrodeposition[142, 143], the additives effects[144], and so forth. In general, most of the direct MC methods have focused on individual steps of overall reaction mechanisms, rather than on overall mechanisms that consist of a variety of steps and pathways[145]. Both MD and MC methods can provide rich information of near-surface chemistry, detailed reaction mechanisms, or intricate molecular traffic patterns that occur in the course of metal ion reduction and lattice formation, but they can not be used in macroscopic engineering models due to the expensive computational costs. Macroscopically, continuum models are used to simulate electrodeposition processes defined by convection-diffusion equation and the surface chemistry is defined by a series of mean field rate equations. These models have already been used to simulate the effects of additives[146, 147], morphology evolution influenced by several factors (such as surface tension) under different conditions[106, 131, 148]. These models have been used to study dendrite propagation and we briefly review some of them below.

Chazalviel and others[126-129] associated dendritic growth with the Sand's time (when the local ion concentration at the surface of the anode goes to zero). However, during dendrite growth, mass transfer is only part of the story. Monroe and Newman proposed models focusing on the electrochemical kinetic reactions at the electrode-electrolyte interface, which is mainly based on Butler-Volmer equation

(BVE) with surface tension, mechanical forces and deformation effects[106, 130, 131]. These models made predictions about the growth rate of dendrites (constant in later extensions of the Chazalviel model, and accelerating for the Monroe and Newman models). More recently, Ely and Garcia[132] used thermodynamic arguments and phase field models that cast the problem in terms of the stability of a critical nucleus of electrodeposited material, and established principles that control either its growth (into a possible dendrite) or decay. While these models did establish the basic principles that control dendritic growth, they did not take into account any variations in local electrode morphology (albeit through an indirect assumption of non-uniform current density at the surface), and more importantly did not model the discharge process, which can increase the propensity to form dendrites.

In this chapter, we introduce a mesoscopic model that is based on Lattice Boltzmann method (LBM) to simulate the whole charge/discharge cycles on non-idealized geometries of Lithium metal anode. LBM was introduced three decades ago[6, 88], and now it has been developed into a powerful tool for Computational Fluid Dynamics (CFD). This method is particularly successful in fluid flow applications involving interfacial dynamics and complex boundaries[7]. LBM has been used to simulate mass transfer problems in various situations, such as advection-diffusion[89, 149-151], electroosmotic/electrokinetic flows[18-20] and electrochemical systems[23, 24]. It has been applied to simulate interfacial dendrite growth dynamics in alloy solidification[22, 152-154] and crystal growth[21] as well.

Our study shows that the Lattice Boltzmann model can capture all the experimentally observed features of microstructure evolution at the anode, from smooth to mossy to dendritic. We find that the onset time of dendrite formation is sensitive to the initial roughness of electrode but not very sensitive to surface energy. However, once the dendrite begins to propagate, its morphology will be influence by surface energy. Since the dendrite growth cannot be prevented once the system has reached the propagation regime[106], we show that it is possible to predict the formation of dendrites in batteries at a very early stage, by monitoring the rate of change of surface area and examine the effect of cycling the battery.

4.3 Model Details

It is straightforward to divide the battery system into two domains: the electrolyte in which mass transfer takes place, and the electrode-electrolyte interface where the electrochemical reaction happens.

4.3.1 The Electrolyte Domain

If the convection force in the electrolyte is ignored, the ionic transport across the entire cell (outside any molecular-scale compact layers) can be expressed by the time-dependent Nernst-Planck equation[78]:

$$J_j = -D_j \nabla C_j - \frac{z_j F}{RT} D_j C_j \nabla \emptyset \qquad (4.3.1)$$

where J_j is the mass flux of species *j*; D_j is the diffusion coefficient; C_j is the local concentration; z_j is the charge on species *j*; *F* is the Faradic constant; *R* is the ideal gas constant; *T* is the system temperature; $\emptyset$ is the local electrical potential. The first and the second term in equ.4.3.1 denote the diffusion and the electromigration of the charged species respectively. However, the electrical mobility in the electromigration part ($u_j = \frac{z_j F}{RT} D_j$) is based on Einstein equation, which may not be applied to high concentration system. Therefore, in this chapter we calculate mobility based on electrolyte conductivity σ, which is $\sigma_j = z_j\, e c_j \mu_j$. To solve the Nernst-Planck equation, we follow the method in literature in which

the electromigration part was regarded as the advection term in the conventional Lattice Boltzmann Equation for the advection-diffusion lattice[18]. In a single-relaxation-time LB model, this physical system can be expressed as:

$$f_i(\boldsymbol{r} + \Delta t\boldsymbol{v}_i, t + \Delta t) = \left(1 - \frac{1}{\tau}\right) f_i + \frac{1}{\tau} f_i^{eq} \quad (4.3.2)$$

where f_i (**r**, t) is the local density distribution function in the i direction; τ is the relaxation time. The velocity $\mathbf{v}_i$ is chosen so that, in one time step Δt, a particle can reach one of its nearest neighbors. f_i^{eq} is the equilibrium density distribution function. With a simple BGK dynamics, it can be calculated based on the expression:

$$f_i^{eq} = t_i\rho\,(1 + \frac{1}{c_s^2}\,\mathbf{v}_i \cdot \mathbf{u}) \quad (4.3.3)$$

The local drift velocity **u** can be obtained from the electromigration term as we mentioned previously. The microscopic potential distribution in the system should be calculated as the evolution of time in order to obtain the electromigration term in the Nernst-Planck equation. This potential distribution is defined by Poisson's Equation:

$$\nabla^2\emptyset = -\frac{\rho_f}{\varepsilon} \quad (4.3.4)$$

where ρ_f denotes free charge density and ε denotes the electric permittivity. A traditional Successive Over-Relaxation (SOR) method is used to solve the Poisson's equation[94].

4.3.2 The Electrode-Electrolyte Interface

At the electrode-electrolyte interface, we follow a mean field approach, where the magnitude of the local metal cation flux on the growing surface j_c is given by the modified Butler-Volmer (B-V) equation[131]:

$$j_c = j_0 e^{((1-\alpha_1)\Delta\mu_e/RT)}(e^{\alpha_1 F\eta/RT} - e^{-\alpha_2 F\eta/RT}) \quad (4.3.5)$$

Here, j_0 is the exchange current density; α_1 and α_2 are symmetry factors related to the potential barrier for metal cation reduction (in our simulation, α_1=α_2=0.5); R is gas constant; T is temperature; η is the local overpotential, which is given by[148]:

$$\eta = V_{eq} - V_{ext} + \frac{RT}{F} ln(\frac{C_c}{C^{eq}}) \quad (4.3.6)$$

where V_{eq} is the equilibrium potential, V_{ext} is the applied potential, C_c is the local concentration of Li ion at the solid-liquid interface, C^{eq} is the equilibrium concentration of Lithium ions; $\Delta\mu_e$ is the electrochemical potential change in the electrons within the electrode induced by local strain or interfacial shape change. When stress and compression of the electrolyte region are negligible and the electrolyte is 1:1, $\Delta\mu_e$ can be expressed as[106]:

$$\Delta\mu_e = -2\gamma V_M\kappa \quad (4.3.7)$$

where γ is surface energy; V_M is molar volume of Lithium; κ is surface curvature. If we take equ.4.3.7 into equ.4.3.5 and take the $\frac{(2\alpha_1-2)\gamma V_M}{RT}$ part as a constant $\boldsymbol{K}$ (it is called curvature constant in this paper), we can get:

$$j_c = j_0 e^{(K\kappa)}(e^{\alpha_1 F\eta/RT} - e^{-\alpha_2 F\eta/RT}) \qquad (4.3.8)$$

Equ.4.3.8 suggests that the local curvature at the interface has an influence on the local exchange current density (and hence the deposition process). In our simulations, unless mentioned, we use a value of $\boldsymbol{K}$ = 0.005 μm, as this is roughly around the values calculated from the surface energy/surface tension in previous studies[130, 131, 148, 155-157]. We should note that this curvature term actually reflects the inhomogeousity of reactivity at the electrode-electrolyte interface, which is due to the curvature effects. The value of 0.005 μm only indicates that this effect is on the same order of magnitude of surface tension. Other effects, such as stress, compression of the electrolyte region, the specific adsorption on the low curvature regime, and the formation of SEI, may have much larger influence than surface tension; therefore we may have a large spectrum of $\boldsymbol{K}$ values for different systems.

The local curvature κ, is calculated by using the virtual front tracking model[158], which gives the local curvature:

$$\kappa = [\left(\frac{\partial f_S}{\partial x}\right)^2 + (\frac{\partial f_S}{\partial y})^2]^{-3/2}[2\frac{\partial f_S}{\partial x}\frac{\partial f_S}{\partial y}\frac{\partial f_S}{\partial x \partial y} - \left(\frac{\partial f_S}{\partial x}\right)^2\frac{\partial^2 f_S}{\partial y^2} - \frac{\partial^2 f_S}{\partial x^2}(\frac{\partial f_S}{\partial y})^2] \qquad (4.3.9)$$

where f_S denotes local solid fraction. This equation is solved by a simple centered finite difference method[159].

The evolution of electrode-electrolyte interface during charge/discharge process is monitored by the local solid fraction distribution, f_S, which is defined as the volume fraction of solid at each lattice node. During the charging process, we assume the nodes fully occupied by Li metal, where f_S = 1.0, as a part of anode, while the nodes with f_S < 1.0 as electrolyte. Only the electrolyte nodes that have at least one nearby anode node can have deposition reaction (the number of nearby anode nodes is also counted into the local reaction). During discharge process, same criteria applied, but we regard the node with f_S = 0 as electrolyte and f_S > 0 as anode. Only the anode with at least one nearby electrolyte can have a dissolution reaction and the interface numbers are also counted into the local reaction. In this model, we also added a cluster-tracing step to distinguish between linked and unlinked solids. Only the interface between linked solid and electrolyte will have an electrochemical reaction. We also assume the unlinked solid will stay static in electrolyte until the end of a charge/discharge cycle when they are cleared away from the system. Once an electrolyte node becomes an anode node, bounce back condition will be applied; while when an anode node becomes an electrolyte node, BGK dynamics will be applied.

4.3.3 Boundary Conditions and System Parameters

In the paper, we tested our simulation approach by using a 400 x 400 D2Q5 lattice to represent a cell size of 0.4mm x 0.4mm. In our simulations, unless mentioned, we keep the cell thickness a constant of 0.4mm. Charge/discharge processes are carried out on a Li metal anode within a binary electrolyte (without any supporting electrolyte). Bounce back conditions are applied at the two parallel electrodes for mass transfer equations. Periodic boundary conditions are applied at the other two sides of the system to represent infinite length of electrodes. The initial thickness of anode is 0.025mm (given that inhomogeneous dissolution will take place during discharge process); the thickness of cathode is 0.001mm. The reaction speed constant, k = 1.3e-4 mm/s, which is used to calculate the exchange current density. The mobility of the Li and the PF_6 ions were both fixed at 1.0e-3 $mm^2/(s\ V)$, which represents the electrolyte (1 M) conductivity of about 2 mS/cm. Note that the conductivity from other papers[160-162] is around 6 to 10 mS/cm. Considering the local ion concentration in the cell may drop to very low values, we used a little bit smaller value, but it is still in the same magnitude. The temperature T was kept constant at 298K and the dielectric constant of the electrolyte was fixed at 46.44. We used diffusion constants for the Li and PF_6 ions equal to 2.0e-4 mm^2/s and 1.0e-4 mm^2/s respectively. The bulk

concentration of Li ion was initialized at 1.0mol/L. All our simulations are run under constant current density conditions, unless otherwise specified. The applied potential on the anode will be adjusted in every time step to maintain the constant current density, and the potential of cathode is kept constant as 0 V. Potentials in the system are referred to the equilibrium potential of $Li|Li^+(1M)$ reference electrode at 298K and 1 atm. We note that where possible all the values that we use are from the experimental literatures as we wanted to make our model as predictive as possible. In all the simulations our unit of length is 1 micron, and we started off by initializing our anode with an rms roughness of 1 micron. The roughness of the system is governed by the standard deviation of normal distribution, σ. Fig.4.1 shows the system initial morphologies and the relationship with σ. All our results are averaged over 10 different initial states of the rough anode surface with the same σ value. Since we are only interested in the reactions at the anode, cathode reactions are simplified by a constant homogenous inlet/outlet flux of Li^+ with zero velocity so that the conservation of mass in the cell system can be maintained.

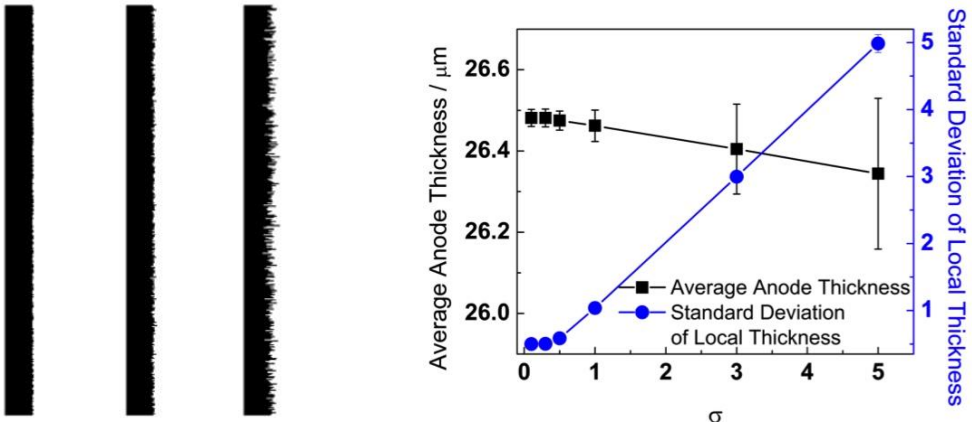

Fig. 4. 1 Initial roughness of the anode; (left) shows the morphologies when σ = 0.1, 1.0 and 3.0 (from left to right); (right) shows the relationship between σ, the average anode thickness and the local thickness. Note that the base line of the anode is 25 μm

While the B-V equation defines the kinetic reactivity at the electrode-electrolyte interface, the amount of Li ions that are available can be limited by the mass transfer in the electrolyte. At low overpotentials, kinetic reactivity dominates this process; at high overpotentials, mass transfer dominates.

4.4 Results and Discussion

4.4.1 Current Densities and Applied Potentials

In a 2D system, only a line current density (mA/cm) is available. In order to compare our results with experiments, we normalized our current density with respect to the diffusion limiting current density (J_{diff}) of the system. The J_{diff} is obtained by applying fixed potentials on a flat anode, keeping everything the same as our targeted system, but turning off electromigration and morphology change. As the overpotential increases, the steady state current density of the system will reach an upper limit, which is J_{dff}. As is shown in Fig.4.2a, the J_{diff} for the 0.4mm cell is around 0.001 mA/cm. Note that J_{dff} is only governed by pure diffusion of Li ions and the cell thickness (because of inlet flux at the cathode), so a real battery system with electromigration and growth of deposition layer can have much larger current density than J_{diff}. Also the J_{diff} in our system may be higher than actual limiting diffusion current in a real battery system since the separator between two electrodes will decrease the apparent diffusion speed.

Fig.4.2b shows relationship between steady state currents and applied potentials when electromigration is considered. The good linearity in the high potential regime indicates the mass

transport is essentially Ohmic. Sawada etc. suggested that in this regime, transport by diffusion can be neglected[163]. In the low applied potential regime, the deviation from that linearity indicates a transition from electromigration dominant process to diffusion dominant process. It is noted here that this transition is not a result of the reaction kinetics at the electrode-electrolyte interface, since if we change the cell thickness (shown in Fig.4.2c), the current densities around the transition potentials will change correspondingly, indicating a mass transfer dominant process. Also we notice that, in spite of the cell thickness, the transition potential is about -0.2V. The transition current density (J/J_{dff}) is about 1.5 for the 0.4mm cell and about 2.0 for the 0.3mm cell.

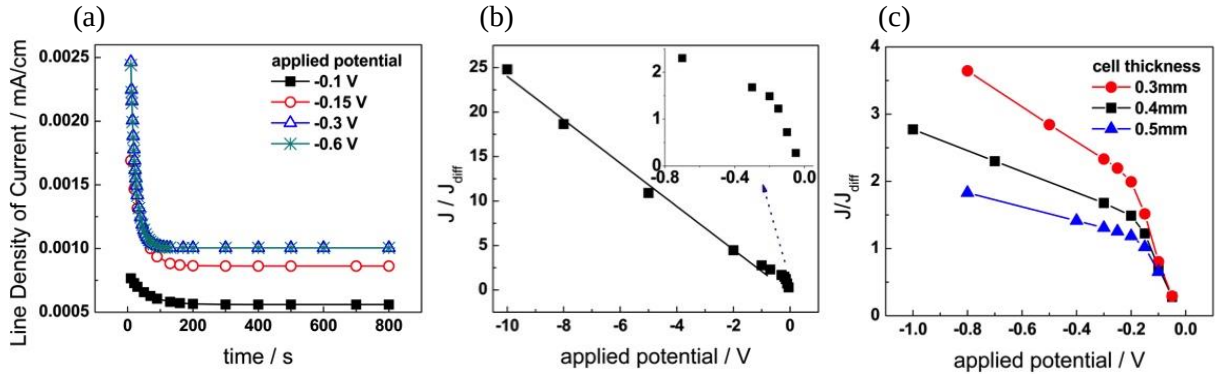

Fig. 4. 2 (a) Current density at fixed potential system without electromigration and morphology change for cell thickness of 0.4mm. (b) Steady state current density at fixed potential system with electromigration but without morphology change for cell thickness of 0.4mm. (c) Steady state current density at fixed potential system with electromigration but without morphology change for cell with different thicknesses.

Next, we go further to add morphology changes of deposits and switch to a constant current density condition. Fig.4.3 shows the morphologies of the deposits under different current densities ($\boldsymbol{K}$ = 0.005 μm, $\sigma = 0.1$). We can observe a transition from mossy to dendritic structure at the current density of around 1.75.

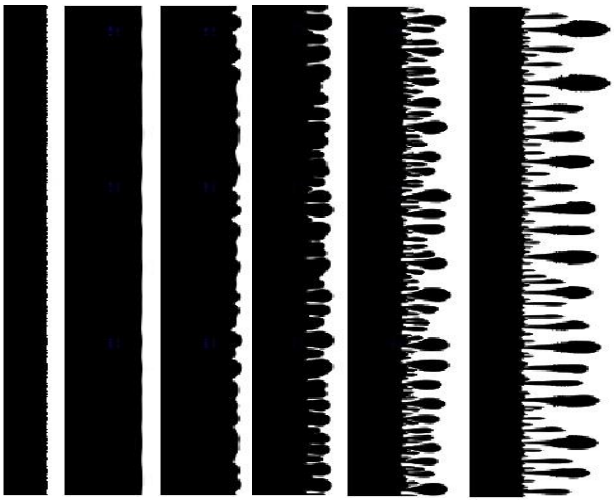

Fig. 4. 3 Morphologies of deposits under different current densities ($\boldsymbol{K}$ = 0.005 μm, $\sigma = 0.1$). The current density are J/J_{diff} = 0, 1.5, 1.7, 1.75, 1.85, 2.0 from left to right.

Fig.4.4 compares the applied potentials of the cell system with and without morphology change. For the system without morphology change (Fig.4.4a), the applied potential will firstly drop due to concentration polarization that drives the equilibrium potential away from the standard equilibrium potential, and then reach a steady state. For the system with morphology change (Fig.4.4b), when the current density is small, the applied potential will also drop and then oscillate around a steady state. This oscillation may be due to the roughening of the anode surface. When current density increases, the applied potential will first decrease and then increase. This increase is mainly a result of an increase of surface area, which is the consequence of forming mossy and dendritic structures on the surface, and a decrease in cell thickness, which results from the deposits on electrode surface. The critical current density when dendrites form in the system is within the range of 1.5 to 2.0, which indicates the transition point from diffusion to electromigration dominant process as we mentioned before (Note that as deposition time goes on, the cell thickness is decreasing. Therefore, when the mossy/dendritic structure forms, the actual cell thickness is exactly within the range of 0.3 to 0.4 mm as well). Because of the increases of surface area and decrease of cell thickness in these systems, the applied potentials in Fig.4.4b are more positive than Fig.4.4a when the current density is the same.

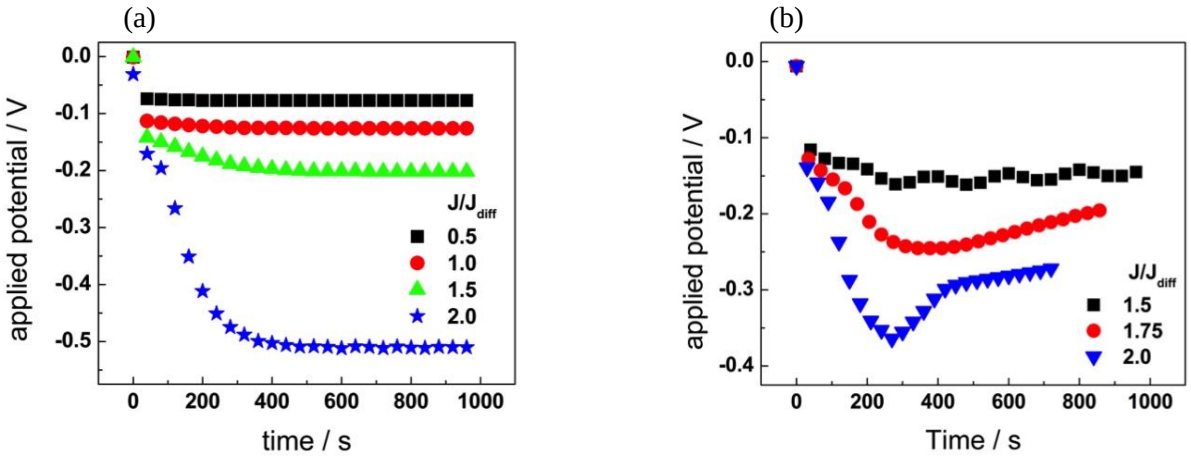

Fig. 4. 4 Change of applied potentials. (a) System without morphology change. (b) System with morphology change.

Fig.4.4b also shows that for the mossy and dendritic structure systems, the applied potential will fall below -0.2V, which is also the very potential for transition from diffusion dominated process to the electromigration dominated process. Diffusion tries to homogenize ions distribution, while electromigration accelerates growth of deposits on high curvature regimes. More specifically speaking, mossy structure forms at the potentials near the transition point, while the dendritic structure forms at the potentials that the system is dominated by electromigration. Similar results have been confirmed both experimentally[164] and theoretically[123], where the growth speed of dendrite is governed by electrical field intensity.

4.4.2 Electric Field Distribution

Since the growth of dendrites that form at high current density is governed by electromigration, the electric field in the system will play a very important role in the morphology formation process. Fig.4.5 shows the electric field intensity distribution in the system that dendrite forms.

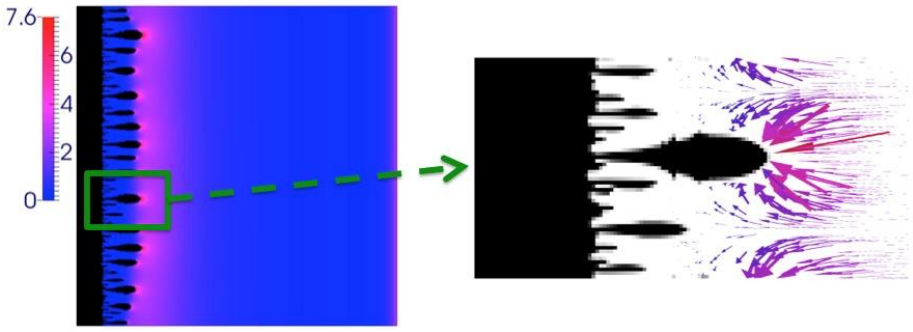

Fig. 4. 5 Electric Field Distribution for dendritic system under charging process. Intensity of electric field (left). Electrical force on Li ions at the vicinity of a dendrite (right).

Fig.4.5 shows that the electrical field intensity is high at the tips of big dendrites; on the contrary, the intensity is very small at the vicinity of small dendrites. The electrical force will drive Li ions to move, at higher speed, towards the tip of big dendrites during charging and outwards from the tip regime during discharging. Therefore, once dendrites begin to form, the inhomogeneous distribution of electrical field will accelerate the growth of big dendrites, while the growth of smaller dendrites that are between big dendrites will be suppressed.

4.4.3 Concentration Distribution of Li Ions and Sand's Time

It has been proved that during the dendrite formation process, when current density is high, the ionic concentrations in the vicinity of the negative electrode drop to zero at the Sand's time[127]. The higher current density is, the lower Li ion concentration at the surface of anode will be. Here, we observe similar results in the simulation. The data in Fig.4.6 shows a depletion of Li ion on the surface of the deposited Li, and as the current density increases, the surface concentration of Li ion decreases, which is due to the higher local electrochemical reaction rate under the higher current density condition.

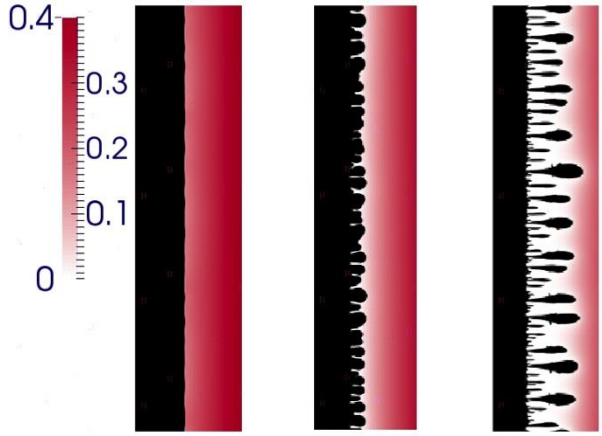

Fig. 4. 6 Distribution of Li ions at the vicinity of anode during charge process. The current densities (J/J_{diff}) from left to right are 1.5, 1.75, and 2.0 respectively.

The "Sand's time", τ, which is the time when system concentration drops to zero, can be calculated based on the following equation[127]:

$$\tau = \pi D \left(\frac{C_0 e}{2 J t_a}\right)^2 \qquad (4.4.1)$$

where $t_a = \frac{\mu_a}{\mu_a + \mu_c}$ is the anionic transport number, $D = \frac{D_c\mu_a + D_a\mu_c}{\mu_a + \mu_c}$ is the ambipolar diffusion constant for the salt. Fig.4.7 shows the relation between current density J and the Sand's time in our simulation. The results show that when current density is high, our simulation is in accordance with theoretical result. But the simulation results deviate from the theoretical value when current density drops. We believe this deviation is a result of three main factors: First, the roughness of anode, which results in an inhomogeneity in the local electric field and larger actual surface area. As is shown in Fig.4.7a, higher roughness system tends to have shorter Sand's time. Second, the constant inlet flow from the cathode boundary breaks the semi-infinite assumption of the theoretical system. In the thin cell system, when the current density is comparatively small, the inlet flux can transfer to the surface of anode before the system reaches the theoretical Sand's time, which increases mass transfer speed at the anode surface, and therefore increase the Sand's time. However, when current density is high, in the much shorter Sand's time, the inlet flux may not have transferred to the anode, and thus has little influence on the Sand's time. Third, the deposits before Sand's time is reached actually decrease the cell thickness, leading to larger Sand's time. It turns out that the last two effects have larger influences in our system.

By comparing Fig.4.7a and b, we also notice that the Sand's time is sensitive to the initial morphology and the curvature constant. However, when the roughness of anode is above a certain threshold (about σ = 1.0), the curves turn to be identical, which indicates that the surface roughness has a limited influence on the Sand's time. We also observe shorter Sand's time as the curvature constant $\boldsymbol{K}$ increases to a much larger value ($\boldsymbol{K}$ = 1.0). This indicates that when curvature constant is very large, it will have an influence on the Sand's time as well. Indeed, the curvature constant $\boldsymbol{K}$ may have much larger value than 0.005 when we consider the stress and compression of the electrolyte region in the calculation of $\Delta\mu_e$ in equ.4.3.5. Monroe and Newman pointed out that surface tension contributes minimally to electrode stability in comparison to the much larger impacts of compressive and deformational forces acting across the interface with solid electrolytes[131], and gave out the full expression of $\Delta\mu_e$ as well[106]. We also believe that the formation of solid electrolyte interphase (SEI) will have a great impact on the surface deformational forces, resulting in large $\boldsymbol{K}$ values.

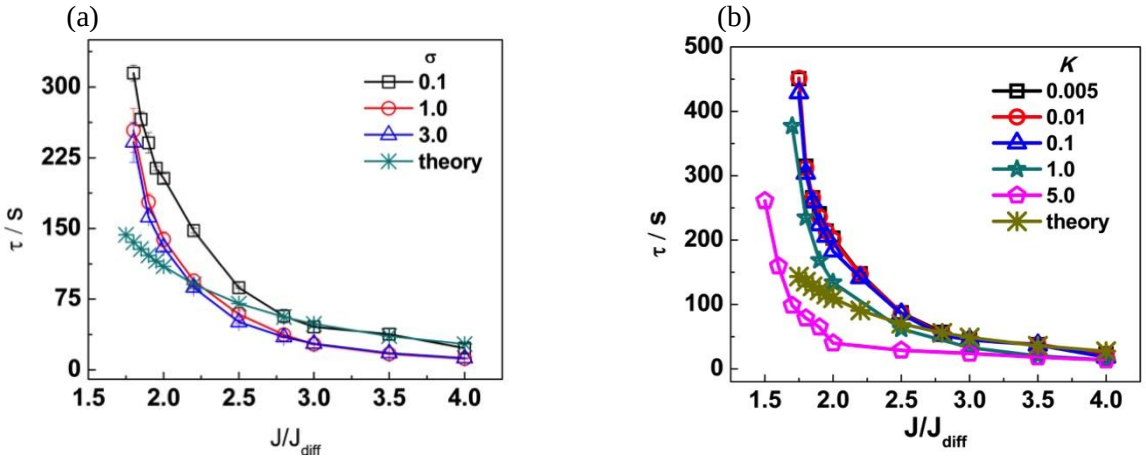

Fig. 4. 7 Relationship between Sand's time and current density. (a) Systems with different initial roughness (σ denotes roughness) for constant $\boldsymbol{K}$ = 0.005. (b) Systems with different curvature constants for constant σ= 0.1.

It is believed that when current density is not high, the ionic concentration profile evolves to a steady state and local concentration will not go to zero. Dendrite formation may follow Monroe and Newman's model which is surface reaction controlled[130]; while at high current density, the local

concentration will go to zero at anode at sand's time, and Chazalviel attributed the dendrite formation to the local space charge associated with a large electric field[126]. The crossover value J^* is given by:

$$J^* = \frac{2eC_0D}{t_aL} \qquad (4.4.2)$$

where L is the distance between two electrodes. In our system the critical value of J^* calculated from equ.4.3.2 is 15.4 mA/cm^2, which is 1.54×10^{-3} mA/cm in line density (J^*/J_{diff} = 1.54) when the cell thickness is 0.375 mm (the thickness of initial anode is 0.025 mm). And actually, the lowest current densities we can observe zero concentration is J/J_{diff} = 1.75 when the curvature constant is not very large ($\boldsymbol{K} = 0.005$ ~ 0.1, shown in Fig.4.8). This is a little larger than the theoretical crossover current density. It is possible that this is a result of the inlet flow on the other side of the cell, which will increase the value of C_0, and the decreased cell thickness due to the deposits before sand's time, which decreases the value of L. However, we do observe smaller crossover current density when the curvature constant is very large (when $\boldsymbol{K} = 1.0$, J^*/J_{diff} = 1.6 and when $\boldsymbol{K} = 5.0$, J^*/J_{diff} = 1.45, shown in Fig.4.8). But the crossover current density is not very sensitive to surface roughness. Therefore, it seems that the curvature constant, which denotes the inhomogeneity of reactivity at electrode-electrolyte interface, has larger influence on the critical current density that whether the system will form mossy or dendrite structures, while once we are above the critical current density, the formation time of dendrites is more sensitive to anode roughness.

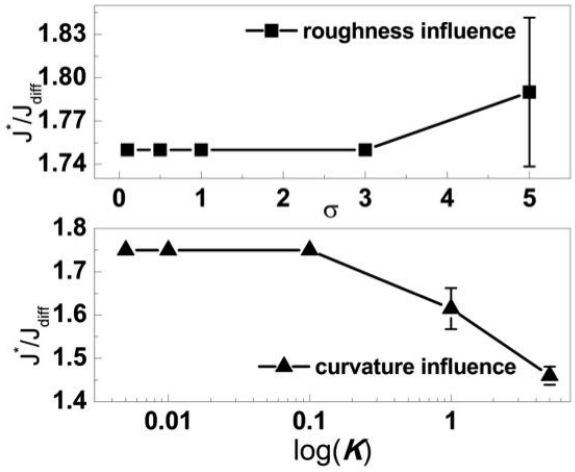

Fig. 4. 8 Crossover current densities for different roughness with constant $\boldsymbol{k}$ = 0.005 (up) and different $\boldsymbol{K}$ with constant σ = 0.1(down).

Liu etc.[165] also reported that in experiment they observed good linearity of $\log\tau$ vs. $\log J$ when current densities are much larger than the critical value J^*. They noted that in this regime, the dendrite growth could be explained by the local inhomogeneities of ion concentrations, which was indicated by Rosso etc.[166]. Fig.4.9 shows the relationship between $\log\tau$ and $\log J$. It reflects good linearity when the current densities are larger than 1.82 ($\log(J/J_{diff})$ = 0.26) in all cases, which is also larger than the crossover current densities we mentioned before. A comparison of Fig.4.9a and b shows that this linearity may hold in almost the entire spectrum of current densities when curvature constant is small and roughness is large, but for high curvature constant systems, the deviation is obvious. An interesting observation shows that this deviation point is not sensitive to curvature constant, which indicates this process is not surface reactivity governed. A possible explanation is that it reflects the transition of electric field governed mass transfer to diffusion governed mass transfer. As we shall see in the next section (Fig.10), this transition point is very close to the transition current density that system morphology changes from mossy structure to dendritic structure. And the reason why we could not observe the

transition in Fig.4.9a when surface roughness is large is because very large roughness is equivalent to say that the system is dendritic initially (Fig.4.1). And the large potential field at the tip of the initial "dendrites" will dominate the growth at the beginning of deposition.

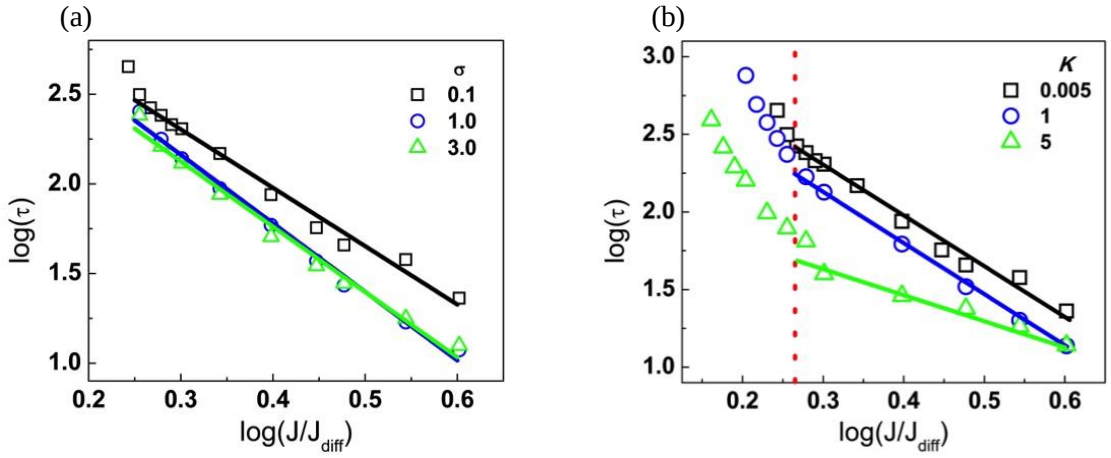

Fig. 4. 9 Relationship between $\log\tau$ and $\log J$ for (a) different roughness (with constant $\boldsymbol{k}$ = 0.005) and (b) different $\boldsymbol{K}$ (with constant σ = 0.1).

4.4.4 Morphologies of Deposits and Change Rate of Surface Area

Our model can capture all the experimentally observed features of microstructure evolution at the anode, from smooth to mossy to dendritic. Fig.4.10 shows the morphologies under different current densities for different surface roughness and curvature constants. We can observe that when current density is not large, increasing either roughness or curvature constant will lead to rougher surface. Higher curvature constant turns to have earlier mossy structures, but the transition from mossy structure to dendritic structure happens at almost the same current density, which is around 1.7~1.8, no matter whether the system has larger curvature constant or larger roughness. These results further confirmed our previous conclusion that the crossover current density, which defines whether the system will form dendritic or mossy structure, is governed by the inhomogeneous surface reactivity (curvature constant); while the transition current density for dendrite formation is governed by the relative speed of diffusion to electromigration, which may indicate the transition from mossy to dendritic structure. This transition is governed by the diffusion coefficient, mobility and the cell thickness. These parameters are fixed in our model, so we obtained almost similar transition current density when dendrite forms. When curvature constant is large, system seems to have larger current density regime to form mossy structure, which indicates that mossy structures are easier to be obtained in high curvature constant systems.

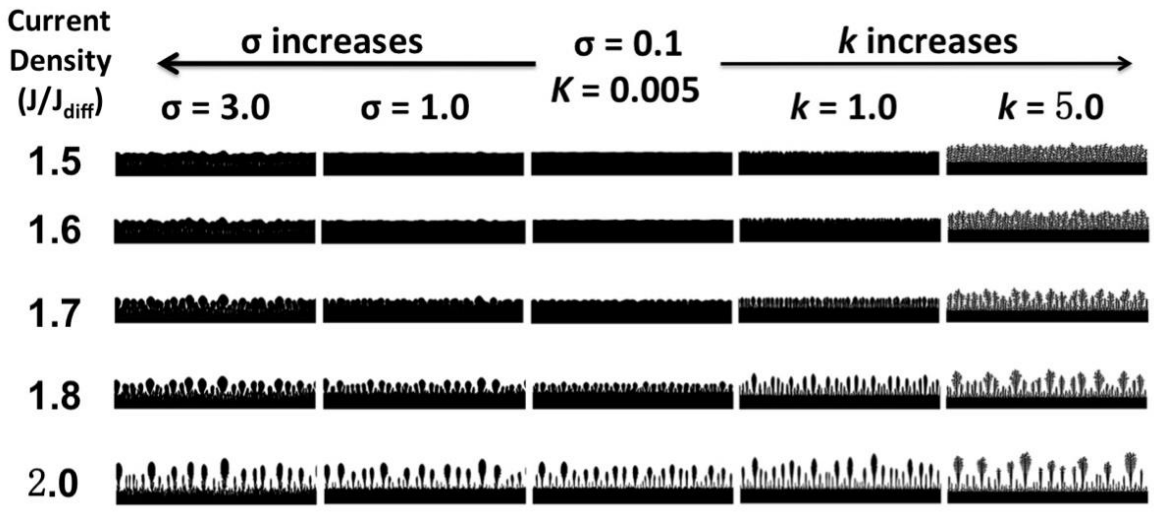

Fig. 4. 10 Morphologies of deposits under different current densities for different surface roughness and curvature constants.

However, when curvature constant is extremely large (for example, $\boldsymbol{K}$ = 20), we do observe dendrite formation at very small current densities. Fig.4.11 shows that when $\boldsymbol{K}$ = 20, we can observe dendrite formation even at the current density of 0.1, which is one order of magnitude smaller than the theoretical crossover current density. And we can observe dendrite structures at high current densities as well. However, the morphologies of the dendrites are different. For small current density, the dendrite is needle-like, while for large current density, the dendrite is branched, and it is large at the head and small at the "neck" that connects the dendrite to anode. Similar morphologies have been observed in experiment for Li deposition as well[127]. When curvature constant is extremely large, the deposition is governed by interface reactivity at very small current density. The large curvature constant will lead to uneven reactivity at the surface and thus form dendrites.

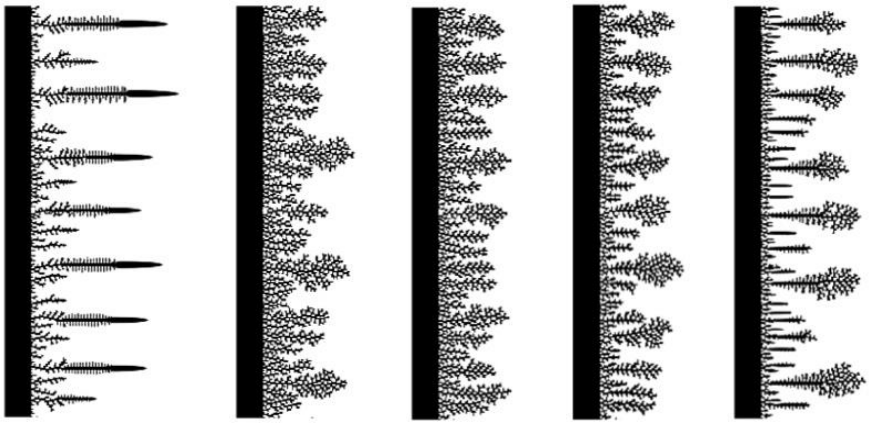

Fig. 4. 11 Morphologies of deposits under extremely large curvature constant system ($\boldsymbol{K}$ = 20); the current density (J/J$_{diff}$) are 0.1, 1.0, 1.5, 1.7, and 2.0 from left to right.

Now we can have a whole picture of the story: when the curvature constant is not extremely high, there are two transition current densities in the deposition system. One is the crossover current density, which is governed by inhomogenous surface reactivity and denotes the transition from flat/rough structure to mossy/dendritic structure. The other is the critical current density that is governed by the relative speed

of diffusion to electromigration, which denotes the transition from mossy structure to dendritic structure. For high curvature constant systems, there is larger current density regime for mossy structure formation; for low curvature constant system, the regime is small, and sometimes it may not be easy to observe the mossy structure and the system will turn into dendritic structure directly. When curvature constant is extremely high, dendrite may form at small current density condition, which is mainly governed by highly inhomogenized reactivity.

While the Sand's time reflects the initial stage of the deposition process, it does not provide any information of the ongoing process of dendrite growth. Here we introduce a way to monitor dendrite growth by tracing the change rate of solid-liquid interface area. Fig.4.12 shows a typical curve of change rate of surface area when current density is high (J/J_{diff} = 2.0). We can divide this curve in to several regions: 0 to 203 s, curve is almost flat, and dendrite does not form in this region since it has not reached the sand's time (averaged τ = 203 □ for this system); 203 to 330 s, surface area increases at accelerated speed due to the initial growth of lots of small dendrites; 330 to about 555 s, surface area goes on increasing, but at decreasing speed, because some big dendrites forms and their growth suppresses the growth of smaller dendrites; 555 to 750 s, surface area still go on increasing with decreasing rate, since the growth of big dendrites decreases cell thickness, the deposition gradually change from electrochemical reaction controlled to mass transfer controlled, thereafter, the growth of the big dendrites is mainly in width rather than in length.

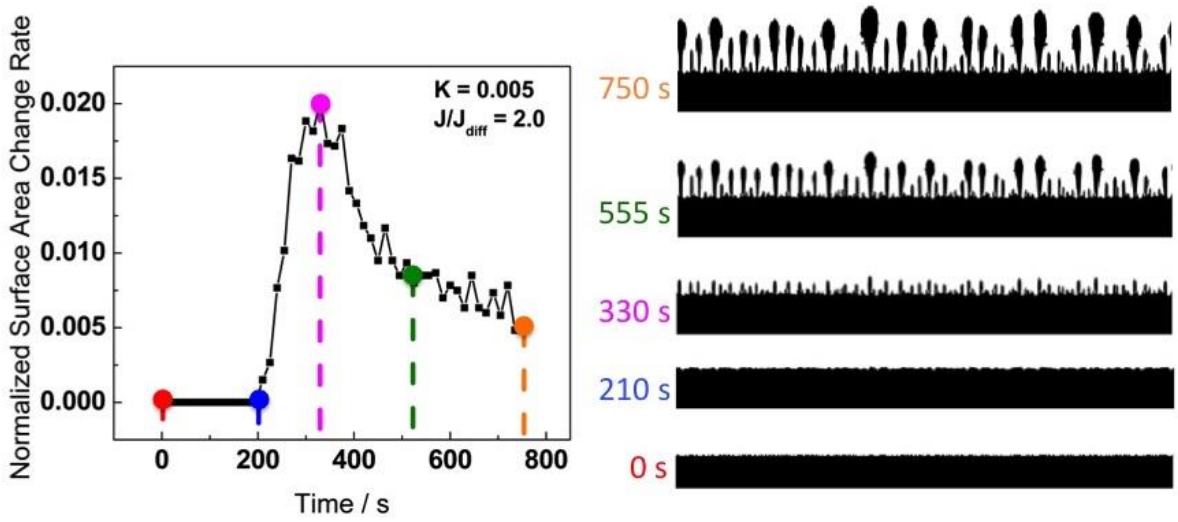

Fig. 4. 12 Change rate of surface area for a single system with current density (J/J_{diff}) of 2.0 (left) and the corresponding morphologies of the system at different times (right).

By comparing the change rate of surface area for different current densities, we can clearly observe a transition current density that dendrite will form or not in the system (Fig.4.13). Once an initial dendrite forms, it will automatically grow at a faster speed than its surroundings, thus, the change rate of surface area will be much higher than non-dendrite system. We can actually use this to predict dendritic system even before big dendrites form. Fig.4.13 also indicates that the onset time for surface area increasing is almost the same as the sand's time of the system, which also proves that dendrites will begin to grow and accelerate the growth after sand's time. Similar tendency can also be observed in higher $\boldsymbol{K}$ and σ systems but with larger fluctuations.

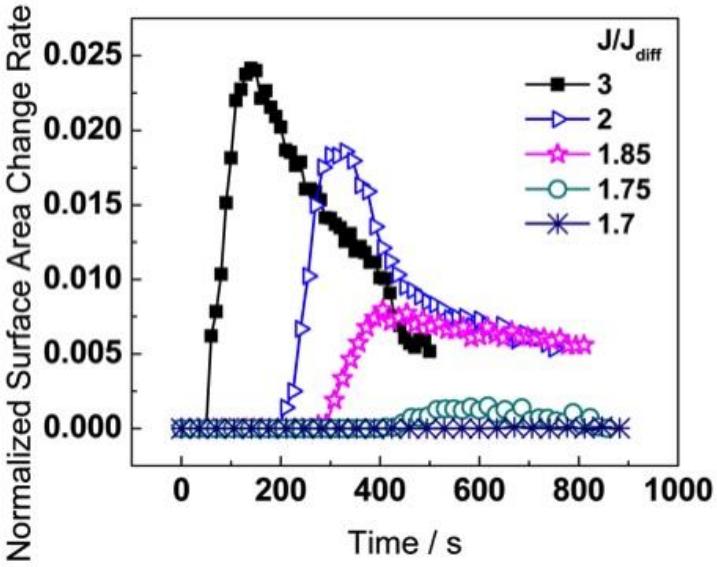

Fig. 4. 13 Change rate of surface area under different current densities (This data is averaged over 10 different initial morphologies).

It is argued that some dendrites may form from the concentration depletion region. As is shown in Fig.4.14, our simulation shows that at high current density condition, there can be an ion depletion layer at the interface, and the final dendrite will form exactly at the positions where there are initial small protrusions. The ion depletion layer for these protrusions will develop into the bulk electrolytes, resulting in a "roughness" of depletion layer as well.

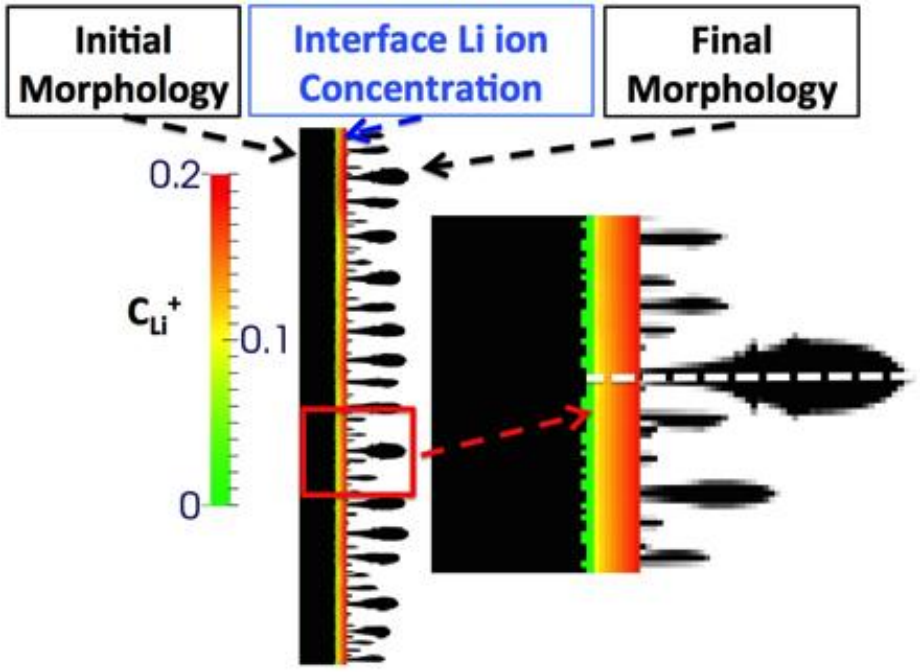

Fig. 4. 14 Position of dendrite and the concentration distribution at the interface.

4.4.5 Discharge and Cyclic Properties

Following the same procedure, our model is capable to simulate the discharge process as well. Fig.4.15 shows the discharge of a single dendrite system. It shows that during the discharge process, the dendrite may break off from the anode. The unlinked Li metal will be excluded from the battery cycles in the future and thus result in capacity fading. It seems that once dendrite forms, some part of it will break off from the anode no matter how small the discharge current density is. However, we note that this is only for a single dendrite, and for a system with multiple dendrites, the dissolution of nearby dendrites will definitely have influence on each other.

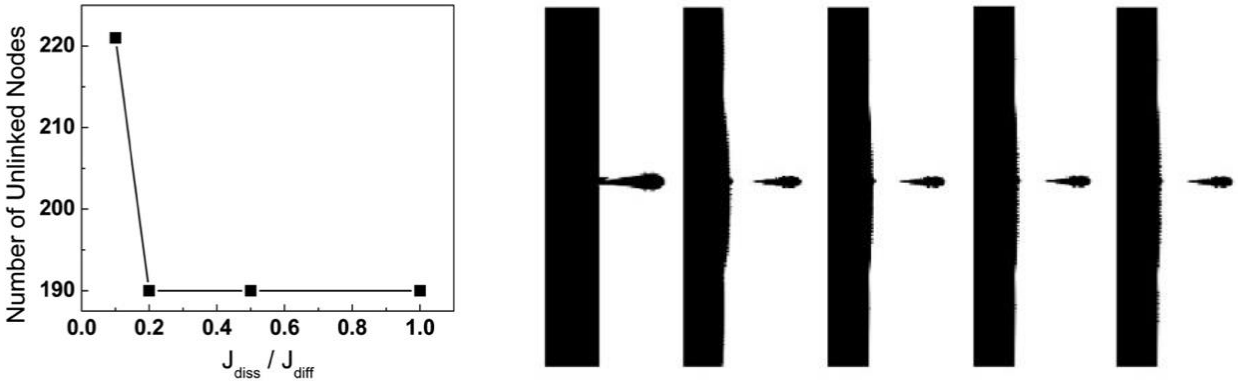

Fig. 4. 15 Discharge of a single dendrite system. (left) Number of unlinked nodes as a function of discharge current density. (right) Morphologies of the system (current densities (J_{diss} /J_{diff}) are: 0, 0.1, 0.2, 0.5, and 1.0 from left to right).

An interesting observation is that higher discharge current density seems to result in smaller amount of unlinked solid, and the same tendency is observed in the random morphology systems with multiple dendrites form (Fig.4.16). We believe the smaller amount of unlinked solid at higher discharge current density is due to concentration polarization at the electrode-electrolyte interface. Fig.4.16 shows that the concentration of Li ions is higher at the base of the dendrite than the tips. The higher local concentration will influence the equilibrium potential and lead to smaller overpotential at the "neck" of the dendrites. The higher the discharge current density, the larger the local concentration, and thus the larger concentration polarization can be expected. The high local concentration at the base of dendrites might be a result of the much smaller electrical field at the base and the steric effect.

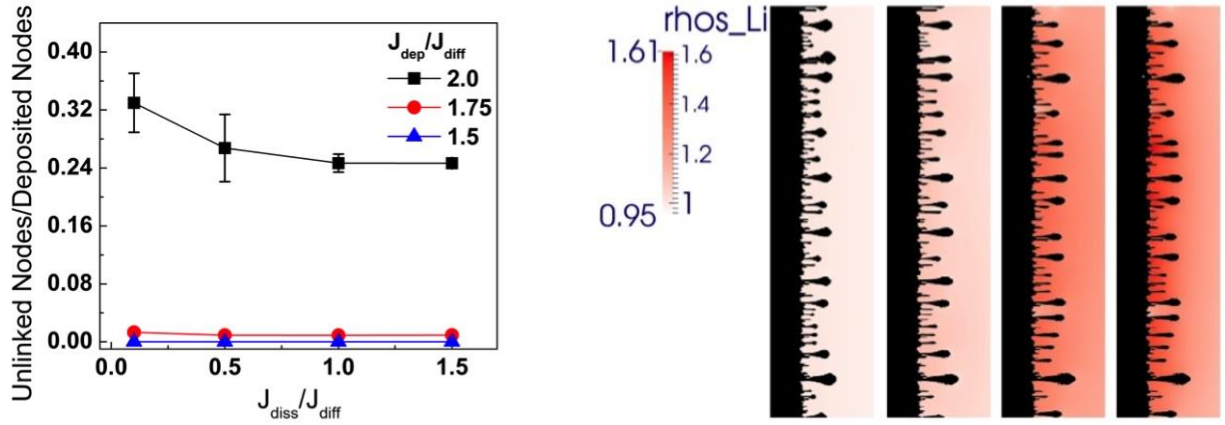

Fig. 4. 16 Discharge of random morphologies. (left) Number of unlinked nodes as a function of discharge current density. (right) Concentration of the system at the initial stage of discharge (current densities (J_{diss}/J_{diff}) are: 0.1, 0.5, 1.0, and 1.5 from left to right).

The advantage of LBM is that it can be parallelized very easily and we can simulate the charge/discharge cycles directly. Fig.4.17 shows the applied potential and current density changes in the charge/discharge cycles for two systems, one is dendritic and the other is non-dendritic, and with the same discharge current of 0.5 as an example. The results confirm that we can get stable current density in the cyclic system. But the applied potential may vary from cycle to cycle at the beginning of the whole process when charge current density is comparatively high. While for lower charge current density system, the applied potential is stable at beginning, and then begins to vary after about 10 cycles. The applied potential change reflects the morphology changes in the system. As we shall see in Fig.4.19, large variation of applied potential indicates dendrite formation or break off, while small variation indicates adjustment of local roughness.

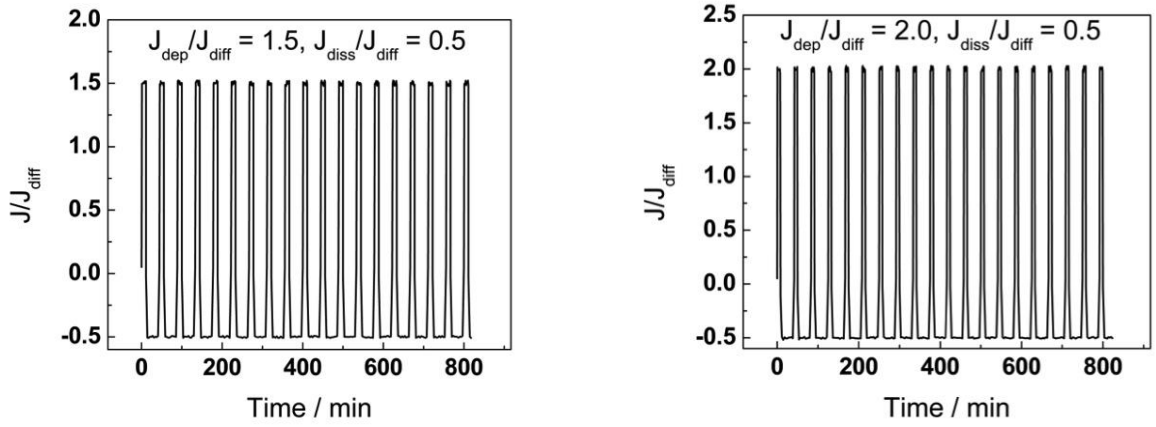

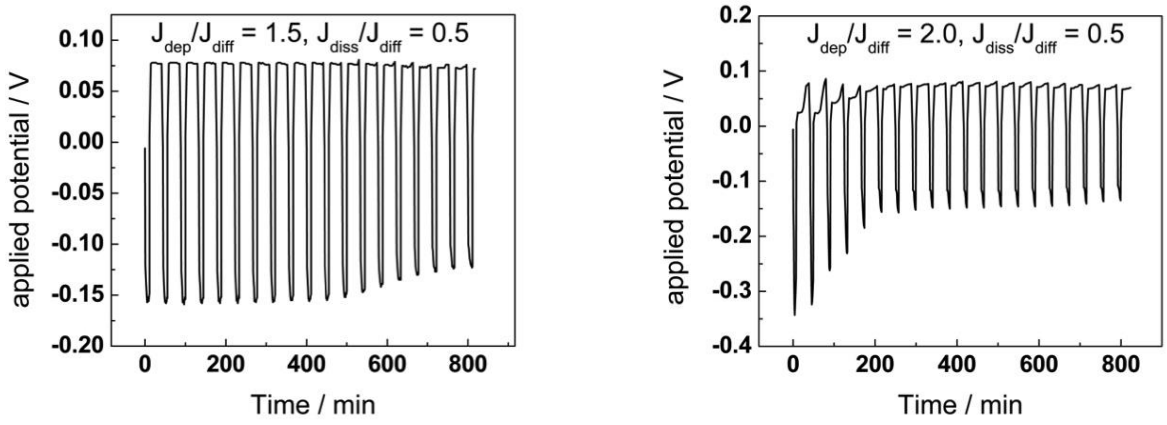

Fig. 4. 17 Applied potential and current density in the charge/discharge cycles.

Fig.4.18 shows the deposits morphologies in the systems for the 1st, 5th, 10th, and 15th cycles for different discharge current densities (J_{diss}/J_{diff} = 0.1, 0.5, 1.0 and 1.5) and different charge current densities (J_{dep}/J_{diff} = 1.5 and 2.0). It reflects that the surface of anode will become rougher and rougher during the charge/discharge cycles in all cases. Also, by comparing different discharge current density conditions we can observe that when charge current density is not high, the discharge speed will not influence anode morphology in a small number of charge/discharge cycles, even though the anode surface does get rougher and rougher. But when the charge current density is high, especially when the system becomes dendritic, the discharge speed will influence the anode morphology. Since dendrites may break off during discharge process, and the unlinked solid will be removed from the system in each cycle, the anode will become thinner and thinner during cycling.

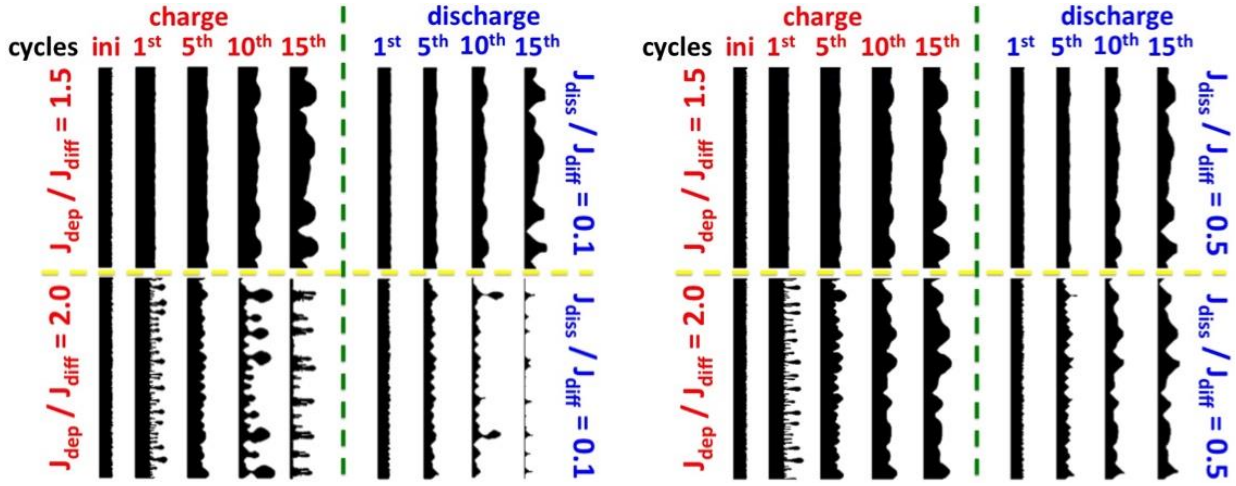

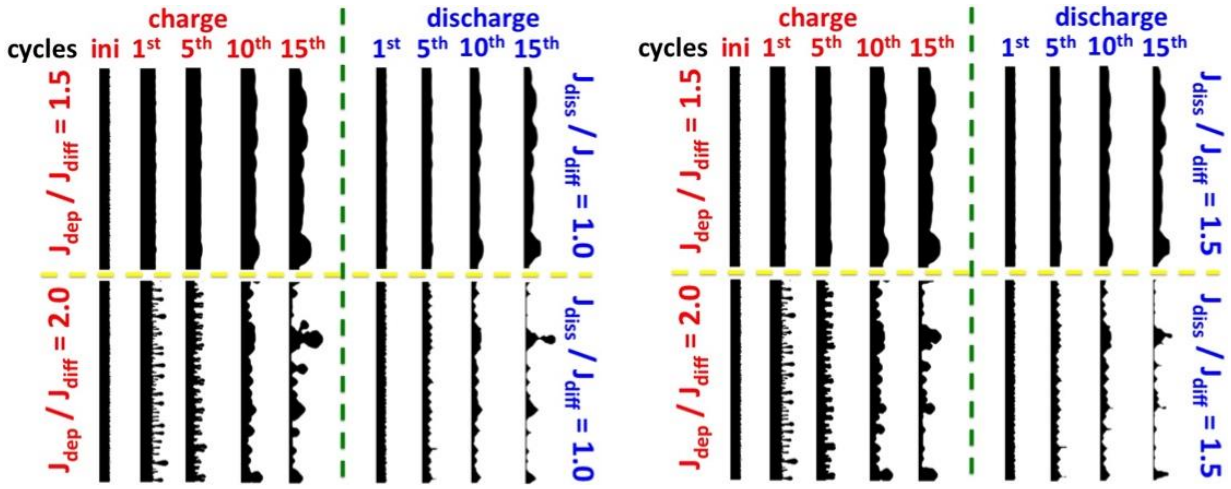

Fig. 4. 18 Morphologies of anode during charge/discharge processes under different charge and discharge current densities.

We can count the disconnected solid in each charge/discharge cycle and compare the influence of discharge current density (shown in Fig.4.19 left, charge current density is 2.0). The results show that as the cycle number increases, the number of breakaway nodes will decrease and increase alternatingly. This is because the breakaway of big dendrite will somehow help to smooth the anode surface, leading to smaller dendrite formation in the following cycles. But since the charge current density is high, the effects of dendrite formation in each cycle will accumulate to form larger dendrite again. Therefore, under high deposition current densities, the number of breakaway solid nodes will decrease and increase alternatingly as the cycle number increases. An interesting observation is that there seems to be an optimal discharge current density that minimizes the number of unlinked solid, which is 0.5 in this system. Under this discharge current density, dendrites will break off normally at initial cycles and then form a "stable" structure in which for the following cycles, even though the charge process will result in rougher surface, but no big dendrite forms (see Fig.4.18). Same tendency can be observed for the other charge current densities when there is break off of solid during discharge process (shown in Fig.4.19 right). We believe this optimal discharge current density may be resulted from the competition between higher local concentration and higher applied potential. As we mention before, higher concentration seems to suppress the break off due to concentration polarization. However, when discharge current is high, the overpotential will mainly be contributed by the applied potential, and the concentration polarization will have comparatively smaller effect.

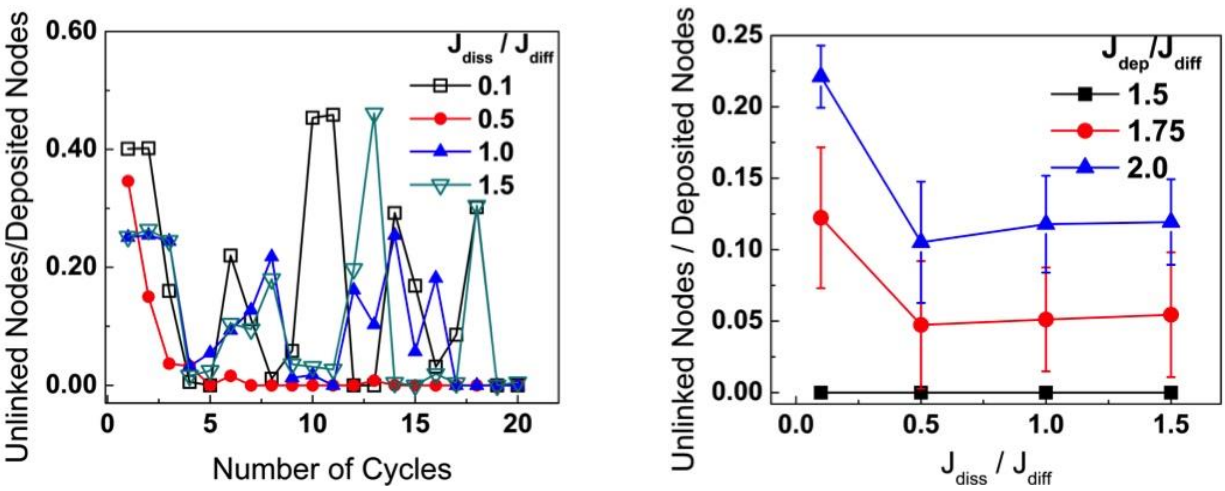

Fig. 4. 19 Total number of unlinked solid in (left) each charge/discharge cycle of the system with fixed charge current density of 2.0 and different discharge current densities (Normalized to the total amount of solid deposited on the anode in each cycle), and (right) 15 charge/discharge cycles for different charge and discharge current densities (Normalized to the total amount of solid deposited on the anode of the 15 cycles).

4.5 Conclusion

LBM can be a powerful simulation tool to simulate the electro-deposition and electro-dissolution process. Our model can capture all the experimentally observed features of microstructure evolution at the anode, from smooth to mossy to dendritic. Our results show that when inhomogeneous reactivity at the electrode-electrolyte interface (denoted by curvature constant ***K***) is not extremely high, there are two transition current densities in the deposition system. One is the crossover current density, which is governed by inhomogeneous surface reactivity (when diffusivity and mobility of charged particles are fixed) and denotes the transition from flat/rough structure to mossy/dendritic structure. The other is the critical current density that is governed by the relative speed of diffusion to electromigration, which denotes the transition from mossy structure to dendritic structure. While the system current density is larger than the crossover current density, the time when dendrite may form (sand's time) is more sensitive to electrode roughness than the inhomogeneous reactivity at interface, when both roughness and curvature constant are not too high. For comparatively high inhomogeneous reactivity system, there is larger current density regime for mossy structure formation; for low inhomogeneous reactivity system, the regime is small, and sometimes it may not be easy to observe the mossy structure and the system will turn into dendritic structure directly. When inhomogeneous reactivity is extremely high, dendrite may form at small current density condition, which is mainly governed by the highly inhomogeneous reactivity at electrode-electrolyte interface.

We also introduced a method to monitor the growth of morphologies in the system by tracing the change rate of surface area, which is very sensitive to dendritic structure. It can predict the dendritic system even before big dendrites form.

Our model is capable to simulate the charge/discharge cycles of a battery system. It seems that no matter how small the discharge current density is, the surface of anode will become rougher and rougher during cycles. It is inevitable to have Li metal break off during discharge process if the anode is already dendritic. However, there seems to be an optimal discharge current density, which lead to more "stable" anode morphology in the first several cycles and results in smaller amount of break-off dendrites. This

optimal discharge current density may be resulted from the competition between higher local concentration and higher applied potential in the system.

Chapter 5. 3D Simulation of Intercalation Reactions in Graphite Electrode of Li-ion Batteries by Using Lattice Boltzmann Method

5.1 Introduction

Carbon materials, such as graphite, are widely used in Li-ion batteries as the active component of the anode, and these systems are currently the foremost candidates to be used in electric vehicles (EVs)[167]. Even though lots of attempts have been made to improve the properties of anode materials[168-170], one of the key issues is to suppress the plating of Li metal, which can grow into dendritic structures that cause capacity loss and even trigger short circuits[99, 171, 172]. To fulfill this target, we have to be able to control the relation between operating parameters, such as current and voltage, the mass transfer properties of anode materials and the packing structure of anode in order to optimize the uniformity of the composite graphite electrodes as electrochemical reaction happens[170], or add active additives to suppress dendrite formation, mainly by adjusting solid electrolyte interphase (SEI) formation[173-176]. Even though SEI formed on the anode surface can suppress dendrite formation to a certain extent, it also leads to increase of cell resistance and capacity fade, which are not favorable for the battery system[176, 177]. In the meanwhile, in order to identify the design parameters to obtain optimal performance of the batteries, many numerical models have been developed, which can be of great help in order to understand the physical phenomena. In this chapter, we will introduce a LB model to simulate the intercalation reaction process in graphite electrode of Li-ion batteries. We will mainly focus on the influence of microscopic morphology of electrode and operation conditions on the intercalation reactions, especially on how to optimize them to suppress the plating of Li dendrites.

5.2 Background

Ever since the simulation work published by Doyle, Fuller and Newman[178], which established a generalized mean-field model for an idealized Li-ion battery system, lots of macroscopic models have been developed. Various effects were added to develop the original model to make it more physical, such as the influence of side reactions [179, 180], microscopic cell design[181, 182], and thermal effects[183]. However, all of these macroscopic models have to homogenize the microstructures of electrodes to some effective parameters, which make them insufficient to consider the detailed microscopic properties of the system. More recently, Smith, etc. developed a model that based on microstructures, which accounts for the mass transfer and interaction between particles in the porous electrodes explicitly[184]; Chirkov and its coworkers modeled equal-sized grain system and investigated the percolation properties of the anode active layer and the anode with nanosize particles[185]; and Harris, etc. simulated the non-shrinking-core behavior in a MCMB (meso carbon micro beads) graphite composite electrode by considering the polycrystalline nature and anisotropic diffusion of MCMB particles[186]. These mesoscopic models are either in 2D or use simplified particle morphologies, for example, square lattices or spheres. Even though some 3D models were developed to simulate the battery system[187-191], they either focused on individual particles in simple geometries, or simple system morphologies with identical particle distributions. 3D random morphologies are considered in some models[192], however, only in the homogenization step. Ideally speaking, we need a mesoscopic simulation method that can easily handle the mass transfer in the random porous system and local electrochemical reactions in a computationally efficient manner.

In this chapter, we introduce a mesoscopic numerical method, called the Lattice Boltzmann Method (LBM), to simulation the intercalation reactions in graphite electrode. Originated as a numerical method for Computational Fluid Dynamics (CFD) three decades ago[6, 88], LBM has been developed into a powerful tool to simulate complex mass transfer phenomena, such as advection-diffusion system[89, 90], electroosmosis flow[91-93], and electrochemical reactions[23, 24]. It is particularly easy to handle

complex boundary geometries[7], which has lots of applications in simulating mass transfer in porous structures[16, 193, 194]. And the intrinsic local operations of the LBM algorithm makes it very easy to be parallelized to simulate comparatively large system[8]. Therefore, LBM can be an ideal numerical method to model batteries.

By using LBM, we simulated a 3D half-cell system with random graphite as anode and pure Li metal as counter electrode. Both galvanostatic and potentiostatic conditions were discussed. We tested the relation between operating parameters (current and potential) and electrode parameters (porosity, thickness and diffusivity) on the initial plating time and the final total charge density when plating happens. Different equilibrium potentials forms (empirical fitting[195], fitting of SONY 18650 cell[196], and staged profiles[197]) were also compared. Finally, we tried to modify the random morphology of electrode with density gradient and obtained much better electrode performance, which can be helpful for the designing and manufacturing of better batteries.

5.3 Model Setup

5.3.1 Mass Transfer in Electrolyte and Electrode Materials

Without convection, the mass transfer in electrolyte can be expressed by Poisson-Nernst-Plank (PNP) equations:

$$\frac{\partial c_i}{\partial t} = D_i \nabla(\nabla c_i + \frac{z_i e c_i}{kT} \nabla \psi) \quad (5.3.1)$$

$$\nabla^2 \psi = -\frac{\rho_f}{\varepsilon \varepsilon_0} \quad (5.3.2)$$

where c_i is the concentration of species *i*; D_i is the diffusion coefficient of the species in electrolyte; z_i is the charge on species *i; e* is the charge of an electron; *k* is Boltzmann constant; *T* is temperature; and ψ is electrical potential; ρ_f is the net charge density; ε_0 is dielectric constant in vacuum and ε is relative dielectric constant. The electrical mobility in the electromigration part ($u_j = \frac{z_i e}{kT} D_j$) is calculated based on electrolyte conductivity σ, which is $\sigma_j = z_j e c_j \mu_j$, instead of the Einstein equation in the original PNP equations.

To solve the PNP equations in the framework of LBM, we can simply regard the electromigration part as the advection term in the conventional Lattice Boltzmann (LB) Equation for the advection-diffusion lattice[18]. In a single-relaxation-time LB model, the physical system can be divided into two steps: collide and stream, which are expressed in a single equation:

$$f_i(\boldsymbol{r} + \Delta t \boldsymbol{v}_i, t + \Delta t) = \left(1 - \frac{1}{\tau}\right) f_i + \frac{1}{\tau} f_i^{eq} \quad (5.3.3)$$

where f_i (**r**, t) is the local density distribution function in the *i* direction; τ is the relaxation time. The velocity $\mathbf{v}_i$ is chosen so that, in one time step Δt, a particle can reach one of its nearest neighbors. f_i^{eq} is the equilibrium density distribution function. With a regular BGK dynamics, it can be calculated based on the expression:

$$f_i^{eq} = t_i \rho \left(1 + \frac{1}{c_s^2} \mathbf{v}_i \cdot \mathbf{u}\right) \quad (5.3.4)$$

The local drift velocity **u** can be obtained from the electromigration term.

The microscopic potential distribution in the system defined in equ.5.3.2 can be solved by using traditional Successive Over-Relaxation (SOR) method[94].

The mass transfer inside of graphite electrode can be simplified as a diffusion process. The same solver for the PNP system can be used by setting the local drift velocity **u** = **0** (no electrical field is considered inside the anode material).

5.3.2 Electrochemical Reactions at Electrode-Electrolyte Interface

The electrochemical reaction at the electrode-electrolyte interface is defined by the following Butler-Volmer expression:

$$i = i_0(e^{\alpha_1 F\eta/RT} - e^{-\alpha_2 F\eta/RT}) \quad (5.3.5)$$

where F is faradic constant, R is gas constant and T is temperature. η is overpotential, which is defined as $\eta = V_{app} - U$, where V_{app} is the applied potential on the anode, and U is the open-circuit potential (OCP) of the graphite electrode. α_1 and α_2 are symmetry factors related to the potential barrier for the intercalation reaction. in this system, we use $\alpha_1 = \alpha_2$ = 0.5. i_0 represents local exchange current density. When concentration polarization is considered, the local exchange current density can be calculated based on[180]:

$$i_0 = i_0^{eq}(c_t - c_s)^{\alpha_1}(c_s)^{\alpha_2}(c)^{\alpha_1} \quad (5.3.6)$$

where i_0^{eq} is the exchange current density at open-circuit condition. c_t is the maximum concentration in intercalation material. c_s is the concentration of lithium in solid phase. c is the concentration of lithium in liquid phase at the interface. In every time step, the concentration of interface nodes at the electrolyte lattice for Li ions will be decreased by the amount that is calculated based on the equ.5.3.6 locally, and the concentration of the interface nodes at the solid lattice for Li atom will increase the corresponding amount.

The OCP is a function of intercalation stage of the system, and it can be obtained both experimentally or theoretically. In this paper, we used three different open-circuit potential formulas obtained from papers: empirical fitting[195], fitting of SONY 18650 cell[196], and staged profiles[197]. We will call them OCP1, OCP2 and OCP3 correspondingly. OCP1 used the Redlich-Kister expansion to fit for the OCP of MCMB in experiment. OCP2 fits for SONY 18650 cell and is widely used in many simulations. OCP3 used piecewise function to represents different stages of intercalation in experiment. Fig.5.1 shows the OCPs as a function of intercalation stage.

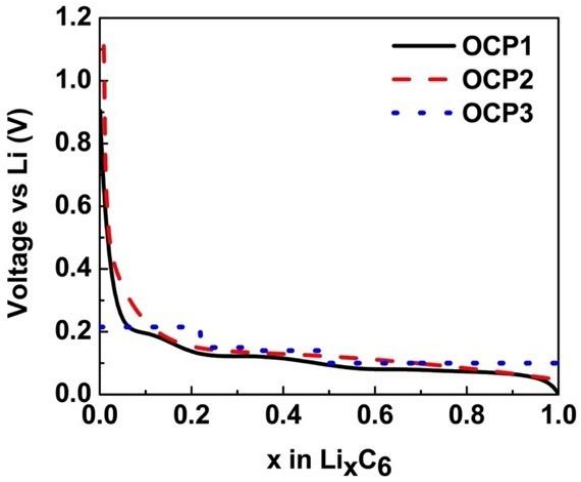

Fig. 5. 1 Open-circuit potential (OCP) of the graphite electrode for empirical fitting (OCP1), fitting of SONY 18650 cell (OCP2), and staged profiles (OCP3).

When the interface overpotential drops to a certain value, plating may happen. The overpotential for plating, η_p, can be calculated based on Nernst equation:

$$\eta_p = V_{app} - E_p^{eq} - \frac{RT}{zF} ln(c) \qquad (5.3.7)$$

where E_p^{eq} is the equilibrium potential for plating at open-circuit condition. When $\eta_p < 0$, plating will happen at the local position. Our simulation will stop at the same time.

5.3.3 Boundary Conditions

In this 3D model, two parallel electrodes were used. One is the working electrode, graphite, with random morphologies. The other is an "imaginary" counter electrode of pure Li metal. We did not calculate the reactions at the "imaginary" counter electrode explicitly. Instead, a uniform inlet current was applied, which is averaged based on the total current at the graphite electrode. Periodic boundaries were used in the other two directions that are perpendicular to the electrodes plane. For electrolyte lattices, which are used to calculate the mass transfer in electrolyte, bounce back boundary condition was applied at electrode nodes. For solid lattice, which is used to calculate the mass transfer in electrode materials, bounce back boundary condition was applied at the solid boundaries, and no dynamics were assigned to the electrolyte nodes. The bounce back nodes in the solid lattice have regular BGK dynamics but the distribution functions point to the electrolyte directions will bounce back in each time step. In order to handle the intercalation step at the electrode-electrolyte interface, one layer of overlap nodes is used at the interface (shown in Fig.5.2). The lattice dynamics were assigned for different lattices based on Table.1. Here, a partition coefficient of 1.0 is used to assume that all the reduced Li atoms will intercalate into graphite electrode, if the local overpotential $\eta_p \geq 0$. Note that we did not consider the formation of SEI in this model, which plays an important role in the capacity fading of the battery. However, the effects of SEI (consumption of electrolytes and increasing resistance at the interface) can be added at the interface nodes easily in a modular manner, which will be included in our future work.

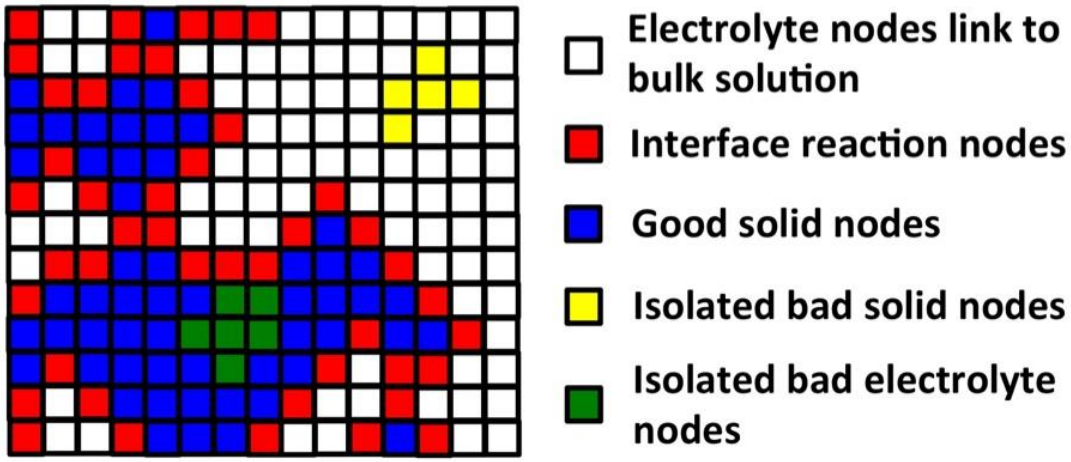

Fig. 5. 2 An illustration of phase distribution of the system.

Table. 5. 1 Dynamics for different phases in different lattices

	Solid Lattice	Electrolyte Lattices
BGK Dynamics		
Bounce Back Dynamics		
No Dynamics		

5.3.4 System Morphologies

In this paper, we used $256 \times 128 \times 128$ D3Q7 lattices to represent a cell with the size of 256 μm by 128 μm by 128 μm, in which the graphite anode is 32 μm thick in x direction, unless otherwise specified. Periodic boundary conditions are applied in the y and z directions. The anode morphologies are generated randomly with the solid volume fractions from 50% to 80% (shown in Fig.5.3). In each of the morphologies, we checked the percolation of the solid nodes to guarantee the volume fraction of isolated "bad" solid nodes is within 0.5%. We should note that there are ways to generate morphologies more exactly from real electrode morphologies in experiment[198], which would be very helpful to increase the accuracy of the model. In order to eliminate the error from a certain random morphology, we averaged 5 different random samples for a certain volume fraction in the system for the data in this chapter.

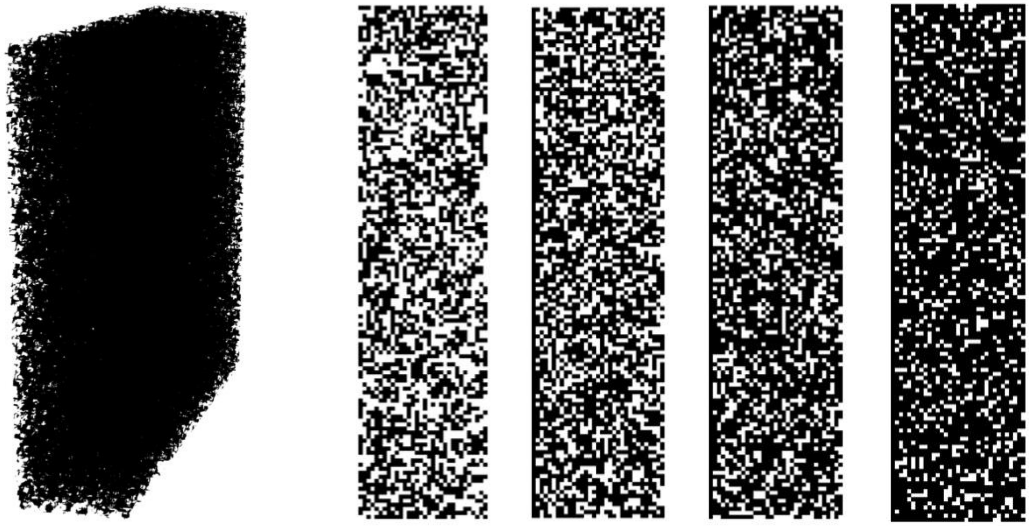

Fig. 5. 3 Morphologies of graphite electrodes. (left) 3D morphology for 50% density electrode. (right) 2D slices of graphite morphologies in the x-z plane of the middle of y-axis (from left to right, electrode densities are 50%, 60%, 70%, and 80%).

Fig.5.4 shows the averaged number of interface nodes at different electrode densities. It reflects the interface area in the system. The result shows that as the electrode density increases, the interface area decreases. As the electrode density increase from 60% to 70%, there is a sharp drop of interface area of the system. This sharp drop will result in some property change of the system, as we shall show in the results section.

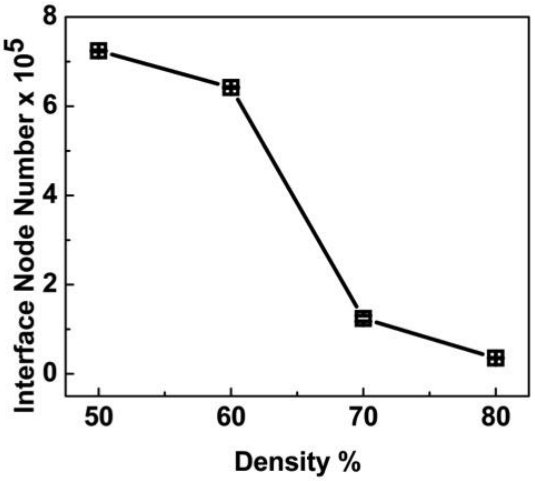

Fig. 5. 4 Averaged number of interface nodes at different electrode densities.

5.3.5 System Parameters

The equilibrium exchange current density $i_0^{eq} = 0.21$ mA/cm^2 [180]. The mobility of the Li and the PF_6 ions were both fixed at 1.0e-3 mm^2/(s V), which represents the electrolyte (1M) conductivity of about 2 mS/cm. Note that the conductivity from other papers for $LiPF_6$ (1M) is around 6 to 10 mS/cm[160-162]. Considering the local ion concentration in the cell may drop to very low values, we used a slightly smaller value, but it is still in the same magnitude. The temperature T was kept constant at

298K and the dielectric constant of the electrolyte was fixed at 46.44. We used diffusion constants for the Li and PF_6^- ions in electrolyte equal to 2.0e-4 mm^2/s and 1.0e-4 mm^2/s respectively. The diffusion coefficient of Li atoms D_s in graphite can vary from 1.0e-5 to 1.0e-8 mm^2/s[199, 200]. The bulk concentration of Li ion was initialized at 1.0M. Unless specified, most of the paper will focus on galvanostatic conditions. In galvanostatic condition, the applied potential on the graphite electrode will be adjusted in every time step to maintain the constant current density, and the potential of the counter electrode is kept constant as 0 V. Potentials in the system are referred to the equilibrium potential of $Li|Li^+$(1M) reference electrode at 298K and 1 atm. The maximum concentration of Li atom in graphite $c_t = 30.54$ mol/L, and the density of graphite is 2.20 g/cm^3 [180], and the charge density (mass density) of graphite can be calculated to be 372 mAh/g when the electrode is fully intercalated.

5.4 Results and Discussion

5.4.1 Influence of Electrode Density

Fig.5.5 shows the final charge density of the system before plating or until the electrode is fully intercalated, whichever comes first. It indicates that smaller electrode density will always lead to higher charge density, when the rest of the parameters are the same. Larger current or smaller diffusivity of Li atom in electrode will give smaller charge density when electrode density is high. An interesting observation is the drop of charge density mainly begins when the electrode density increases from 60% to 70%. This is exactly the same point at which we see a sharp surface area change in the system. When electrode density increases, the mass density increases, and thus the actual current in a fixed volume will increase (shown in Fig.5.6). And at the same time, the surface area decreases sharply. These will result in a large increase of current density at the electrode-electrolyte interface. And when the diffusion of Li atom into the electrode material is not fast enough, the interface graphite will soon become fully intercalated and thus result in plating. This leads to very large inhomogeneous distribution of Li intercalation in the electrode (shown in Fig.5.7).

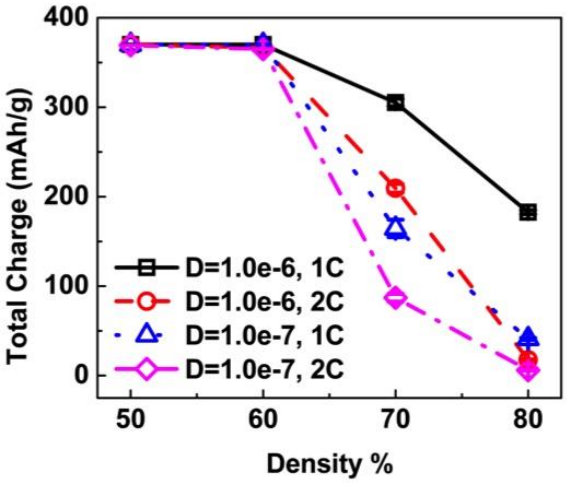

Fig. 5. 5 Final charge density of electrodes with different densities under galvanostatic conditions.

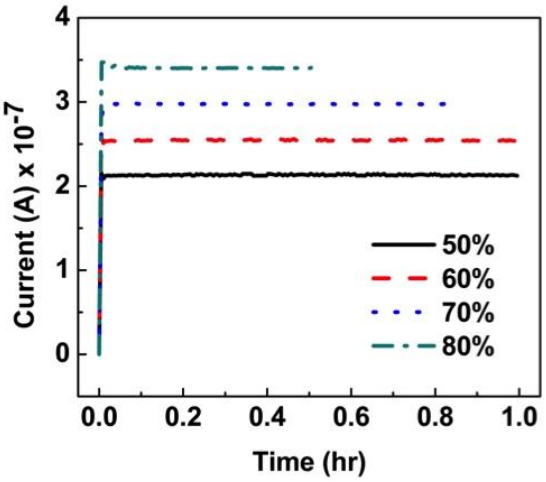

Fig. 5. 6 Current of the system with different electrode densities under galvanostatic conditions.

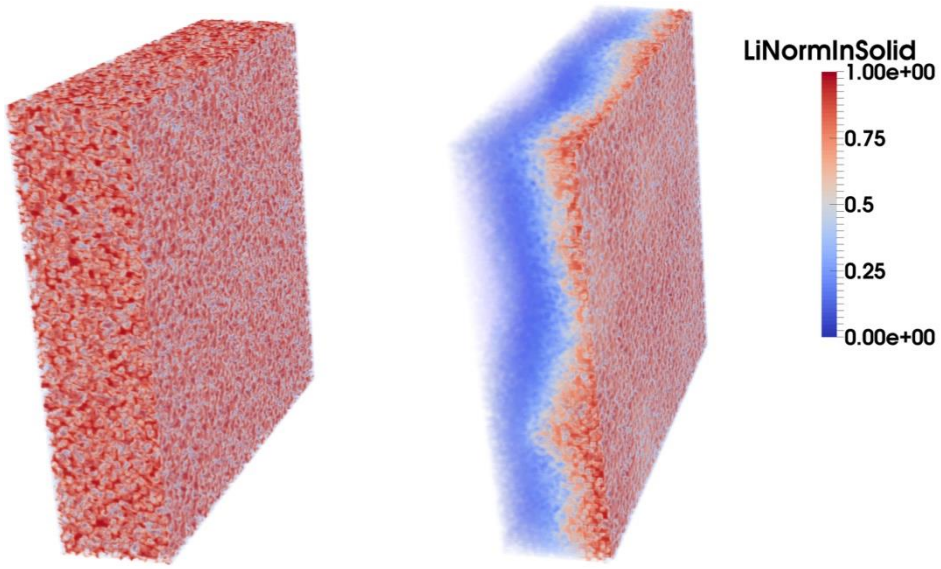

Fig. 5. 7 Normalized Li atom density in the working electrodes under galvanostatic conditions. (left) 60%, 1C, and D_s = 1.0e-7 mm^2/s. (right) 70%, 1C, and D_s = 1.0e-7 mm^2/s.

Fig.5.8 shows the phase diagram of transition points of the system when plating happens before electrode is fully intercalated. In these plots we adopt the convention of the C rate as a measure of the charging rate. 1C rate means the battery can be fully charged in 1h. It shows that electrode with smaller densities (50% and 60%) can tolerate higher current (3C and 2C correspondingly) without any plating. In addition, when the electrode density is comparatively high (60 % to 80%), plating is not very sensitive to the diffusivity of Li atom in electrode. However, if the electrode density is low (50%), plating can be sensitive to the diffusivity (the transition happens at the region of D_s = 1.0e-6 to 1.0e-7 mm^2/s).

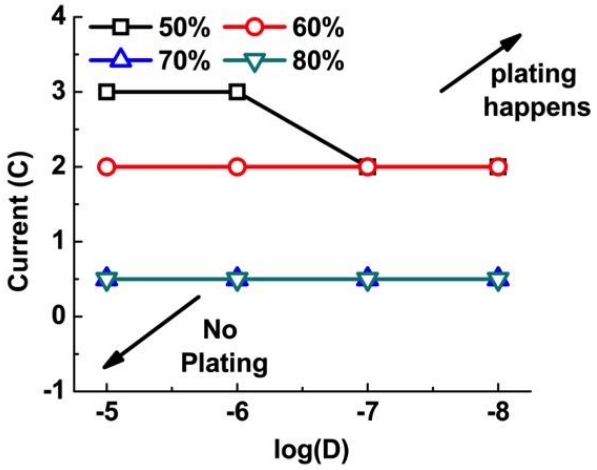

Fig. 5. 8 Phase diagram of transition points of the system when plating happens before electrode is fully intercalated under galvanostatic conditions.

5.4.2 Influence of Li Atom Diffusivity in Graphite

Fig.5.9 shows the final charge density of the system as a function of Li atom diffusivity in graphite under galvanostatic conditions. It indicates that when electrode density is not high (60%), the final charge density is not sensitive to the Li atom diffusivity in graphite. While electrode density is comparatively high (70%), higher diffusivity will lead to higher final charge density. There seems to be an apparent drop of charge density when the diffusion coefficient drops from 1.0e-6 to 1.0e-7 mm^2/s. This transition might be governed by the relative speed of graphite diffusivity and interface reactivity.

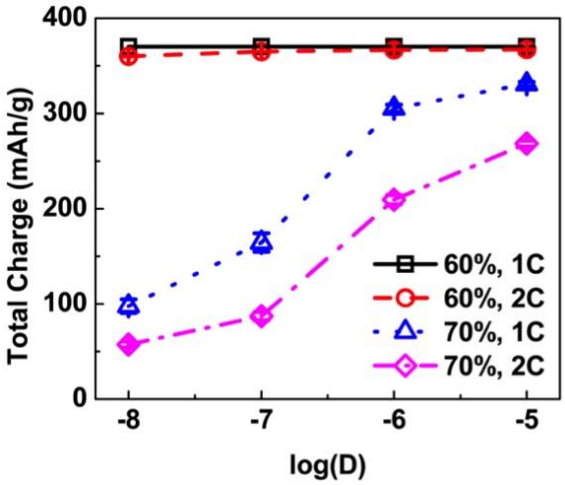

Fig. 5. 9 Final charge density as a function of Li atom diffusivity in graphite under galvanostatic conditions.

Fig.5.10 shows the phase diagram of transition points for plating of the system at different diffusion coefficients of graphite electrode. The result shows that the transition curve of plating is not sensitive to the diffusivity in graphite when electrode density is comparatively high (above 60%). But when electrode density is low (50%), higher diffusivity (above 1.0e-6 mm^2/s) systems can tolerant larger C-rate current (3C).

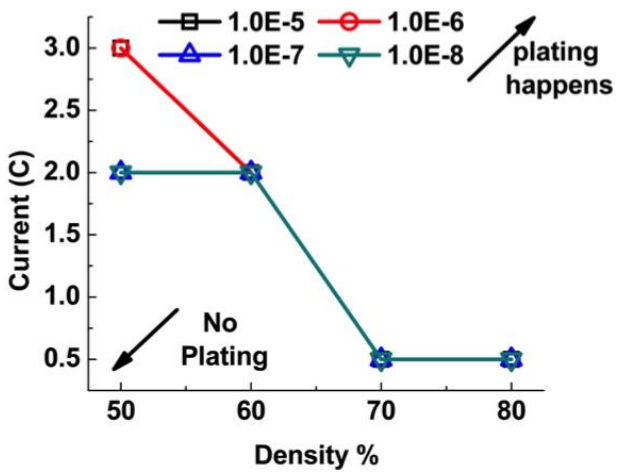

Fig. 5. 10 Phase diagram of transition points of the system at different diffusion coefficients of graphite electrode under galvanostatic conditions.

5.4.3 Influence of Current

Fig.5.11 shows the final charge density of the system as a function of C-rate current under galvanostatic conditions. The result shows that when electrode density is small (60%) the final charge density is not very sensitive to the applied current, if the diffusivity of graphite does not change too much. When electrode density is high (70%), larger current will lead to smaller amount of charge density. We can expect that apparent decrease of charge density could be observed in small electrode density system (below 60%) when the current becomes much larger.

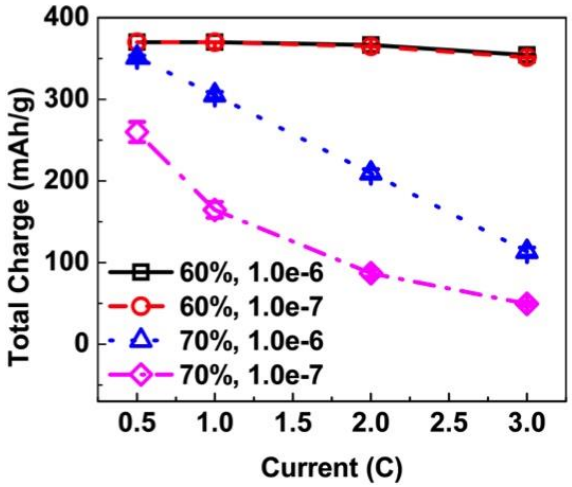

Fig. 5. 11 Final charge density as a function of C-rate current under galvanostatic conditions.

Fig.5.12 shows the phase diagram of transition points for plating of the system at different C-rate currents under galvanostatic conditions. It indicates that when current is small (below 1.0C), plating will happen only when electrode density is comparatively large (above 70%). When current increases, we may need to decrease the electrode density to suppress plating. The diffusivity of graphite plays a limited role, except that when the C-rate current is intermediate (2.0C).

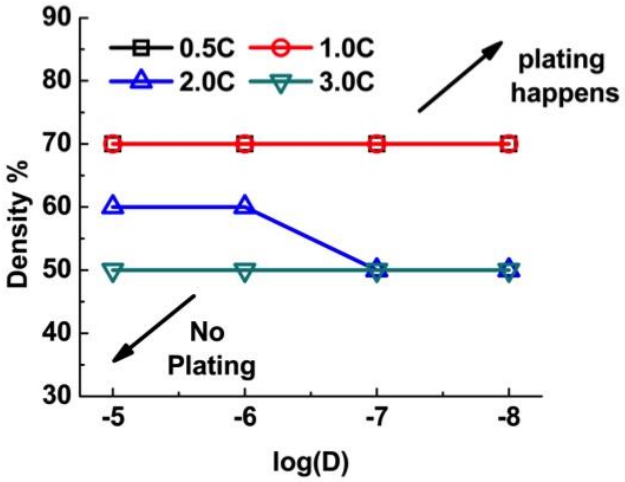

Fig. 5. 12 Phase diagram of transition points for plating of the system at different C-rate currents under galvanostatic conditions.

5.4.4 Influence of Electrode Thickness

To test the influence of electrode thickness, we compared the system with 3 different thicknesses: 16, 32, and 64 μm. In all cases, the thickness of electrolyte domain is kept constant. Fig.5.13 shows the final charge density of the system at different electrode thicknesses with constant current of 1C and D_s = 1.0e-6 mm^2/s. The result indicates that when electrode density is small (60%), the charge density is not very sensitive to the thickness of electrode. But when the electrode density is large (70%), the electrode thickness will have tremendous influence on the final charge density. The final charge density will decrease with the increase of electrode thickness when electrode density is large. This is mainly because it is harder for electrolyte to penetrate into the inner part of the electrode with higher densities, which may lead to the inhomogeneous distribution of Li atoms in the electrode material, and the longer diffusion length in the thicker electrode. Also, the thicker electrode requires larger current density in the C-rate current system, which would lead to large reaction speed, thus large accumulation of Li atoms at the electrode-electrolyte interface.

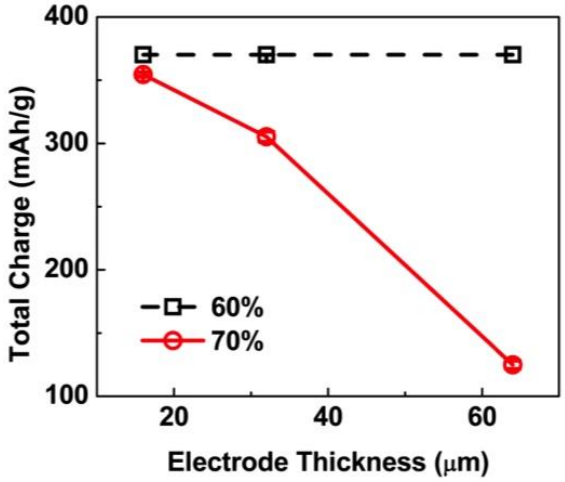

Fig. 5. 13 Final charge density at different electrode thicknesses with constant current of 1C and D_s = 1.0e-6 mm^2/s.

Fig.5.14 shows the normalized Li atom density in the working electrodes at different electrode thicknesses when electrode density is 70%. It shows that the thicker the electrode is, the more inhomogeneous the Li atom distribution will be.

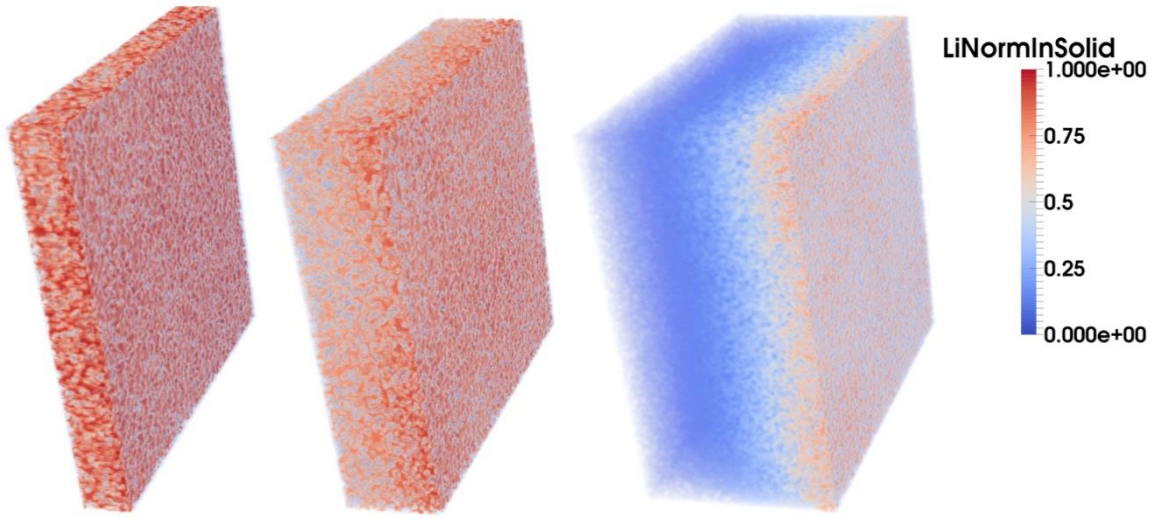

Fig. 5. 14 Normalized Li atom density in the working electrodes at different electrode thicknesses with electrode density of 70%, current of 1C and D_s = 1.0e-6 mm^2/s. From left to right, the electrode thicknesses are 16, 32 and 64 μm.

5.4.5 Influence of Equilibrium Potential Formula

In the previous sections, the OCP of the system is defined by the fitting curve of experiment result form SONY 18650 cells (OCP2). In this section, we are going to check the influence of OCP in the system by comparing 3 different OCP formulas defined in section 5.3.2 (OCP1, OCP2, and OCP3).

Fig.5.15 shows the applied potential change in the system with different OCPs under galvanostatic conditions with current of 1C, electrode density of 60% and D_s = 1.0e-6 mm^2/s. This figure has the similar tendencies as the OPC curves in Fig.1, which means the applied potential is highly positively related to its OCP formula.

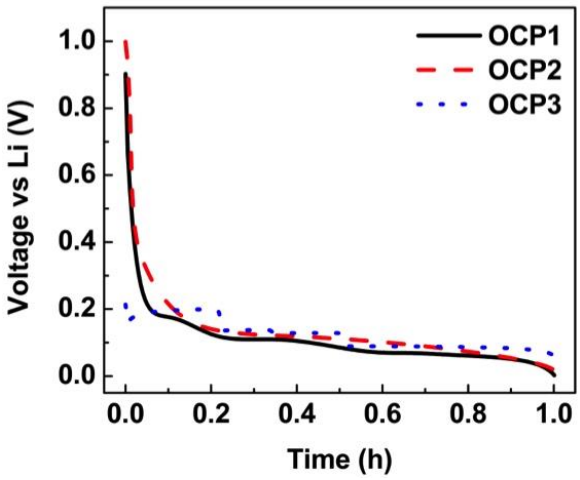

Fig. 5. 15 Applied potential in the system with different OCPs under galvanostatic conditions with current of 1C, electrode density of 60% and D_s = 1.0e-6 mm^2/s.

Fig.5.16 shows the final charge density for the three different OCP systems under different electrode density conditions (60% and 70%). The results indicate that when both electrode density and current are small (60% and 1C), system charge density will not be influence by the form of OCP. When the electrode density is large (70%) or when the current is large (2C), the final charge density in the system tend to have the tendency: OCP3 > OCP2 > OCP1. Which may result from the comparatively larger equilibrium potential in OCP3 when the intercalation amount tends to be high. This will lead to higher applied potential and from Eq.5.3.7 we know that plating will be harder in this system.

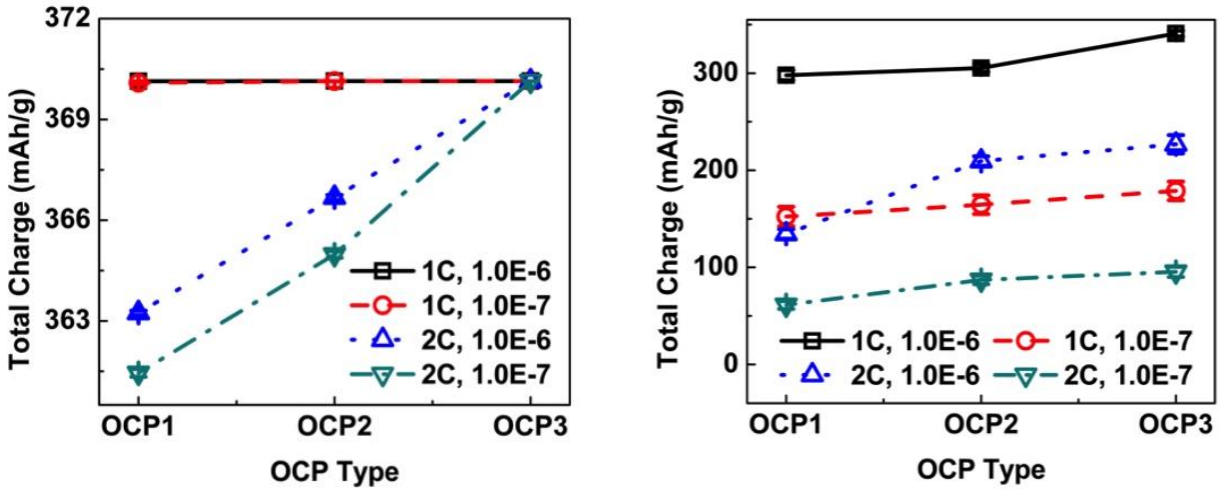

Fig. 5. 16 Final charge density for different OCPs. (left): electrode density is 60%; (right): electrode density is 70%.

5.4.6 Modified Electrode Morphologies

The fast developing 3D printing technology may make it possible to manufacture batteries with targeted microstructure in the future. As is shown previously, the microstructure of electrode materials can have large impact on the properties of the system. Therefore, there is possibility to improve the performance of battery by modifying the morphologies of electrode materials.

Fig.5.17 shows the cross section of a modified morphology, which has larger densities at the base of the electrode and smaller densities near the electrolyte domain. Fig.18 compares the final charge densities of the modified electrode to the pure random electrode systems. The result indicates that by adjusting the packing distribution of electrode materials, it is possible to increase the performance of battery tremendously for a fixed volume fraction of electrode. The modification here at one hand increases the surface area to decrease the current density, and at the other hand, makes it easier for electrolyte to penetrate into the inner part of the electrode. Even though the density near the base of the electrode is high, the thickness is very small. From the observations in section 5.4.4, it is known that the very thin electrode materials will not decrease the charge amount a lot. Therefore, we could obtain higher total charge by modifying the distribution of electrode materials with a gradient (high near the current collector and small near the electrolyte domain) of the electrode density.

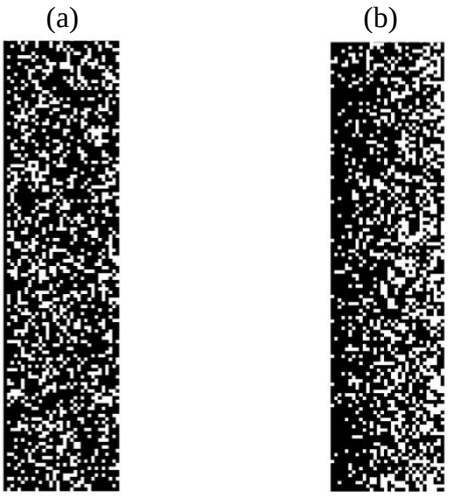

Fig. 5. 17 2D cross section snapshot of the electrode morphologies: (a) pure random, and (b) modified

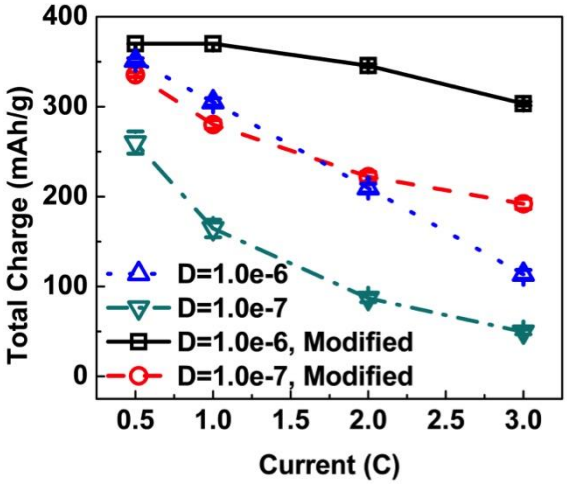

Fig. 5. 18 Comparison of final charge densities of the modified electrode to the pure random electrode systems.

5.4.7 Potentiostatic Test

In potentiostatic test, the applied potential is fixed at a certain value. As the intercalation reaction goes on, the local OCP will drop until the system reaches equilibrium, at which the applied potential should be very close to the OCP value of the intercalated material.

Fig.5.19 shows the typical curve of the current in the potentiostatic condition. It shows a sharp decrease of current at the initial stage of the intercalation reaction, and then the current decreases asymptotically to zero. The sharp initial drop of the current is mainly due to the drop of local OCP at the electrode-electrolyte interface. As is shown in Fig.5.1, the curve of OCP2 that is applied in the system will drop sharply at the initial stage of intercalation, therefore decrease the overpotential for the interface reaction, leading to a sharp decrease of current initially. In this stage, there is a sharp accumulation of Li atoms at the interface. With the decrease of the current, the accumulation will slow down, while at the same time, the Li atom will diffuse into the inner part of the electrode. The interfacial reaction and the diffusion of Li atom will be balanced, resulting in the following asymptotical decrease of current to zero, when the OCP of the electrode material reaches the value of OCP2 in Fig.5.1.

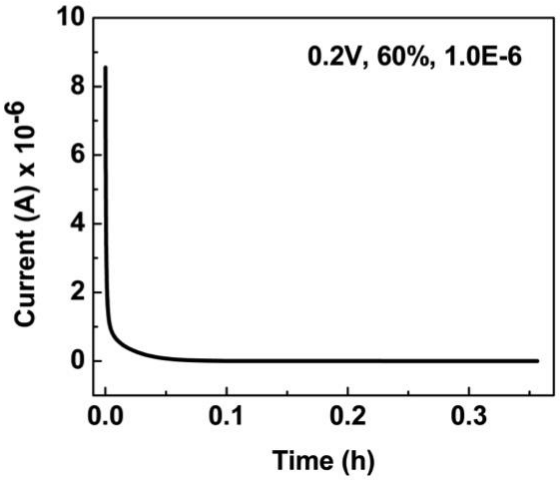

Fig. 5. 19 Current in the potentiostatic condition with applied potential of 0.2V, electrode density of 60% and D_s = 1.0e-6 mm^2/s

Fig.5.20 shows the final charge densities of the potentiostatic system when different potentials (0.1, 0.2 and 0.5 V) are applied. It reflects that the higher applied potential is, the lower the final charge density will be. This is because the amount of reaction is bounded by the applied potential in the system. When the intercalation reaches the equilibrium amount, applied potential equals the equilibrium potential, and no reaction could happen. An interesting observation is that the final charge density is almost identical for the same applied potential, no matter whether the electrode density or the Li atom diffusivity in graphite changes or not. This is because in the region of the asymptotical decrease of current, the distribution of Li atom will be homogenized. This homogenization state is only governed by the OCP value at equilibrium. Different diffusivities of Li atom will only alter the speed to reach the equilibrium, but they cannot change the equilibrium state itself. Therefore, if the intercalation reaction can carry on for enough time, the final charge density will be only governed by applied potential.

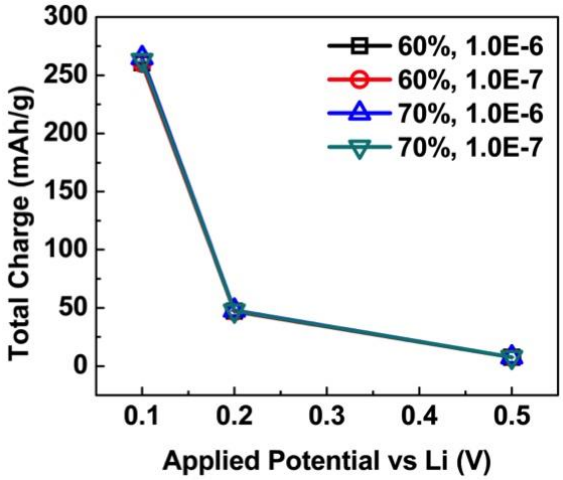

Fig. 5. 20 Final charge densities of the potentiostatic system.

5.5 Conclusion

By using LBM, we simulated a 3D half-cell system with random morphologies of graphite as anode and pure Li metal as counter electrode. We tested the relation between operating parameters (current and potential) and electrode parameters (porosity, thickness and diffusivity) on the final total charge density when plating happens. It is shown that our model can track most of the key features of the intercalation system.

In galvanostatic condition, our model shows that smaller electrode density, smaller C-rate current and larger diffusivity of Li atom in graphite can help to obtain higher final charge density before plating happens. There is a sharp change of the property of the electrode when the electrode density change from 60% to 70%, which is mainly due to the sharp change in the interfacial area in the system. The applied current and the diffusivity of Li atom will have apparent influence on the final charge density when the electrode density is comparatively high. Thicker electrode tends to have smaller charge density when electrode density is high. The different forms of OCP will have larger influence on the system when the electrode density is high as well. By modifying the random morphology of electrode with density gradient, it is possible to obtain much better electrode performance. This model may help to design battery microstructures for optimal performance, which can be the input for new manufacturing methods, such as 3D printing.

In potentiostatic condition, the final charge density will be only governed by applied potential, which will be equal to the OCP value when the current of the system drop asymptotically to zero.

In the future, it is possible to simulate the full cell system and add the side reactions, the influence of SEI layer and the heat convections into the system in a modular manner straightforwardly.

Chapter 6. Simulation of Transdermal Drug Delivery by Using Lattice Boltzmann Method

6.1 Introduction

Ever since 1979 when the first transdermal patch was introduced in the United States, the number of new transdermal delivery systems is gradually increasing. Especially in more recent years (2003 to 2007), new systems were introduced at a remarkable pace; one every 7.5 months[201], and transdermal delivery has been transformed from an interesting new idea to a multi-billion US dollar per year industry[202]. The transdermal drug delivery has several advantages, such as the avoidance of pain, possible infection and compliance issues related to injections; the possibility to control drug release over long periods; and avoiding the first-pass metabolism via the oral route that can lead to large loss of drug[203]. The increasing demands for the transdermal patches, on the one hand, call for clinical research to develop more effective way of drug delivery through the stratum corneum (SC), which is the main barrier for skin permeability, and on the other hand, require more efficient drug design methods that can guide the drug development to obtain the transdermal patches with targeted delivery properties. During the past 30 years, many delivery enhancement methods were introduced, such as using chemical enhancers, noncavitational ultrasound and iontophoresis (second-generation delivery systems), and using microneedles, thermal ablation, microdermabrasion, electroporation and cavitational ultrasound (third-generation delivery systems)[201, 204-216]. Numerical tools can be of great help for us to understand the physical phenomena and identify the design parameters to reduce the cost and time for new drug development. In this chapter, we will introduce a LB model to simulate the transdermal drug delivery system, which can handle the "brick and mortar" structure of the SC layer explicitly and add the influence of enhancer straightforwardly. The influence of the key properties of the system, such as drug diffusivity, concentration, partition coefficients, will be tested and compared for more effective drug design.

6.2 Background

The numerical simulation models of transdermal drug delivery mainly focus on two levels: the molecular level and the patch-SC level. At the molecular level, Molecular Dynamics (MD) has been widely used to identify the partition coefficient and the diffusion properties of solute under different transdermal conditions[217-221]. In the patch-SC level, mass transfer of drug is usually regarded as a diffusion process, and Fick's Laws are applied. This mass transfer can be simplified as steady state Fick's first law, or described fully by Fick' second law[222, 223]. The structure of SC layer is either ignored[222, 223], or by homogenization of the "bricks and mortar" structures [224-228]. Passive diffusion [225, 229] (drug can diffuse through the corneocytes), nonlinear diffusion[230], and the effects of enhancer[221] have been investigated. However, in order to obtain more quantitively accurate simulation data for the guidance of drug design, there are several questions we need to answer: 1. Does the simplified steady state fick's law works for the drug delivery system that actually has finite size of patch and inhomogenous stratum corneum structure? 2. Is the homogenization of the stratum corneum structures an adequate way to capture the transport property in the actual inhomogenous structure?

The mostly widely used mathematical approaches to the Fick's mass transfer in transdermal delivery system are Laplace Transform Method (LTM)[231, 232], Finite Difference Method (FDM)[225, 229], Finite Element Method (FEM)[221, 224, 230], and Random Walk Method (RWM)[233]. The former three methods are numerical tools to solve differential equations in a top-down manner, which is not easy to implement complex local interactions and boundary conditions. On the contrary, the RWM is carried out in a bottom-up manner, which traces the random thermal motion of molecules in the system, and the mass transfer properties, such as the flux or density distributions, can be calculated by averaging the trajectories of the particles. But for large systems, this method is computationally expensive, and to

eliminate too much noise from the results, a lot of random trails need to be carried out. Here we try to introduce another bottom-up numerical method, called Lattice Boltzmann Method (LBM), to simulate the mass transfer in transdermal delivery system.

LBM was introduced three decades ago as a mesoscopic simulation method for Computational Fluid Dynamics (CFD)[6, 88]. Then it is soon developed to simulate advection-diffusion mass transfer systems[90]. A lot of complex advection-diffusion based physical systems have been studied, including electroosmotic flow in microchannels[19, 234, 235], dendrite formation from melt[21] and in convective solutions[153, 236], reacting flows[237, 238], and anisotropic diffusion[89, 239]. It is proved to be particularly successful in fluid flow applications involving interfacial dynamics and complex boundaries[7]. Therefore, LBM is an ideal numerical method for the simulation of transdermal drug delivery system.

In this chapter, by using LBM, we will compare the transdermal drug delivery models in the "brick and mortar" structures, and in the homogenized anisotropic system. By using "brick and mortar" structure, we tested the influences of different parameters, such as the drug amount in patch, patch thickness, partition coefficient at patch/SC interface, and the diffusion coefficient of drug in each component. Also, we will show that the influence of enhancer can be included in the model in a straightforward way.

6.3 Model Setup

6.3.1 Lattice Boltzmann Model

LBM is a particle-based model to simulate the evolution of physical systems. The evolution of a system is expressed by discrete Boltzmann Equation (BE), and if we use a simple single-relaxation-time BGK (Bhatnagar–Gross–Krook) dynamics[90] for the collision operation, the physical system can be expressed as:

$$f_i(\boldsymbol{r} + \Delta t\boldsymbol{v}_i, t + \Delta t) = \left(1 - \frac{1}{\tau}\right) f_i + \frac{1}{\tau} f_i^{eq} \qquad (6.3.1)$$

where f_i (**r**, t) is the local density distribution function in the i direction; τ is the relaxation time. The velocity $\mathbf{v}_i$ is chosen so that, in one time step Δt, a particle can reach one of its nearest neighbors. f_i^{eq} is the Equilibrium Distribution Function (EDF).

One of the key problems in LBM is to construct a suitable EDF to represent a targeted physical system. In this chapter, we will mainly consider three situations: pure diffusion, anisotropic diffusion in different directions and diffusion with enhancer.

The EDF for pure diffusion system can be easily derived from Maxwell distribution and conservation of mass[240]. It is:

$$f_i^{eq} = t_i \rho \qquad (6.3.2)$$

where t_i is the weight factor in the i direction, which is a constant for a chosen lattice structure, and ρ is the local density of solute. The relaxation time τ is a function of diffusion coefficient:

$$D = c_s^2 \left(\tau - \frac{1}{2}\right) \qquad (6.3.3)$$

where c_s is the speed of sound in the lattice, which reflects an effective propagation velocity of the lattice. By using Chapman-Enskog Expansion, it is easy to prove that this EDF and relaxation time can recover the pure diffusion equation[240]:

$$\frac{\partial \rho}{\partial t} = \nabla(D\nabla\rho) \quad (6.3.4)$$

Based on the pure diffusion EDF, it is easy to develop the collision step of the anisotropic diffusion with different diffusion coefficients at different directions. Note that in LBM, the diffusion coefficient is related to the local relaxation time. Therefore, for this anisotropic system, the relaxation time is also directional dependent[240]:

$$D_i = c_s^2\left(\tau_i - \frac{1}{2}\right) \quad (6.3.5)$$

where "i" denotes the direction in space. The EDF can be kept the same as pure diffusion. Then, we can obtain the new distribution function in each streaming directions based on Eq. (1), and the distribution function at the lattice center can be calculated from the conservation of mass.

For particles diffusion with enhancer, the Fick's second law can be expressed as:

$$\frac{\partial \rho}{\partial t} = \nabla(D(c_{en})\nabla\rho) \quad (6.3.6)$$

where $D(c_{en})$ is the anisotropic diffusion coefficient of the solute due to the local concentration of enhancer. Equ.6.3.6 is the same as equ.6.3.4, except that the local diffusion coefficient is not a constant in equ.6.3.6. We can simply adjust local diffusion coefficient by:

$$D(c_{en}) = c_s^2\left(\tau_{c_{en}} - \frac{1}{2}\right) \quad (6.3.7)$$

where $\tau_{c_{en}}$ is the local relaxation time at each lattice node.

6.3.2 System Morphologies and Homogenization Method

Two levels of morphologies are used in the simulation. On the cell level, typical "brick and mortar" structures are employed as SC layer. The bricks represent corneocytes with edge length 10 um and thickness of 0.75 um. The mortar represents lipid layer between corneocytes, which has an equal horizontal and vertical gap of 75 nm. A slip ratio is used to control the stacking arrangement of the corneocytes in two adjacent layers. As is shown in Fig.6.1, this ratio is defined as a/b. In this paper, unless otherwise specified, we will fix this ratio as 0.4. Fig.6.1 shows each layer with one unit cell and one layer of lipid. Periodic boundary condition will be applied in the lateral direction. Patch is placed on the top of the SC layer.

At the homogenization level, the SC layer is simplified as a homogeneous rectangular box. A two-layer structure is used to represent the transdermal system, as is depicted in Fig.6.1.

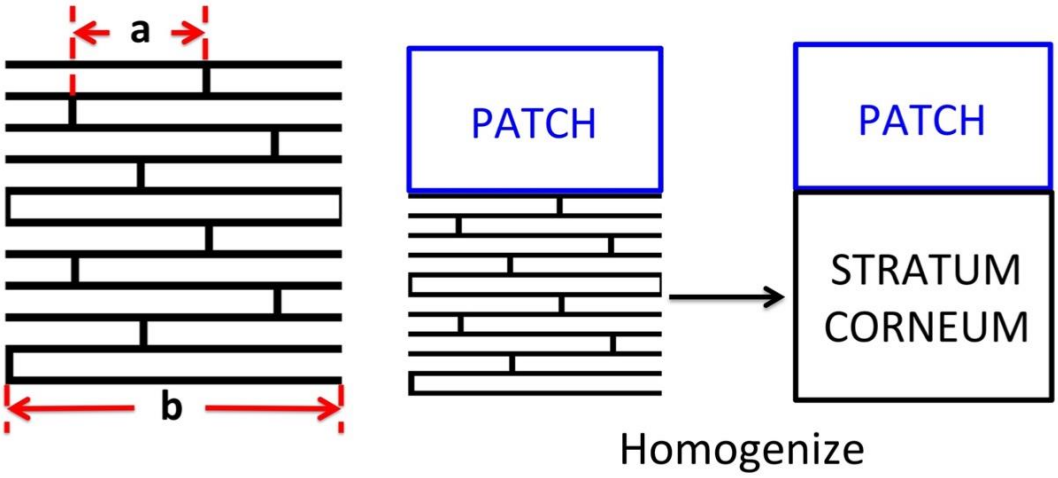

Fig. 6. 1 System morphologies. (left) shows the "brick and mortar" representation of the stratum corneum layer with corneocytes in black and lipid in white. (right) shows the homogenized structure of the patch-stractum-corneum system.

To obtain the effective diffusion coefficients for homogenization, finite difference method is used to solve the steady state flux of drug in the "brick and mortar" structure. For transverse effective diffusion, a fix concentration ρ_0 is applied on the top of the SC layer, and the bottom boundary concentration is fixed as zero. When the system reaches steady state, the Fick's second law can be reduced Laplace equation:

$$\nabla^2 \rho = 0 \qquad (6.3.8)$$

The solution of equ.6.3.8 can give us the concentration distribution of the system, and the steady state out flux can be calculated based Fick's first law on the out flux boundary:

$$J_{trans} = -D\frac{\partial \rho_{out}}{\partial y} \qquad (6.3.9)$$

The principle of effective diffusion is: if we choose the same system size with homogeneous distribution and the same boundary conditions, the effective diffusion coefficient for the homogenized system should be able to give us the same flux value as the "brick and mortar" structure. If the "brick and mortar" structure has a length of ly in the transverse direction, then the homogenized system should have an out flux equal to:

$$J_{trans}^{eff} = -D_{trans}^{eff}\frac{\rho_0}{ly} \qquad (6.3.10)$$

By equating equ.6.3.9 and 6.3.10, we can obtain the effective diffusion coefficient for transverse direction:

$$D_{trans}^{eff} = D\frac{\partial \rho_{out}}{\partial y}\frac{ly}{\rho_0} \qquad (6.3.11)$$

The same method can be applied to obtain the effective diffusion coefficient in the lateral direction.

6.3.3 Boundary Conditions

For the "brick and mortar" structure, since no passive diffusion is considered in the system right now, we apply bounce back boundary condition for corneocytes. Periodic boundary condition is used in the lateral direction, except for the effective lateral diffusion calculation system, in which constant concentration is fixed at the two boundaries in the lateral direction. The Neumann boundary of zero flux is applied at the top of patch.

For homogenized structure, the same boundary conditions are applied at the system boundaries as the "brick and mortar" system, except that there are no corneocytes, therefore no bounce back boundaries, inside of SC layer.

For the interfaces between patch and SC layers, equilibrium partition is used for mass transfer across interfaces, and Neumann boundary of zero flux is applied at the interfaces.

6.3.4 System Parameters

We use fentanyl as the model drug, which was reported to have an averaged diffusion coefficient of 1.2×10^{-7} cm^2/s, and oleic acid as the enhancer, which has the averaged diffusion coefficient of 2.65×10^{-8} cm^2/s in the lipid of SC. In patch, fentanyl and oleic acid are assumed to have the same diffusion coefficient of 1.0×10^{-9} cm^2/s. The partition coefficients of fentanyl and oleic acid from patch to SC are the same, which is 0.14. All these parameters can be found in Rim's paper[221].

6.4 Results and Discussion

6.4.1 Effects of Homogenization

To test the effects of homogenization, we will compare the flux value calculated from a specific "brick and mortar" structure and the flux from the homogenized system with the same size and boundary conditions. Only one component is considered. Fig.6.2 shows the influence of number of cells in each cell layer of the SC in the "brick and mortar" structure. The result indicates that when periodic boundary condition is applied, the one-cell-per-layer representation is large enough to obtain reliable averaged out flux at the boundary. Therefore, all of our following calculations based on "brick and mortar" structures will use one cell in each layer and periodic boundary in the lateral direction.

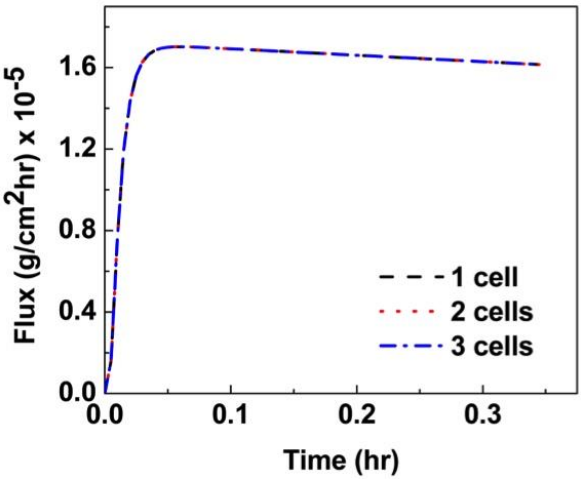

Fig. 6. 2 Flux in "brick and mortar" structure with slip ratio 0.4, cell length10 um and 10 layers of cells. Different number of cells in each layer is compared.

To test the homogenization effects on the out flux, two conditions are applied here. One is the pure SC layer with constant inlet boundary concentration of 0.09 g/cm^3 and outlet concentration of zero. The other is SC and patch layers with initial drug concentration of 0.09 g/cm^3 in patch, and the thickness of patch is 5 um. As is shown in Fig.6.3, generally speaking, the homogenized system can get similar flux as the "brick and mortar" structure after system reaches steady state or after the flux peak. However, the duration time to reach steady state or reach the peak flux is much longer for homogenized system than the "brick and mortar" system. Also, for the SC and patch structure, the peak flux value for homogenized system is smaller than the "brick and mortar" structure. If we use larger corneocytes, we can capture the similar tendency, and the steady state errors tend to be even larger. This may indicate that if we are interested steady state flux or the flux after the peak, a homogenized system may be enough to capture the properties that we want, as long as the cell size is not too large. But the information related to transition state, such as the duration time to reach steady state and the peak flux value, may not be obtained from this homogenization method directly. This is mainly due to the way we define the effective diffusion in the system. Since the effective diffusion coefficient is calculated based on steady state flux only, the transition information is lost in the homogenization.

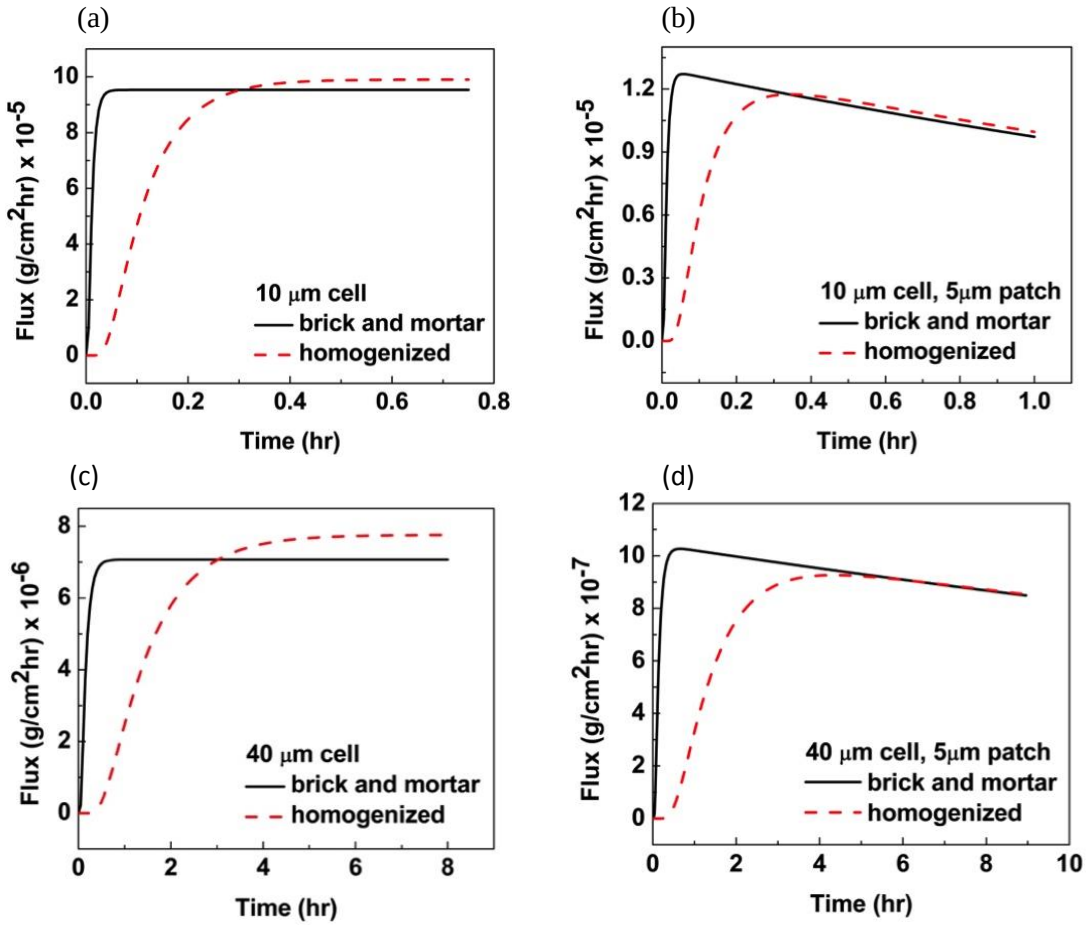

Fig. 6. 3 Comparison of flux in "brick and mortar" and homogenized systems. Cell slip ration is 0.4, and the number of cells layers in the SC is 10. (a) and (b) have cell size of 10 um, (c) and (d) have cell size of 40 um. (a) and (c) are systems with only SC layer. (b) and (d) are systems with SC and patch layers.

6.4.2 Effects of Different Parameters for "Brick and Mortar" System

Since the homogenization may not be a good estimation of the physical system, now we will focus on the "brick and mortar" structure directly and test the sensitivity of out flux to different parameters of the system. We use the parameters in Table.1 as the base case. By varying each parameter in the base case, we can do the sensitivity test.

Table. 6. 1 Test Parameters for Homogenized System

	Parameters	Base case	Test Range
Diffusion Coefficients	D(patch)	1.0e-9 cm^2/s	[0.5, 2, 4]*Base
	D(SC lipid)	1.2e-7 cm^2/s	[0.5, 2, 4]*Base
Partition Coefficeints	patch/SC	0.14	[0.5, 1.5, 2]*Base
Patch Concentration	Initial Density in patch	0.09 g/cm^3	[0.5, 2, 4]*Base
Patch Thickness	Patch Thickness	5 um	[0.4, 2, 3]*Base

6.4.2.1 Effects of Drug Diffusivity in Patch

Fig.6.4 shows the flux and drug distributions (Drug amount is normalized to lattice volume) in the two-layer system with different drug diffusivities in patch. It turns out that the influence of drug diffusivity in patch does not have much influence on the flux and drug distribution, since all the curves are almost identical.

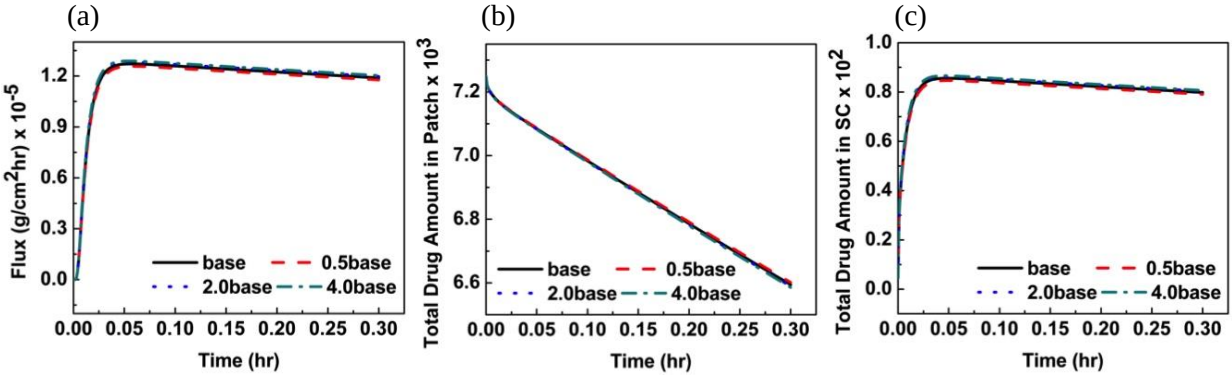

Fig. 6. 4 Flux and drug distributions in the patch-SC system with different drug diffusion coefficients in patch. (a) Flux, (b) Total drug amount left in patch, and (c) Total drug amount in SC.

However, if we look at the peak positions in Fig.6.4a, as is shown in Fig.6.5, we can find that by increasing the diffusivity of drug in patch, the peak time will be shifted earlier a little bit, and the peak flux will increase a little as well. But the shift of time and the increase of flux are very small, and they seem to have a small influence in the system, indicating that the mass transfer in the system is not governed by diffusivity of drug in patch.

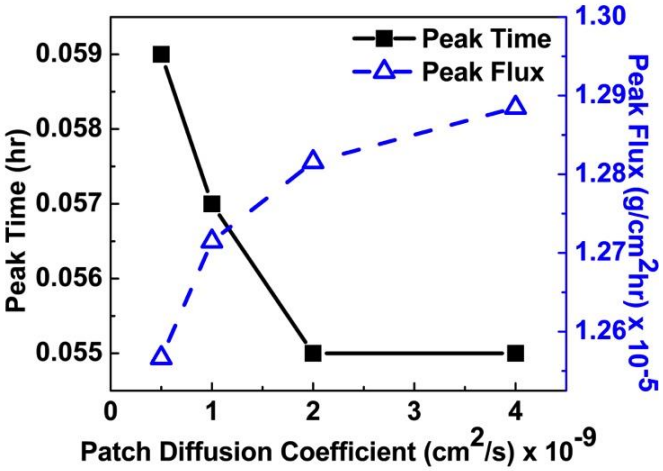

Fig. 6. 5 Peak time and peak flux with different drug diffusion coefficients in patch.

6.4.2.2 Effects of Drug Diffusivity in SC

By increasing the diffusion coefficient of drug in SC layer, we can observe an obvious increase of drug flux in the system (shown in Fig.6.6). The drug concentration in patch will decrease faster with higher diffusivity in SC layer; however, the drug in SC will decrease faster as well. The total amount of drug in SC layer is determined by the relative speed of inlet from patch and outlet to sink boundary. Faster diffusion speed in SC will increase the outlet and thus lead to smaller amount of drug in SC layer.

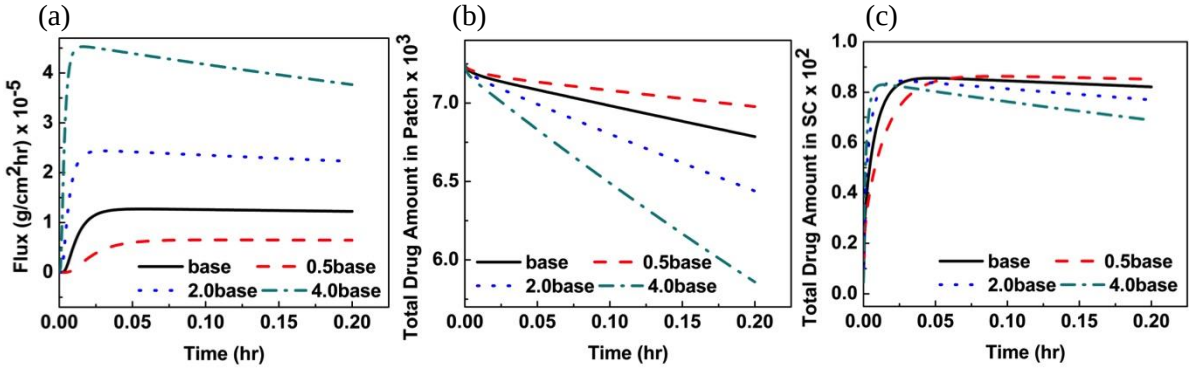

Fig. 6. 6 Flux and drug distributions in the patch-SC system with different drug diffusion coefficients in SC layer. (a) Flux, (b) Total amount of drug left in patch, and (c) Total drug amount in SC.

A more careful investigation on the peak flux information shows that the peak flux values has almost linear relationship with the diffusion coefficient of drug in SC layer (shown in Fig.6.7). Actually, the mathematical components of the system, including the partition and the flux equations, are linear function of concentration gradient. And all of these components are linked together in series. Therefore, if the amount of drug in patch does not decrease too much, we should be able to get a linear relationship here. Also, we can find that the higher diffusion in SC will shift the peak time earlier, and the shift is not linearly with diffusivity.

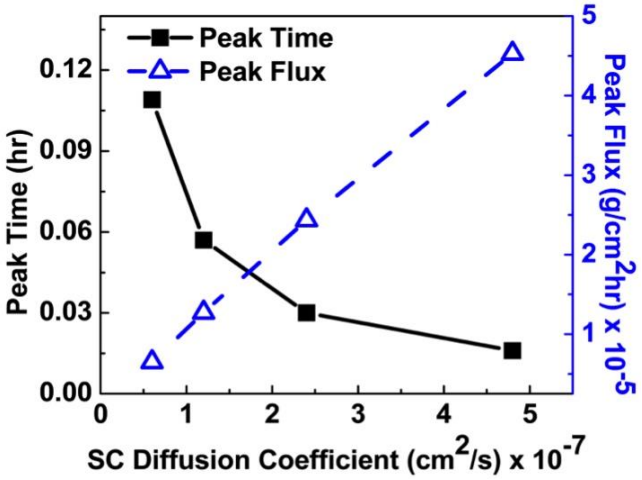

Fig. 6. 7 Peak time and peak flux with different drug diffusion coefficients in SC.

6.4.2.3 Effects of Partition Coefficient

The flux of drug will increase with an increase of the partition coefficient at the patch/SC interface (shown in Fig.6.8). Drug amount left in patch will decrease with faster speed as the partition coefficient increases, because higher partition coefficient will increase the transfer from patch to SC. The consequence is higher inlet to the SC and therefore, the amount of drug in SC layer will increases as the partition coefficient increases.

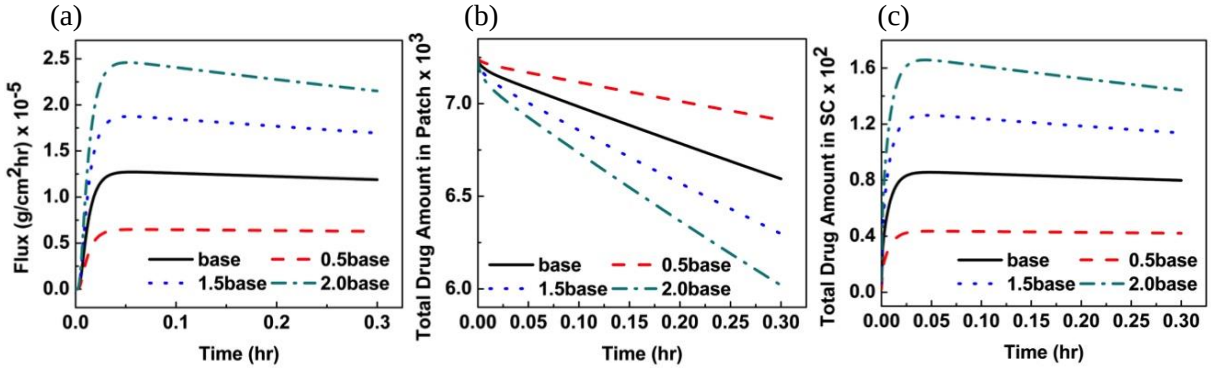

Fig. 6. 8 Flux and drug distributions in the patch-SC system with different partition coefficients at patch/SC interface. (a) Flux, (b) Total amount of drug left in patch, and (c) Total drug amount in SC.

The peak flux will increase linearly with the increase of partition coefficient and the peak time will decrease with the increase of partition coefficient (shown in Fig.6.9). The reason for the linearity should be the same as what we mentioned before in section 6.4.2.2.

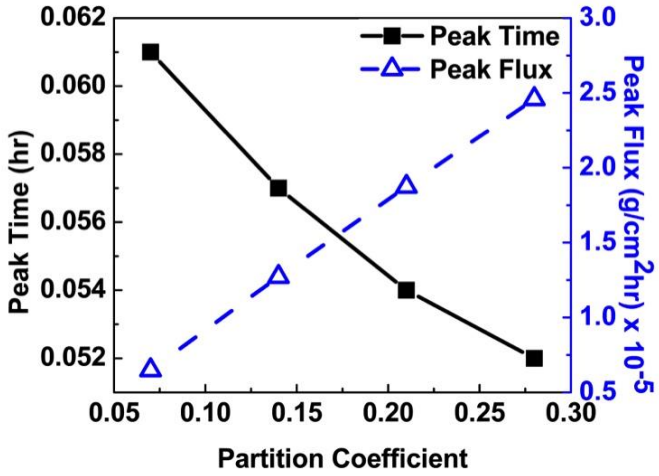

Fig. 6. 9 Peak time and peak flux with different partition coefficients.

6.4.2.4 Effects of Initial Patch Concentration

As is shown in Fig.6.10, the flux of drug, the amount of drug left in patch, and the amount of drug in SC layer will increase as the patch concentration increases. This is just simply because the inlet flux into SC layer increases as the patch concentration increases, due to the linear partition at the interface.

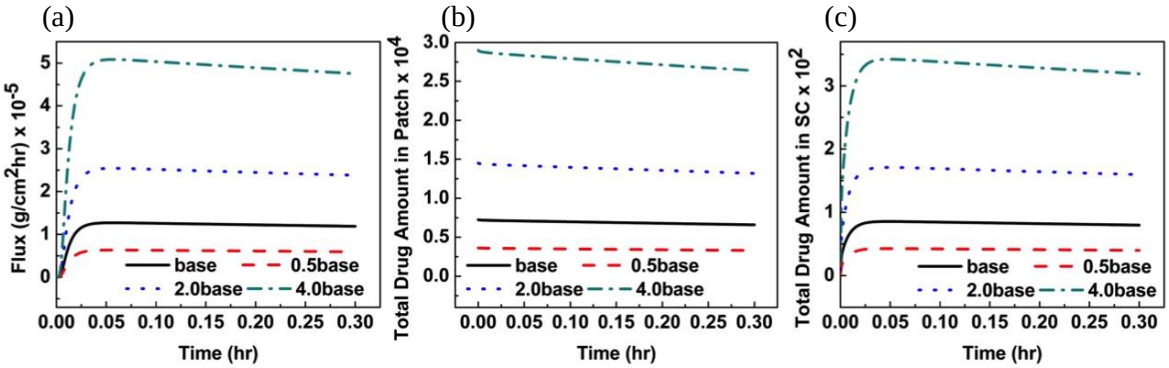

Fig. 6. 10 Flux and drug distributions in the patch-SC system with different initial patch concentrations. (a) Flux, (b) Total amount of drug left in patch, and (c) Total drug amount in SC.

As we can expect, the linear property of the system leads to the linear relation of the peak flux to the initial patch concentration (shown in Fig.6.11). An interesting observation is that the peak time is almost unchanged as the initial patch concentration increases. This is also due to the linear property of the system. The larger initial concentration in patch will only "rescale" the numerical values in the system to a larger value, but the relative relation of numerical values will stay the same.

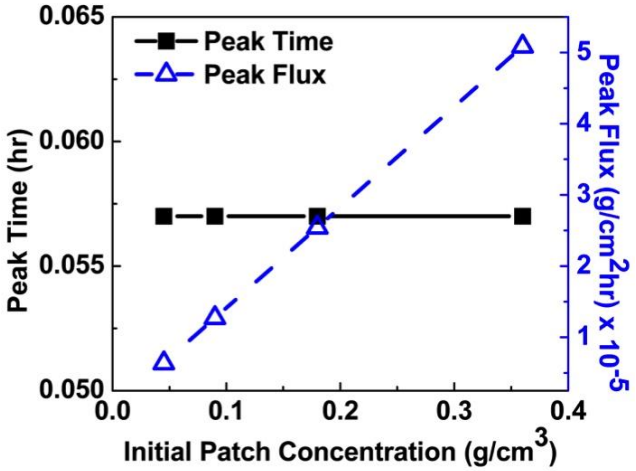

Fig. 6. 11 Peak time and peak flux with different initial patch concentrations.

6.4.2.5 Effects of Patch Thickness

The patch thickness seems to have small effects on the drug flux in the system. Fig.6.12 shows that the drug flux will decay faster with smaller patch thickness. However, when the patch thickness is larger than a certain value, the difference in the decay speed will be indistinguishable in a short period of time. This flux decay is mainly due to insufficient amount of drug in the patch. Therefore, we can observe smaller amount of drug both in patch and SC when the patch thickness decreases.

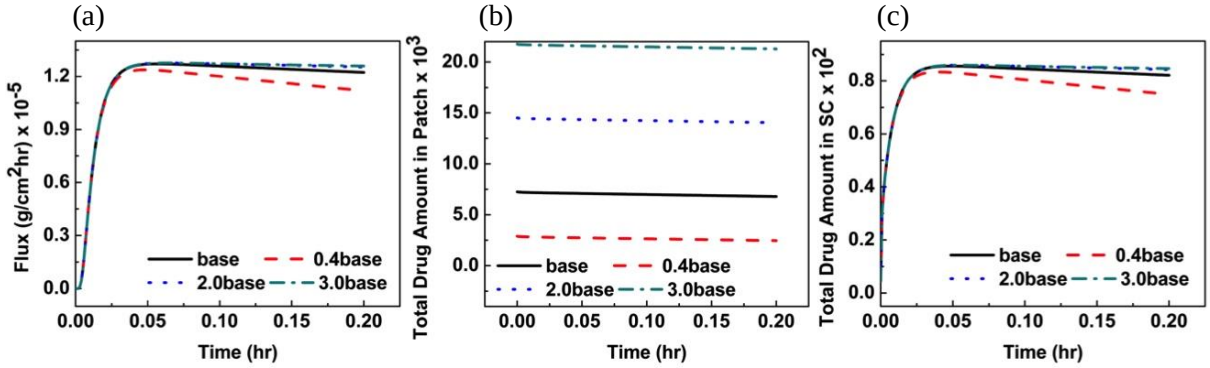

Fig. 6. 12 Flux and drug distributions in the patch-SC system with different patch thickness. (a) Flux, (b) Total amount of drug left in patch, and (c) Total drug amount in SC.

Fig.6.13 shows that the patch thickness has a limited influence on the peak flux and peak time. As the thickness increases, both peak time and peak flux will increase and then reach a maximum value. This indicates that when the patch thickness is large enough, it will have little influence on the mass transfer in the system.

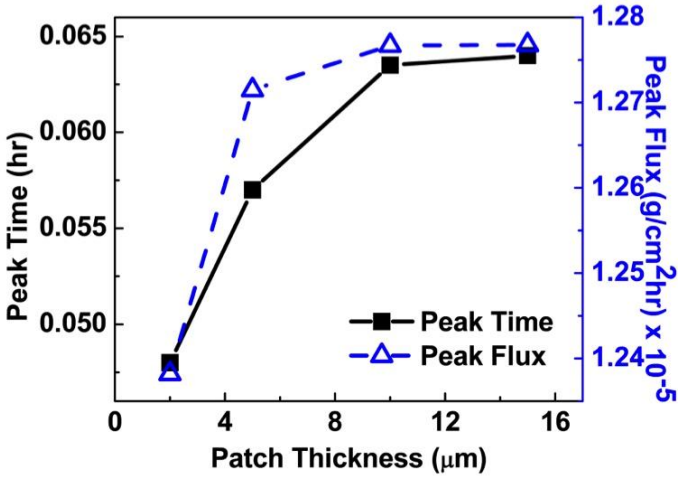

Fig. 6. 13 Peak time and peak flux with different initial patch concentrations.

6.4.2.6 Comparison of Different Parameters

Fig.6.14 compares the peak time and peak flux under different parameters. The changes of the testing parameters are in the unit of base parameters shown in Table.6.1. The results indicate that the flux in the system is governed by the partition coefficient at patch/SC interface, the initial patch concentration and the diffusivity of drug in SC layer. And the peak flux has almost linear relationship with these three parameters. Patch thickness and patch diffusion coefficient seems to have very little influence on flux in the test range. We should note that if we change these two parameters to some extreme values, they could become the governing factors of the system.

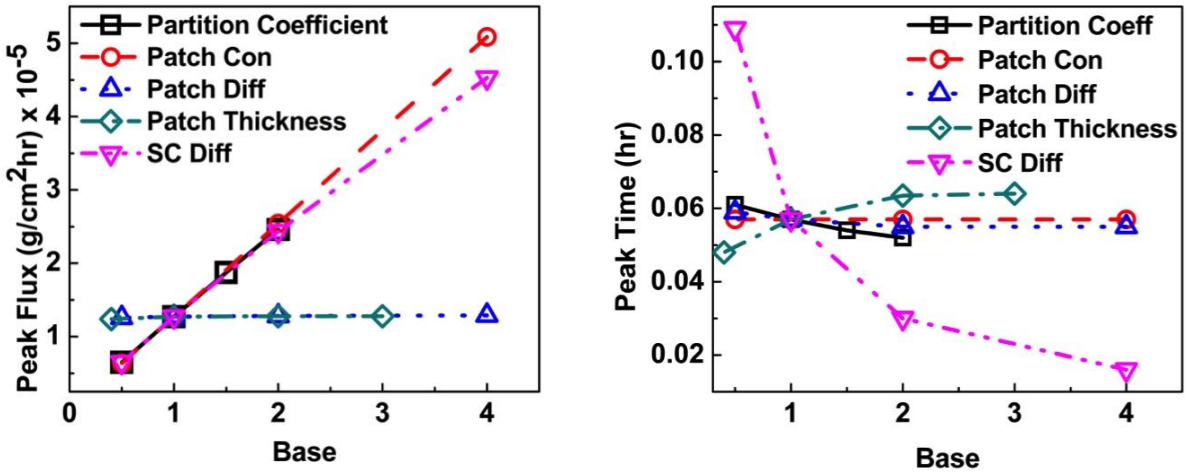

Fig. 6. 14 Comparison of peak flux (left) and peak time (right) under different testing parameters.

The peak time of the system is more sensitive to the diffusion coefficient of drug in SC, patch thickness and partition coefficient at patch/SC interface. Of these three parameters, the diffusion coefficient of drug in SC has the largest effects. The peak time will be delayed as the patch thickness increases.

Therefore, on the whole, within the testing range, the governing factors for the system should be the partition coefficient at patch/SC interface and the diffusion coefficient of drug in SC layer.

6.4.3 Effects of Enhancer

As is previously mentioned, the solution of homogenized system may deviate from the "brick and mortar" system at transient state. For the anisotropic diffusion of drug with enhancer, the system will always be in the "transient state", as long as the amount of enhancer in the patch is finite. Therefore, the simple homogenization method may not be an ideal model for such a system, and here we will test the effects of enhancer in "brick and mortar" structure directly.

For testing purpose, we use a simple linear relation to demonstrate the effect of local concentration of enhancer on the local diffusion coefficient of drug, which was proved in previous work by Rim, etc.[221]:

$$D_{drug} = 2.03 \times 10^{-6} c_{enhancer} + 1.2 \times 10^{-7} \qquad (6.4.1)$$

where the "drug" stands for fentanyl and the "enhancer" stands for oleic acid. The unit of diffusion coefficient is cm^2/s, and the unit of concentration is g/cm^3. A simplified patch-SC structure is used, which is the same as what we applied for testing the effects of homogenization in section 6.4.1. The length of cell in SC layer is assumed to be 10 um and there are 10 layers of cell in this layer. Patch has a finite thickness of 5 um. Periodic boundary condition is applied in the lateral direction. The diffusion coefficient of enhancer is assumed to be independent of the concentration of drug and enhancer itself, with the constant value of 2.65×10^{-8} cm^2/s. The partition at the patch/SC interface is assumed to be the same for both patch and enhancer, with the value of 0.14. By adjusting the initial concentrations of enhancer in the patch (0, 0.06, 0.13, 0.20, 0.25 g/cm^3), we can check the influence of enhancer on the flux of the system.

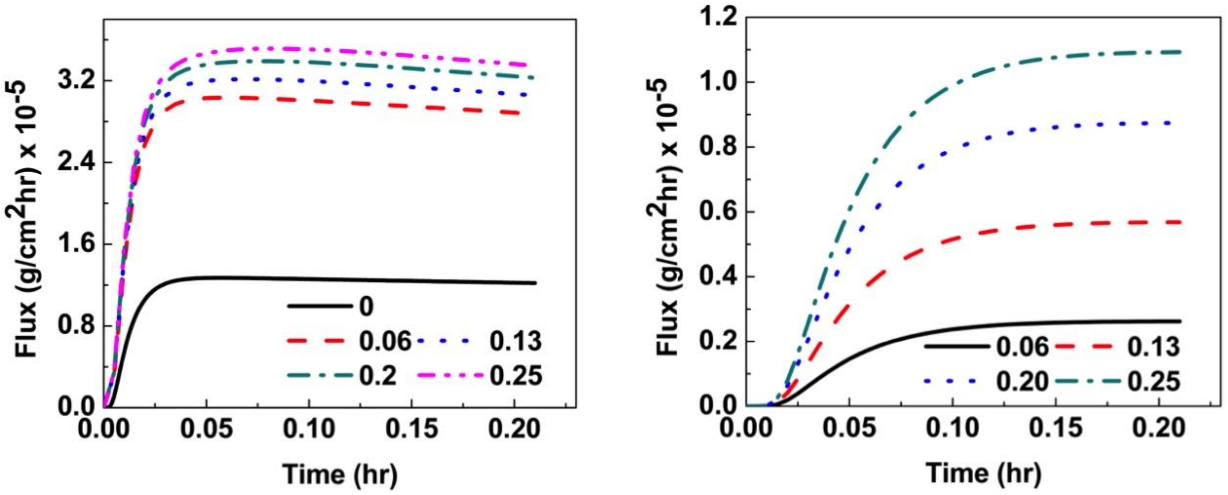

Fig. 6. 15 Outlet flux with different initial concentrations of enhancer in patch. Enhancer has higher diffusivity in SC than drug. (left) Drug flux. (right) Enhancer flux.

Fig.6.15 shows the flux at the outlet boundary of SC layer for drug and enhancer with different initial concentration of enhancer in patch. It is not surprising that the larger concentration of enhancer leads to larger flux of drug in the system. The flux of enhancer is also higher with larger initial concentration in patch. However, the peak flux time for drug does not necessarily match the peak flux time for enhancer. In this system, the peak time for drug is much earlier than the peak time for enhancer.

Notice that the diffusion coefficient for drug is almost one to two magnitudes higher than it is for the enhancer. Therefore, enhancer will travel much slower than drug. In the meantime, the drug concentration in the patch will drop, which will limit the inlet of drug into the SC layer. These two factors will lead to the mismatch of the peak time of the two components.

If we choose an enhancer that will travel faster than drug, we can actually observe earlier flux peak for enhancer than the drug (shown in Fig.6.16). In Fig.6.16, the diffusion coefficient of drug in SC layer is set to be $8.0\times\ 10^{-7}\text{cm}^2/\text{s}$, which is 6 times larger than the diffusion coefficient of drug.

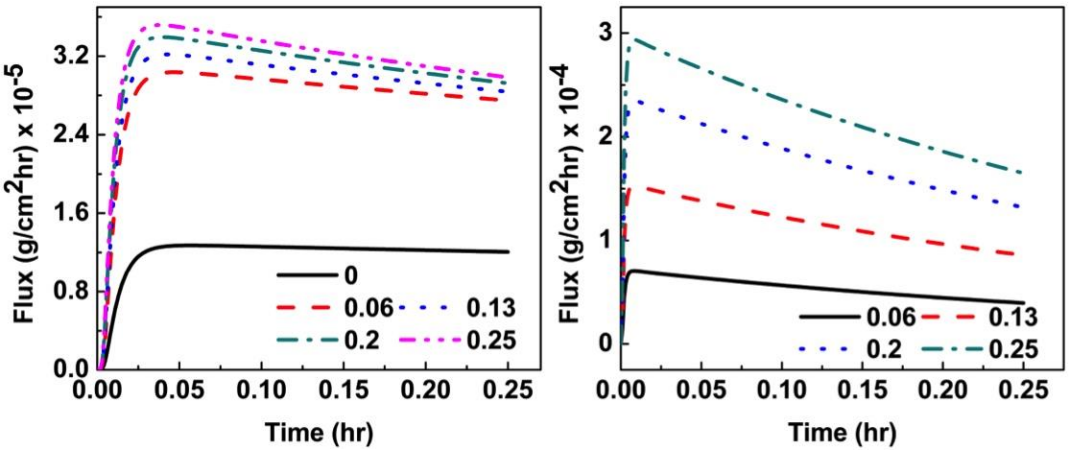

Fig. 6. 16 Outlet flux with different initial concentrations of enhancer in patch. Enhancer has higher diffusivity in SC than drug. (left) Drug flux. (right) Enhancer

Fig.6.17 shows the peaks time and the peak flux value of drug with different initial concentration of enhancer in the patch. It indicates that the peak time will be "lagged" to later time with higher initial concentration of enhancer, if the enhancer has smaller diffusivity than drug; while the peak time could be "pushed" earlier with higher concentration of enhancer, if the enhancer has higher diffusivity than drug. The peak flux value in these two cases does not vary too much. This gives us a hint that we can adjust the peak time of the drug by using different kinds of enhancers in the system. Enhancer with faster diffusion speed than drug may push the peak time earlier; while the enhancer with mush slower diffusion speed may drag the peak time later.

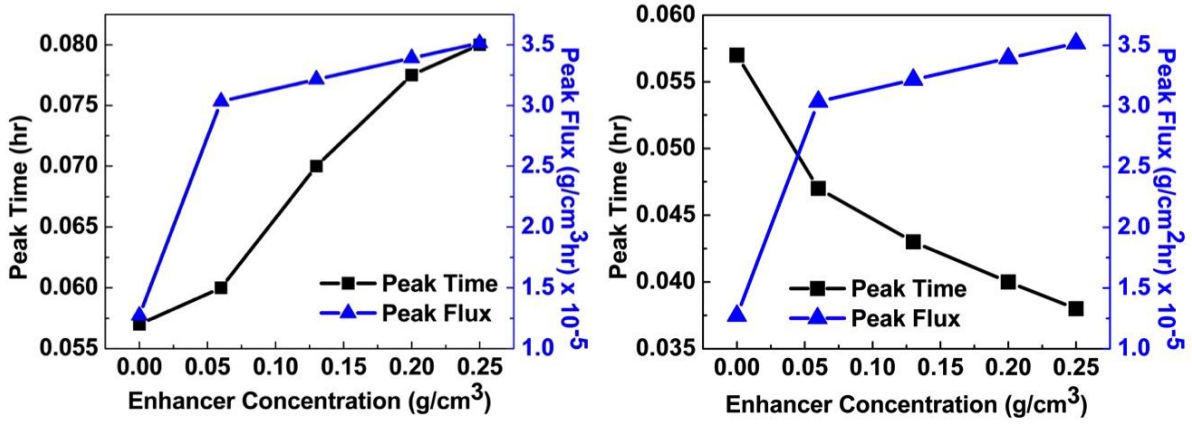

Fig. 6. 17 Peak time and peak flux value of drug with different enhancer concentrations. (left) Enhancer has smaller diffusivity than drug. (right) Enhancer has higher diffusivity than drug.

Fig.6.17 also shows that the enhancer will increase the peak flux of drug in a linearly manner, which might be mainly due to the linear relationship between the local concentration of enhancer and the local diffusion coefficient of drug depicted in equ.6.4.1.

6.5 Conclusion

In this chapter, we mainly introduced a new numerical method, Lattice Boltzmann Method, to simulate the transdermal drug delivery system. Two kinds of transdermal structures are discussed: "brick and mortar" structure and a simple homogenized structure. We demonstrated that the homogenized system is able to obtain similar steady state flux as the "brick and mortar" structure; however, in the early transient region, their flux value can be different.

We tested the influence of different system parameters on the outlet flux of drug, the drug distribution in each layer, and the peak flux and peak flux time. It turns out that in this system, the rate-determine step for mass transfer should be the partition between patch and SC layers and the diffusion in the SC layer.

The influence of enhancer is tested. Our results show that by adding enhancers, the drug flux can be significantly increased. However, the peak time of drug does not necessarily match the peak flux time for enhancer. The peak time of drug might be adjusted (pushed earlier or dragged later) by using different kinds of enhancers, which has higher/smaller diffusivity than drug in the system.

Future Work

I. Diffuse Charge Dynamics in Electric Double Layer Capacitors

It should be straightforward to test the high potential system. When the applied potential is high, the charge v.s. potential should not follow the linear relation and the steric effect can be higher. The stern layer capacitance can be added into the system by changing the value of δ to non-zero values directly or by MD simulations to obtain the capacitance value numerically. It is important to extend the simulation system into 3D to monitor the microstructure of real electrode systems. Also, it should be possible to add the heat convection effects into the mass transfer process in a modular manner.

II. Dendrite Formation on the Anode of Li-ion Batteries

The formation of SEI layer plays an important role in the dendrite formation process. The SEI effects can be added to the system by using Monte Carlo Method to adjust the local reactivity according to an imaginary thin layer at the electrode-electrolyte interface, or by using Lattice Spring Model to simulate the dendrite-SEI interaction directly. The growth induced convection and heat convection in the electrolyte can be added to the model in a modular manner. Also, it should be possible to extend the model into 3D straightforwardly.

III. Intercalation Reaction in Graphite Electrode of Li-ion Batteries

It should be possible to add the effect of SEI in a modular manner, which will increase electrode resistance and consume electrolyte. A whole cell simulation (including the intercalation reaction of cathode materials) can be useful to foretell the performance of a battery system, and can be simulated in the similar way as we discussed in the thesis. Different micro-filler (spheres and fibers, etc.) and their distributions can be tested to optimize the battery performance.

IV. Transdermal Drug Delivery

A more accurate homogenization method is needed to simplify the simulation when we extend the system into 3D. This can be done by following the more sophisticated homogenization methods in other porous structure studies. Non-regular cell morphologies can be introduced into the system to represent more realistic condition. Passive diffusion of drug should be added into the model in a straightforward way.

Reference

1. Kleven, M., M.C. Melaaen, and P.G. Djupesland, *Computational Fluid Dynamics (Cfd) Applied in the Drug Delivery Design Process to the Nasal Passages: A Review.* Journal of Mechanics in Medicine and Biology, 2012. **12**(1).
2. Bhutta, M.M.A., et al., *CFD applications in various heat exchangers design: A review.* Applied Thermal Engineering, 2012. **32**: p. 1-12.
3. Kadau, K., et al., *Atomistic methods in fluid simulation.* Philosophical Transactions of the Royal Society a-Mathematical Physical and Engineering Sciences, 2010. **368**(1916): p. 1547-1560.
4. *Non-equilibrium thermodynamics*. Available from: http://en.wikipedia.org/wiki/Non-equilibrium_thermodynamics.
5. McNamara, G.R. and G. Zanetti, *Use of the Boltzmann Equation to Simulate Lattice-Gas Automata.* Physical Review Letters, 1988. **61**(20): p. 2332-2335.
6. Higuera, F.J. and J. Jimenez, *Boltzmann Approach to Lattice Gas Simulations.* Europhysics Letters, 1989. **9**(7): p. 663-668.
7. Chen, S. and G.D. Doolen, *Lattice Boltzmann method for fluid flows.* Annual Review of Fluid Mechanics, 1998. **30**: p. 329-364.
8. Aidun, C.K. and J.R. Clausen, *Lattice-Boltzmann Method for Complex Flows.* Annual Review of Fluid Mechanics, 2010. **42**: p. 439-472.
9. Wang, H.M., G.W. Yan, and B. Yan, *Lattice Boltzmann Model Based on the Rebuilding-Divergency Method for the Laplace Equation and the Poisson Equation.* Journal of Scientific Computing, 2011. **46**(3): p. 470-484.
10. Dhumieres, D., P. Lallemand, and U. Frisch, *Lattice Gas Models for 3d Hydrodynamics.* Europhysics Letters, 1986. **2**(4): p. 291-297.
11. Frisch, U., B. Hasslacher, and Y. Pomeau, *Lattice-Gas Automata for the Navier-Stokes Equation.* Physical Review Letters, 1986. **56**(14): p. 1505-1508.
12. Frisch, U. and J.P. Rivet, *Lattice Gas Hydrodynamics - Green-Kubo Formula.* Comptes Rendus De L Academie Des Sciences Serie Ii, 1986. **303**(12): p. 1065-1068.
13. Dominique d'Humieres, P.L., *Numerical Experiments on Lattice Gases: Mixtures and Galilean Invariance.* Complex Systems, 1987. **1**: p. 633-647.
14. He, X.Y., N. Li, and B. Goldstein, *Lattice Boltzmann simulation of diffusion-convection systems with surface chemical reaction.* Molecular Simulation, 2000. **25**(3-4): p. 145-156.
15. Kang, Q.J., D.X. Zhang, and S.Y. Chen, *Simulation of dissolution and precipitation in porous media.* Journal of Geophysical Research-Solid Earth, 2003. **108**(B10).
16. Kang, Q.J., et al., *Lattice Boltzmann simulation of chemical dissolution in porous media.* Physical Review E, 2002. **65**(3).
17. Jia, X. and R.A. Williams, *A hybrid mesoscale modelling approach to dissolution of granules and tablets.* Chemical Engineering Research & Design, 2007. **85**(A7): p. 1027-1038.
18. Yoshida, H., T. Kinjo, and H. Washizu, *Coupled lattice Boltzmann method for simulating electrokinetic flows: A localized scheme for the Nernst-Plank model.* Communications in Nonlinear Science and Numerical Simulation, 2014. **19**(10): p. 3570-3590.
19. Wang, M.R. and Q.J. Kang, *Modeling electrokinetic flows in microchannels using coupled lattice Boltzmann methods.* Journal of Computational Physics, 2010. **229**(3): p. 728-744.

20. Yang, X.G., et al., *A Coupled Lattice Boltzmann Method to Solve Nernst-Planck Model for Simulating Electro-osmotic Flows.* Journal of Scientific Computing, 2014. **61**(1): p. 222-238.
21. Miller, W. and S. Succi, *A lattice Boltzmann model for anisotropic crystal growth from melt.* Journal of Statistical Physics, 2002. **107**(1-2): p. 173-186.
22. Miller, W., S. Succi, and D. Mansutti, *Lattice Boltzmann model for anisotropic liquid-solid phase transition.* Physical Review Letters, 2001. **86**(16): p. 3578-3581.
23. Du, G., et al., *Computational electrochemistry: Lattice Boltzmann simulations of voltammetry at microelectrodes.* Electrochemistry Communications, 2007. **9**(10): p. 2519-2524.
24. He, X.Y. and N. Li, *Lattice Boltzmann simulation of electrochemical systems.* Computer Physics Communications, 2000. **129**(1-3): p. 158-166.
25. Zhang, J.Y. and G.W. Yan, *A lattice Boltzmann model for the nonlinear Schrodinger equation.* Journal of Physics a-Mathematical and Theoretical, 2007. **40**(33): p. 10393-10405.
26. Zhong, L.H., et al., *Lattice Boltzmann schemes for the nonlinear Schrodinger equation.* Physical Review E, 2006. **74**(3).
27. Succi, S., *The Lattice Boltzmann Equation for Fluid Dynamics and Beyond*. Numerical Mathematics and Scientific Computation, ed. R.J. G. H. Golub, W. A. Light, E. Suli. 2001: Oxford University Press.
28. Wolf-Gladrow, D.A., *Lattice-Gas Cellular Automata and Lattice Boltzmann Models: An Introduction*. 2000: Springer-Verlag Berlin Heidelberg.
29. Mohamad, A.A., *Lattice Boltzmann Method Fundamentals and Engineering Applications with Computer Codes*. 2011: Springer-Verlag London.
30. Camas, B.S., *Lattice Boltzmann Modeling for Mass Transport Equations in Porous Media*. 2008, Louisiana State University.
31. Ryu, S. and S. Ko, *Direct numerical simulation of nucleate pool boiling using a two-dimensional lattice Boltzmann method.* Nuclear Engineering and Design, 2012. **248**: p. 248-262.
32. Luoding Zhu , G.H., Shizhao Wang ‡, Laura Miller ⋆, Xing Zhang ‡, Qian You ⋄, Shiaofen Fang *An immersed boundary method by the lattice Boltzmann approach in three dimensions with application.*
33. Guo, Z.L., C.G. Zheng, and B.C. Shi, *An extrapolation method for boundary conditions in lattice Boltzmann method.* Physics of Fluids, 2002. **14**(6): p. 2007-2010.
34. Yang, Z., *Analysis of Lattice Boltzmann Boundary Conditions*. 2007, University of Kaiser- slautern, University of Saarland, University of Constance.
35. Wu, J. and C. Shu, *Implicit velocity correction-based immersed boundary-lattice Boltzmann method and its applications.* Journal of Computational Physics, 2009. **228**(6): p. 1963-1979.
36. Lee, L. and I. Vankova, *A class of Cartesian grid embedded boundary algorithms for incompressible flow with time-varying complex geometries.* Physica D-Nonlinear Phenomena, 2011. **240**(20): p. 1583-1592.
37. Oulaid, O., Q. Chen, and J.F. Zhang, *Accurate boundary treatments for lattice Boltzmann simulations of electric fields and electro-kinetic applications.* Journal of Physics a-Mathematical and Theoretical, 2013. **46**(47).

38. Zou, Q.S. and X.Y. He, *On pressure and velocity boundary conditions for the lattice Boltzmann BGK model.* Physics of Fluids, 1997. **9**(6): p. 1591-1598.
39. Geback, T. and A. Heintz, *A Lattice Boltzmann Method for the Advection-Diffusion Equation with Neumann Boundary Conditions.* Communications in Computational Physics, 2014. **15**(2): p. 487-505.
40. Shao, J.Y., C. Shu, and Y.T. Chew, *Development of an immersed boundary-phase field-lattice Boltzmann method for Neumann boundary condition to study contact line dynamics.* Journal of Computational Physics, 2013. **234**: p. 8-32.
41. Chen, Q., X.B. Zhang, and J.F. Zhang, *Numerical simulation of Neumann boundary condition in the thermal lattice Boltzmann model.* International Journal of Modern Physics C, 2014. **25**(8).
42. Machado, R., *On pressure and corner boundary conditions with two lattice Boltzmann construction approaches.* Mathematics and Computers in Simulation, 2012. **84**: p. 26-41.
43. Guo, Z.L., C.G. Zheng, and B.C. Shi, *Non-equilibrium extrapolation method for velocity and pressure boundary conditions in the lattice Boltzmann method.* Chinese Physics, 2002. **11**(4): p. 366-374.
44. Zhang, J.F. and D.Y. Kwok, *Pressure boundary condition of the lattice Boltzmann method for fully developed periodic flows.* Physical Review E, 2006. **73**(4).
45. Ginzburg, I., F. Verhaeghe, and D. d'Humieres, *Two-relaxation-time Lattice Boltzmann scheme: About parametrization, velocity, pressure and mixed boundary conditions.* Communications in Computational Physics, 2008. **3**(2): p. 427-478.
46. Junk, M. and Z.X. Yang, *Pressure boundary condition for the lattice Boltzmann method.* Computers & Mathematics with Applications, 2009. **58**(5): p. 922-929.
47. Salazar, A.N. and J. Harting, *Evaluation of Pressure Boundary Conditions for Permeability Calculations Using the Lattice-Boltzmann Method.* Advances in Applied Mathematics and Mechanics, 2010. **2**(5): p. 685-700.
48. Cheng, H.H., et al., *Extended hybrid pressure and velocity boundary conditions for D3Q27 lattice Boltzmann model.* Applied Mathematical Modelling, 2012. **36**(5): p. 2031-2055.
49. Abruna, H.D., Y. Kiya, and J.C. Henderson, *Batteries and electrochemical capacitors.* Physics Today, 2008. **61**(12): p. 43-47.
50. Faggioli, E., et al., *Supercapacitors for the energy management of electric vehicles.* Journal of Power Sources, 1999. **84**(2): p. 261-269.
51. Dunn, B., H. Kamath, and J.M. Tarascon, *Electrical Energy Storage for the Grid: A Battery of Choices.* Science, 2011. **334**(6058): p. 928-935.
52. Simon, P. and Y. Gogotsi, *Materials for electrochemical capacitors.* Nature Materials, 2008. **7**(11): p. 845-854.
53. Park, G.L., A.I. Schafer, and B.S. Richards, *Renewable energy-powered membrane technology: Supercapacitors for buffering resource fluctuations in a wind-powered membrane system for brackish water desalination.* Renewable Energy, 2013. **50**: p. 126-135.
54. Ebrahimi, H., et al., *Electrochemical Detection of Piezoelectric Effect from Misaligned Zinc Oxide Nanowires Grown on a Flexible Electrode.* Electrochimica Acta, 2014. **134**: p. 435-441.
55. Xiang, C.C., et al., *A reduced graphene oxide/Co3O4 composite for supercapacitor electrode.* Journal of Power Sources, 2013. **226**: p. 65-70.

56. Chmiola, J., et al., *Anomalous increase in carbon capacitance at pore sizes less than 1 nanometer.* Science, 2006. **313**(5794): p. 1760-1763.
57. Xing, W., et al., *Superior electric double layer capacitors using ordered mesoporous carbons.* Carbon, 2006. **44**(2): p. 216-224.
58. Portet, C., et al., *Capacitance of KOH activated carbide-derived carbons.* Physical Chemistry Chemical Physics, 2009. **11**(25): p. 4943-4945.
59. Dong, X.C., et al., *3D Graphene-Cobalt Oxide Electrode for High-Performance Supercapacitor and Enzymeless Glucose Detection.* Acs Nano, 2012. **6**(4): p. 3206-3213.
60. Lu, X.H., et al., *Hydrogenated TiO2 Nanotube Arrays for Supercapacitors.* Nano Letters, 2012. **12**(3): p. 1690-1696.
61. Wu, Z.S., et al., *Three-Dimensional Graphene-Based Macro- and Mesoporous Frameworks for High-Performance Electrochemical Capacitive Energy Storage.* Journal of the American Chemical Society, 2012. **134**(48): p. 19532-19535.
62. Kim, M., I. Oh, and J. Kim, *Hierarchical porous silicon carbide with controlled micropores and mesopores for electric double layer capacitors.* Journal of Power Sources, 2015. **282**: p. 277-285.
63. Sharma, P. and T.S. Bhatti, *A review on electrochemical double-layer capacitors.* Energy Conversion and Management, 2010. **51**(12): p. 2901-2912.
64. Varghese, J., H.N. Wang, and L. Pilon, *Simulating Electric Double Layer Capacitance of Mesoporous Electrodes with Cylindrical Pores.* Journal of the Electrochemical Society, 2011. **158**(10): p. A1106-A1114.
65. Devillers, N., et al., *Review of characterization methods for supercapacitor modelling.* Journal of Power Sources, 2014. **246**: p. 596-608.
66. Torregrossa, D., et al., *Improvement of Dynamic Modeling of Supercapacitor by Residual Charge Effect Estimation.* Ieee Transactions on Industrial Electronics, 2014. **61**(3): p. 1345-1354.
67. Lee, J., et al., *Modeling of the Electrical and Thermal Behaviors of an Ultracapacitor.* Energies, 2014. **7**(12): p. 8264-8278.
68. Miranda, A.G. and C.W. Hong, *Integrated modeling for the cyclic behavior of high power Li-ion batteries under extended operating conditions.* Applied Energy, 2013. **111**: p. 681-689.
69. Choi, H.S. and C.R. Park, *Theoretical guidelines to designing high performance energy storage device based on hybridization of lithium-ion battery and supercapacitor.* Journal of Power Sources, 2014. **259**: p. 1-14.
70. Vangaveti, S. and A. Travesset, *General solution to the electric double layer with discrete interfacial charges.* Journal of Chemical Physics, 2012. **137**(6).
71. Merlet, C., et al., *Computer simulations of ionic liquids at electrochemical interfaces.* Physical Chemistry Chemical Physics, 2013. **15**(38): p. 15781-15792.
72. Burt, R., G. Birkett, and X.S. Zhao, *A review of molecular modelling of electric double layer capacitors.* Physical Chemistry Chemical Physics, 2014. **16**(14): p. 6519-6538.
73. Cazade, P.A., R. Hartkamp, and B. Coasne, *Structure and Dynamics of an Electrolyte Confined in Charged Nanopores.* Journal of Physical Chemistry C, 2014. **118**(10): p. 5061-5072.
74. Wang, Z.X., et al., *Evaluation of the constant potential method in simulating electric double-layer capacitors.* Journal of Chemical Physics, 2014. **141**(18).

75. Rezaei, M., A.R. Azimian, and D. Toghraie, *Molecular dynamics study of an electro-kinetic fluid transport in a charged nanochannel based on the role of the stern layer.* Physica a-Statistical Mechanics and Its Applications, 2015. **426**: p. 25-34.
76. Wang, H.N. and L. Pilon, *Mesoscale modeling of electric double layer capacitors with three-dimensional ordered structures.* Journal of Power Sources, 2013. **221**: p. 252-260.
77. Singh, M.B. and R. Kant, *Debye-Falkenhagen dynamics of electric double layer in presence of electrode heterogeneities.* Journal of Electroanalytical Chemistry, 2013. **704**: p. 197-207.
78. Bazant, M.Z., K. Thornton, and A. Ajdari, *Diffuse-charge dynamics in electrochemical systems.* Physical Review E, 2004. **70**(2).
79. Kilic, M.S., M.Z. Bazant, and A. Ajdari, *Steric effects in the dynamics of electrolytes at large applied voltages. II. Modified Poisson-Nernst-Planck equations.* Physical Review E, 2007. **75**(2).
80. Kilic, M.S., M.Z. Bazant, and A. Ajdari, *Steric effects in the dynamics of electrolytes at large applied voltages. I. Double-layer charging.* Physical Review E, 2007. **75**(2).
81. Zhao, H., *Diffuse-charge dynamics of ionic liquids in electrochemical systems.* Physical Review E, 2011. **84**(5).
82. Staser, J.A. and J.W. Weidner, *Mathematical Modeling of Hybrid Asymmetric Electrochemical Capacitors.* Journal of the Electrochemical Society, 2014. **161**(8): p. E3267-E3275.
83. Sin, J.S., S.J. Im, and K.I. Kim, *Asymmetric electrostatic properties of an electric double layer: a generalized Poisson-Boltzmann approach taking into account non-uniform size effects and water polarization.* Electrochimica Acta, 2015. **153**: p. 531-539.
84. Sikha, G., R.E. White, and B.N. Popov, *A mathematical model for a lithium-ion battery/electrochemical capacitor hybrid system.* Journal of the Electrochemical Society, 2005. **152**(8): p. A1682-A1693.
85. Skinner, B., et al., *Theory of volumetric capacitance of an electric double-layer supercapacitor.* Physical Review E, 2011. **83**(5).
86. Chirkov, Y.G. and V.I. Rostokin, *Computer Simulation of Active Layers in the Electric Double Layer Supercapacitor: Optimization of Active Layer Charging Modes and Structure, Calculation of Overall Characteristics.* Russian Journal of Electrochemistry, 2014. **50**(3): p. 208-222.
87. Chirkov, Y.G. and V.I. Rostokin, *Computer Simulation of Active Layers in Double-Layer Supercapacitors: Galvanostatics, Determination of Effective Coefficients, and Calculation of Overall Characteristics.* Russian Journal of Electrochemistry, 2014. **50**(1): p. 13-26.
88. Mcnamara, G.R. and G. Zanetti, *Use of the Boltzmann-Equation to Simulate Lattice-Gas Automata.* Physical Review Letters, 1988. **61**(20): p. 2332-2335.
89. Ginzburg, I., *Equilibrium-type and link-type lattice Boltzmann models for generic advection and anisotropic-dispersion equation.* Advances in Water Resources, 2005. **28**(11): p. 1171-1195.
90. Flekkoy, E.G., *Lattice Bhatnagar-Gross-Krook Models for Miscible Fluids.* Physical Review E, 1993. **47**(6): p. 4247-4257.
91. Warren, P.B., *Electroviscous transport problems via lattice-Boltzmann.* International Journal of Modern Physics C, 1997. **8**(4): p. 889-898.

92. Wang, M., et al., *Electrokinetic pumping effects of charged porous media in microchannels using the lattice Poisson-Boltzmann method.* Journal of Colloid and Interface Science, 2006. **304**(1): p. 246-253.
93. Qiao, R. and N.R. Aluru, *Ion concentrations and velocity profiles in nanochannel electroosmotic flows.* Journal of Chemical Physics, 2003. **118**(10): p. 4692-4701.
94. Nicholls, A. and B. Honig, *A Rapid Finite-Difference Algorithm, Utilizing Successive over-Relaxation to Solve the Poisson-Boltzmann Equation.* Journal of Computational Chemistry, 1991. **12**(4): p. 435-445.
95. Goodenough, J.B. and K.S. Park, *The Li-Ion Rechargeable Battery: A Perspective.* Journal of the American Chemical Society, 2013. **135**(4): p. 1167-1176.
96. Chen, J.J., *Recent Progress in Advanced Materials for Lithium Ion Batteries.* Materials, 2013. **6**(1): p. 156-183.
97. Lee, H., et al., *A review of recent developments in membrane separators for rechargeable lithium-ion batteries.* Energy & Environmental Science, 2014. **7**(12): p. 3857-3886.
98. Agubra, V. and J. Fergus, *Lithium Ion Battery Anode Aging Mechanisms.* Materials, 2013. **6**(4): p. 1310-1325.
99. Li, Z., et al., *A review of lithium deposition in lithium-ion and lithium metal secondary batteries.* Journal of Power Sources, 2014. **254**: p. 168-182.
100. Ding, F., et al., *Dendrite-Free Lithium Deposition via Self-Healing Electrostatic Shield Mechanism.* Journal of the American Chemical Society, 2013. **135**(11): p. 4450-4456.
101. Lu, Y.Y., Z.Y. Tu, and L.A. Archer, *Stable lithium electrodeposition in liquid and nanoporous solid electrolytes.* Nature Materials, 2014. **13**(10): p. 961-969.
102. Shin, W.K., A.G. Kannan, and D.W. Kim, *Effective Suppression of Dendritic Lithium Growth Using an Ultrathin Coating of Nitrogen and Sulfur Codoped Graphene Nanosheets on Polymer Separator for Lithium Metal Batteries.* Acs Applied Materials & Interfaces, 2015. **7**(42): p. 23700-23707.
103. Zheng, G.Y., et al., *Interconnected hollow carbon nanospheres for stable lithium metal anodes.* Nature Nanotechnology, 2014. **9**(8): p. 618-623.
104. Yan, K., et al., *Ultrathin Two-Dimensional Atomic Crystals as Stable Interfacial Layer for Improvement of Lithium Metal Anode.* Nano Letters, 2014. **14**(10): p. 6016-6022.
105. Yang, C.-P., et al., *Accommodating lithium into 3D current collectors with a submicron skeleton towards long-life lithium metal anodes.* Nat Commun, 2015. **6**.
106. Monroe, C. and J. Newman, *The effect of interfacial deformation on electrodeposition kinetics.* Journal of the Electrochemical Society, 2004. **151**(6): p. A880-A886.
107. Mcintyre, J.D.E., S. Nakahara, and W.F. Peck, *Electrodeposition of Gold - Nucleation Enhancement and Morphological-Changes Induced by Trace Heavy-Metal Ions.* Journal of the Electrochemical Society, 1978. **125**(3): p. C172-C172.
108. Wijenberg, J.H.O.J., et al., *On the Rate-Equation of Nucleation and the Concept of Active-Sites in Electrodeposition.* Journal of Electroanalytical Chemistry, 1988. **256**(1): p. 1-10.
109. Grujicic, D. and B. Pesic, *Electrodeposition of copper: the nucleation mechanisms.* Electrochimica Acta, 2002. **47**(18): p. 2901-2912.
110. Hyde, M.E., O.V. Klymenko, and R.G. Compton, *The theory of electrodeposition in the presence of forced convection: transport controlled nucleation of hemispheres.* Journal of Electroanalytical Chemistry, 2002. **534**(1): p. 13-17.

111. Zheng, M. and A.C. West, *Simulation of the influence of reactant depletion on nucleation rate in electrodeposition.* Journal of the Electrochemical Society, 2004. **151**(7): p. C502-C507.
112. Stephens, R.M., M. Willis, and R.C. Alkire, *Additive-Assisted Nucleation and Growth by Electrodeposition II. Mathematical Model and Comparison with Experimental Data.* Journal of the Electrochemical Society, 2009. **156**(10): p. D385-D394.
113. Willis, M. and R. Alkire, *Additive-Assisted Nucleation and Growth by Electrodeposition I. Experimental Studies with Copper Seed Arrays on Gold Films.* Journal of the Electrochemical Society, 2009. **156**(10): p. D377-D384.
114. nnLai, S.C.S., et al., *Nucleation, aggregative growth and detachment of metal nanoparticles during electrodeposition at electrode surfaces.* Chemical Science, 2015. **6**(2): p. 1126-1138.
115. Shyu, J.H. and U. Landau, *Dendrite Propagation in Electrodeposition - an Analytical Model.* Journal of the Electrochemical Society, 1980. **127**(8): p. C382-C382.
116. Argoul, F., A. Arneodo, and G. Grasseau, *Self-Similarity of Diffusion-Limited Aggregates and Electrodeposition Clusters.* Physical Review Letters, 1988. **61**(22): p. 2558-2561.
117. Argoul, F., et al., *Self-Similarity of Diffusion-Limited Aggregates and Electrodeposition Clusters - Reply.* Physical Review Letters, 1989. **63**(12): p. 1323-1323.
118. Li, G., L.M. Sander, and P. Meakin, *Self-Similarity of Diffusion-Limited Aggregates and Electrodeposition Clusters - Comment.* Physical Review Letters, 1989. **63**(12): p. 1322-1322.
119. Kahanda, G.L.M.K.S., et al., *Columnar Growth and Kinetic Roughening in Electrochemical Deposition.* Physical Review Letters, 1992. **68**(25): p. 3741-3744.
120. Livermore, C. and P.Z. Wong, *Convection and Turbulence Effects in Strongly Driven Electrochemical Deposition.* Physical Review Letters, 1994. **72**(24): p. 3847-3850.
121. Wang, M., et al., *Formation of a Mesh-Like Electrodeposit Induced by Electroconvection.* Nature, 1994. **367**(6462): p. 438-441.
122. Huang, W.G. and D.B. Hibbert, *Modeling of Metal Electrodeposits - Analytical Solutions.* Physical Review E, 1995. **52**(5): p. 5065-5069.
123. Fleury, V., J.N. Chazalviel, and M. Rosso, *Coupling of Drift, Diffusion, and Electroconvection, in the Vicinity of Growing Electrodeposits.* Physical Review E, 1993. **48**(2): p. 1279-1295.
124. Fleury, V., J. Kaufman, and B. Hibbert, *Evolution of the Space-Charge Layer during Electrochemical Deposition with Convection.* Physical Review E, 1993. **48**(5): p. 3831-3840.
125. Ustarroz, J., et al., *A Generalized Electrochemical Aggregative Growth Mechanism.* Journal of the American Chemical Society, 2013. **135**(31): p. 11550-11561.
126. Chazalviel, J.N., *Electrochemical Aspects of the Generation of Ramified Metallic Electrodeposits.* Physical Review A, 1990. **42**(12): p. 7355-7367.
127. Brissot, C., et al., *Dendritic growth mechanisms in lithium/polymer cells.* Journal of Power Sources, 1999. **81**: p. 925-929.
128. Brissot, C., et al., *Concentration measurements in lithium/polymer-electrolyte/lithium cells during cycling.* Journal of Power Sources, 2001. **94**(2): p. 212-218.
129. Rosso, M., *Electrodeposition from a binary electrolyte: new developments and applications.* Electrochimica Acta, 2007. **53**(1): p. 250-256.

130. Monroe, C. and J. Newman, *Dendrite growth in lithium/polymer systems - A propagation model for liquid electrolytes under galvanostatic conditions.* Journal of the Electrochemical Society, 2003. **150**(10): p. A1377-A1384.
131. Monroe, C. and J. Newman, *The impact of elastic deformation on deposition kinetics at lithium/polymer interfaces.* Journal of the Electrochemical Society, 2005. **152**(2): p. A396-A404.
132. Ely, D.R. and R.E. Garcia, *Heterogeneous Nucleation and Growth of Lithium Electrodeposits on Negative Electrodes.* Journal of the Electrochemical Society, 2013. **160**(4): p. A662-A668.
133. Liao, X.Z., et al., *High-pressure torsion-induced grain growth in electrodeposited nanocrystalline Ni.* Applied Physics Letters, 2006. **88**(2).
134. Schiotz, J., *Strain-induced coarsening in nanocrystalline metals under cyclic deformation.* Mater. Sci. Eng. A, 2004. **375**: p. 975–979.
135. Guymon, C.G., et al., *MPSA effects on copper electrodeposition investigated by molecular dynamics simulations.* Journal of Chemical Physics, 2008. **128**(4).
136. S. Nishimura, Y.K., Y. Hiwatari, K. Ohara and F. Asa, *Molecular Simulation Approach to the Effects of Additives in Electrodeposition Process.* ECS Transactions, 2009. **16**(46): p. 83-92.
137. Kaneko, Y., et al., *Computer simulation of electrodeposition: hybrid of molecular dynamics and Monte Carlo.* Molecular Simulation, 2005. **31**(6-7): p. 429-433.
138. Hiwatari, Y., et al., *Molecular dynamics-Monte Carlo hybrid simulation of thin film growth and void formation in electrodeposition process.* Molecular Simulation, 2007. **33**(1-2): p. 133-138.
139. Kaneko, Y., et al., *Monte Carlo and Molecular Dynamics Studies of the Effects of Additives in Electrodeposition.* Journal of the Korean Physical Society, 2009. **54**(3): p. 1207-1211.
140. Ohwaki, T., et al., *Large-scale first-principles molecular dynamics for electrochemical systems with O(N) methods.* Journal of Chemical Physics, 2012. **136**(13).
141. M. P. Allen, D.J.T., *Computer Simulation of Liquids*. 1990: New York Press.
142. A. C. Frank, E.P.M.L., and P. T. A. Sumodjo, *A Monte Carlo Model for the Simulation of the Electrodeposition of CoNi Alloys onto Glassy Carbon.* ECS Transactions, 2010. **25**(34): p. 53-63.
143. Drews, T.O., et al., *Stochastic simulation of the early stages of kinetically limited electrodeposition.* Journal of the Electrochemical Society, 2006. **153**(6): p. C434-C441.
144. Li, X.H., et al., *Effect of additives on shape evolution during electrodeposition I. Multiscale simulation with dynamically coupled kinetic Monte Carlo and moving-boundry finite-volume codes.* Journal of the Electrochemical Society, 2007. **154**(4): p. D230-D240.
145. Pricer, T.J., M.J. Kushner, and R.C. Alkire, *Monte Carlo simulation of the electrodeposition of copper - I. Additive-free acidic sulfate solution.* Journal of the Electrochemical Society, 2002. **149**(8): p. C396-C405.
146. Emekli, U. and A.C. West, *Simulation of the Effect of Additives on Electrochemical Nucleation.* Journal of the Electrochemical Society, 2010. **157**(9): p. D479-D485.
147. Haataja, M., D.J. Srolovitz, and A.B. Bocarsly, *Morphological stability during electrodeposition - II. Additive effects.* Journal of the Electrochemical Society, 2003. **150**(10): p. C708-C716.

148. Haataja, M., D.J. Srolovitz, and A.B. Bocarsly, *Morphological stability during electrodeposition - I. Steady states and stability analysis.* Journal of the Electrochemical Society, 2003. **150**(10): p. C699-C707.
149. Perko, J. and R.A. Patel, *Single-relaxation-time lattice Boltzmann scheme for advection-diffusion problems with large diffusion-coefficient heterogeneities and high-advection transport.* Physical Review E, 2014. **89**(5).
150. Chopard, B., J.L. Falcone, and J. Latt, *The lattice Boltzmann advection-diffusion model revisited.* European Physical Journal-Special Topics, 2009. **171**: p. 245-249.
151. Shi, B.C., et al., *A new scheme for source term in LBGK model for convection-diffusion equation.* Computers & Mathematics with Applications, 2008. **55**(7): p. 1568-1575.
152. Sun, D.K., et al., *Lattice Boltzmann modeling of dendritic growth in forced and natural convection.* Computers & Mathematics with Applications, 2011. **61**(12): p. 3585-3592.
153. Sun, D.K., et al., *Lattice Boltzmann modeling of dendritic growth in a forced melt convection.* Acta Materialia, 2009. **57**(6): p. 1755-1767.
154. Yin, H., S.D. Felicelli, and L. Wang, *Simulation of a dendritic microstructure with the lattice Boltzmann and cellular automaton methods.* Acta Materialia, 2011. **59**(8): p. 3124-3136.
155. Hsu, C.C. and H. Eyring, *Significant Structure Theory of Surface-Tension of Alkali-Metals.* Proceedings of the National Academy of Sciences of the United States of America, 1972. **69**(5): p. 1125-&.
156. J. L. Barton, J.O.M.B., *The Electrolytic Growth of Dendrites from Ionic Solutions.* Proc. R. Soc. Lond., 1962. **268**.
157. Vitos, L., et al., *The surface energy of metals.* Surface Science, 1998. **411**(1-2): p. 186-202.
158. Beltran-Sanchez, L. and D.M. Stefanescu, *A quantitative dendrite growth model and analysis of stability concepts.* Metallurgical and Materials Transactions a-Physical Metallurgy and Materials Science, 2004. **35A**(8): p. 2471-2485.
159. Hoffman, J.D., *Relationship between the Truncation Errors of Centered Finite-Difference Approximations on Uniform and Nonuniform Meshes.* Journal of Computational Physics, 1982. **46**(3): p. 469-474.
160. Ravdel, B., et al. *Temperature dependence of the conductivity of lithium-ion battery electrolytes*. 2003.
161. Valoen, L.O. and J.N. Reimers, *Transport properties of LiPF6-based Li-ion battery electrolytes.* Journal of the Electrochemical Society, 2005. **152**(5): p. A882-A891.
162. Kufian, M.Z. and S.R. Majid, *Performance of lithium-ion cells using 1 M LiPF6 in EC/DEC (v/v=1/2) electrolyte with ethyl propionate additive.* Ionics, 2010. **16**(5): p. 409-416.
163. Sawada, Y., A. Dougherty, and J.P. Gollub, *Dendritic and Fractal Patterns in Electrolytic Metal Deposits.* Physical Review Letters, 1986. **56**(12): p. 1260-1263.
164. Fleury, V., *Branched fractal patterns in non-equilibrium electrochemical deposition from oscillatory nucleation and growth.* Nature, 1997. **390**(6656): p. 145-148.
165. Liu, S., et al., *Lithium Dendrite Formation in Li/Poly(ethylene oxide)-Lithium Bis(trifluoromethanesulfonyl)imide and N-Methyl-N-propylpiperidinium Bis(trifluoromethanesulfonyl)imide/Li Cells.* Journal of the Electrochemical Society, 2010. **157**(10): p. A1092-A1098.

166. Rosso, M., et al., *Onset of current-driven concentration instabilities in thin cell electrodeposition with small inter-electrode distance.* Electrochimica Acta, 2002. **47**(8): p. 1267-1273.
167. Safari, M. and C. Delacourt, *Modeling of a Commercial Graphite/LiFePO4 Cell.* Journal of the Electrochemical Society, 2011. **158**(5): p. A562-A571.
168. Goriparti, S., et al., *Review on recent progress of nanostructured anode materials for Li-ion batteries.* Journal of Power Sources, 2014. **257**: p. 421-443.
169. de las Casas, C. and W.Z. Li, *A review of application of carbon nanotubes for lithium ion battery anode material.* Journal of Power Sources, 2012. **208**: p. 74-85.
170. Etacheri, V., et al., *Challenges in the development of advanced Li-ion batteries: a review.* Energy & Environmental Science, 2011. **4**(9): p. 3243-3262.
171. Aurbach, D., et al., *A short review of failure mechanisms of lithium metal and lithiated graphite anodes in liquid electrolyte solutions.* Solid State Ionics, 2002. **148**(3-4): p. 405-416.
172. Piao, T., et al., *Intercalation of lithium ions into graphite electrodes studied by AC impedance measurements.* Journal of the Electrochemical Society, 1999. **146**(8): p. 2794-2798.
173. Yoon, S., et al., *Enhanced cyclability and surface characteristics of lithium batteries by Li-Mg co-deposition and addition of HF acid in electrolyte.* Electrochimica Acta, 2008. **53**(5): p. 2501-2506.
174. Matsuda, Y., *Behavior of Lithium Electrolyte Interface in Organic Solutions.* Journal of Power Sources, 1993. **43**(1-3): p. 1-7.
175. Park, G., et al., *The important role of additives for improved lithium ion battery safety.* Journal of Power Sources, 2009. **189**(1): p. 602-606.
176. Zhang, S.S., *A review on electrolyte additives for lithium-ion batteries.* Journal of Power Sources, 2006. **162**(2): p. 1379-1394.
177. Rejovitzky, E., C.V. Di Leo, and L. Anand, *A theory and a simulation capability for the growth of a solid electrolyte interphase layer at an anode particle in a Li-ion battery.* Journal of the Mechanics and Physics of Solids, 2015. **78**: p. 210-230.
178. Doyle, M., T.F. Fuller, and J. Newman, *Modeling of Galvanostatic Charge and Discharge of the Lithium Polymer Insertion Cell.* Journal of the Electrochemical Society, 1993. **140**(6): p. 1526-1533.
179. Darling, R. and J. Newman, *Modeling side reactions in composite LiyMn2O4 electrodes.* Journal of the Electrochemical Society, 1998. **145**(3): p. 990-998.
180. Arora, P., M. Doyle, and R.E. White, *Mathematical modeling of the lithium deposition overcharge reaction in lithium-ion batteries using carbon-based negative electrodes.* Journal of the Electrochemical Society, 1999. **146**(10): p. 3543-3553.
181. Verbrugge, M.W. and B.J. Koch, *Electrochemical analysis of lithiated graphite anodes.* Journal of the Electrochemical Society, 2003. **150**(3): p. A374-A384.
182. Doyle, M. and Y. Fuentes, *Computer simulations of a lithium-ion polymer battery and implications for higher capacity next-generation battery designs.* Journal of the Electrochemical Society, 2003. **150**(6): p. A706-A713.
183. Gu, W.B. and C.Y. Wang, *Thermal-electrochemical modeling of battery systems.* Journal of the Electrochemical Society, 2000. **147**(8): p. 2910-2922.
184. Smith, M., R.E. Garcia, and Q.C. Horn, *The Effect of Microstructure on the Galvanostatic Discharge of Graphite Anode Electrodes in LiCoO2-Based Rocking-Chair*

Rechargeable Batteries. Journal of the Electrochemical Society, 2009. **156**(11): p. A896-A904.
185. Chirkov, Y.G., V.I. Rostokin, and A.M. Skundin, *Computer Modeling of Negative Electrode Operation in Lithium-Ion Battery: Model of Equal-Sized Grains, Galvanostatic Discharge Mode, Calculation of Characteristic Parameters.* Russian Journal of Electrochemistry, 2011. **47**(1): p. 59-70.
186. Harris, S.J., E.K. Rahani, and V.B. Shenoy, *Direct In Situ Observation and Numerical Simulations of Non-Shrinking-Core Behavior in an MCMB Graphite Composite.* Journal of the Electrochemical Society, 2012. **159**(9): p. A1501-A1507.
187. Zadin, V., et al., *Finite element modelling of ion transport in the electrolyte of a 3D-microbattery.* Solid State Ionics, 2011. **192**(1): p. 279-283.
188. Yi, Y.B., C.W. Wang, and A.M. Sastry, *Two-dimensional vs. three-dimensional clustering and percolation in fields of overlapping ellipsoids.* Journal of the Electrochemical Society, 2004. **151**(8): p. A1292-A1300.
189. Zhang, X.C., A.M. Sastry, and W. Shyy, *Intercalation-induced stress and heat generation within single lithium-ion battery cathode particles.* Journal of the Electrochemical Society, 2008. **155**(7): p. A542-A552.
190. Zadin, V., et al., *Finite element simulations of 3D ionic transportation properties in Li-ion electrolytes.* Electrochimica Acta, 2012. **65**: p. 165-173.
191. Zhang, X.C., W. Shyy, and A.M. Sastry, *Numerical simulation of intercalation-induced stress in Li-ion battery electrode particles.* Journal of the Electrochemical Society, 2007. **154**(10): p. A910-A916.
192. Latz, A. and J. Zausch, *Multiscale modeling of lithium ion batteries: thermal aspects.* Beilstein Journal of Nanotechnology, 2015. **6**: p. 987-1007.
193. Guo, Z.L. and T.S. Zhao, *Lattice Boltzmann model for incompressible flows through porous media.* Physical Review E, 2002. **66**(3).
194. Kang, Q.J., P.C. Lichtner, and D.X. Zhang, *An improved lattice Boltzmann model for multicomponent reactive transport in porous media at the pore scale.* Water Resources Research, 2007. **43**(12).
195. Karthikeyan, D.K., G. Sikha, and R.E. White, *Thermodynamic model development for lithium intercalation electrodes.* Journal of Power Sources, 2008. **185**(2): p. 1398-1407.
196. Ramasamy, R.P., J.W. Lee, and B.N. Popov, *Simulation of capacity loss in carbon electrode for lithium-ion cells during storage.* Journal of Power Sources, 2007. **166**(1): p. 266-272.
197. Persson, K., et al., *Thermodynamic and kinetic properties of the Li-graphite system from first-principles calculations.* Physical Review B, 2010. **82**(12).
198. Stephenson, D.E., et al., *Modeling 3D Microstructure and Ion Transport in Porous Li-Ion Battery Electrodes.* Journal of the Electrochemical Society, 2011. **158**(7): p. A781-A789.
199. Yu, P., et al., *Determination of the lithium ion diffusion coefficient in graphite.* Journal of the Electrochemical Society, 1999. **146**(1): p. 8-14.
200. Persson, K., et al., *Lithium Diffusion in Graphitic Carbon.* Journal of Physical Chemistry Letters, 2010. **1**(8): p. 1176-1180.
201. Prausnitz, M.R. and R. Langer, *Transdermal drug delivery.* Nature Biotechnology, 2008. **26**(11): p. 1261-1268.
202. Wiedersberg, S. and R.H. Guy, *Transdermal drug delivery: 30+years of war and still fighting!* Journal of Controlled Release, 2014. **190**: p. 150-156.

203. Jepps, O.G., et al., *Modeling the human skin barrier - Towards a better understanding of dermal absorption.* Advanced Drug Delivery Reviews, 2013. **65**(2): p. 152-168.
204. Lim, P.F.C., X.Y. Liu, and S.Y. Chan, *A Review on Terpenes as Skin Penetration Enhancers in Transdermal Drug Delivery.* Journal of Essential Oil Research, 2009. **21**(5): p. 423-428.
205. Benson, H.A.E., *Transdermal Drug Delivery: Penetration Enhancement Techniques.* Current Drug Delivery, 2005. **2**: p. 11.
206. Prausnitz, M.R., S. Mitragotri, and R. Langer, *Current status and future potential of transdermal drug delivery.* Nature Reviews Drug Discovery, 2004. **3**(2): p. 115-124.
207. Prausnitz, M.R., *Microneedles for transdermal drug delivery.* Advanced Drug Delivery Reviews, 2004. **56**(5): p. 581-587.
208. Sharma, A., et al., *Transdermal drug delivery using electroporation. II. Factors influencing skin reversibility in electroporative delivery of terazosin hydrochloride in hairless rats.* Journal of Pharmaceutical Sciences, 2000. **89**(4): p. 536-544.
209. Sharma, A., et al., *Transdermal drug delivery using electroporation. I. Factors influencing in vitro delivery of terazosin hydrochloride in hairless rats.* Journal of Pharmaceutical Sciences, 2000. **89**(4): p. 528-535.
210. Tashiro, Y., et al., *Iontophoretic transdermal delivery of ketoprofen: Effect of iontophoresis on drug transfer from skin to cutaneous blood.* Biological & Pharmaceutical Bulletin, 2000. **23**(12): p. 1486-1490.
211. Tashiro, Y., et al., *Iontophoretic transdermal delivery of ketoprofen: Novel method for the evaluation of plasma drug concentration in cutaneous vein.* Biological & Pharmaceutical Bulletin, 2000. **23**(5): p. 632-636.
212. Asbill, C.S., A.F. El-Kattan, and B. Michniak, *Enhancement of transdermal drug delivery: Chemical and physical approaches.* Critical Reviews in Therapeutic Drug Carrier Systems, 2000. **17**(6): p. 621-658.
213. Lahiji, S.F., M. Dangol, and H. Jung, *A patchless dissolving microneedle delivery system enabling rapid and efficient transdermal drug delivery.* Scientific Reports, 2015. **5**.
214. Sanz, R., et al., *Enhancing Topical Analgesic Administration: Review and Prospect for Transdermal and Transbuccal Drug Delivery Systems.* Current Pharmaceutical Design, 2015. **21**(20): p. 2867-2882.
215. Zorec, B., et al., *Ultrasound and electric pulses for transdermal drug delivery enhancement: Ex vivo assessment of methods with in vivo oriented experimental protocols.* International Journal of Pharmaceutics, 2015. **490**(1-2): p. 65-73.
216. Herman, A. and A.P. Herman, *Essential oils and their constituents as skin penetration enhancer for transdermal drug delivery: a review.* Journal of Pharmacy and Pharmacology, 2015. **67**(4): p. 473-485.
217. Otto, D.P. and M.M. de Villiers, *The Experimental Evaluation and Molecular Dynamics Simulation of a Heat-Enhanced Transdermal Delivery System.* Aaps Pharmscitech, 2013. **14**(1): p. 111-120.
218. Casciola, M., et al., *A molecular dynamic study of cholesterol rich lipid membranes: comparison of electroporation protocols.* Bioelectrochemistry, 2014. **100**: p. 11-17.
219. Huzil, J.T., et al., *Drug delivery through the skin: molecular simulations of barrier lipids to design more effective noninvasive dermal and transdermal delivery systems for small molecules, biologics, and cosmetics.* Wiley Interdisciplinary Reviews-Nanomedicine and Nanobiotechnology, 2011. **3**(5): p. 449-462.

220. Notman, R. and J. Anwar, *Breaching the skin barrier - Insights from molecular simulation of model membranes.* Advanced Drug Delivery Reviews, 2013. **65**(2): p. 237-250.
221. Rim, J.E., P.M. Pinsky, and W.W. van Osdol, *Multiscale Modeling Framework of Transdermal Drug Delivery.* Annals of Biomedical Engineering, 2009. **37**(6): p. 1217-1229.
222. Couto, A., et al., *Dermic diffusion and stratum corneum: A state of the art review of mathematical models.* Journal of Controlled Release, 2014. **177**: p. 74-83.
223. Anissimov, Y.G., et al., *Mathematical and pharmacokinetic modelling of epidermal and dermal transport processes.* Advanced Drug Delivery Reviews, 2013. **65**(2): p. 169-190.
224. Rim, J.E., P.M. Pinsky, and W.W. van Osdol, *Using the method of homogenization to calculate the effective diffusivity of the stratum corneum.* Journal of Membrane Science, 2007. **293**(1-2): p. 174-182.
225. Wang, T.F., G.B. Kasting, and J.M. Nitsche, *A multiphase microscopic diffusion model for stratum corneum permeability. II. Estimation of physicochemical parameters, and application to a large permeability database.* Journal of Pharmaceutical Sciences, 2007. **96**(11): p. 3024-3051.
226. Rim, J.E., P.M. Pinsky, and W.W. van Osdol, *Using the method of homogenization to calculate the effective diffusivity of the stratum corneum with permeable corneocytes.* Journal of Biomechanics, 2008. **41**(4): p. 788-796.
227. Mitragotri, S., et al., *Mathematical models of skin permeability: An overview.* International Journal of Pharmaceutics, 2011. **418**(1): p. 115-129.
228. Chen, L.J., G.P. Lian, and L.J. Han, *Use of "bricks and mortar" model to predict transdermal permeation: Model development and initial validation.* Industrial & Engineering Chemistry Research, 2008. **47**(17): p. 6465-6472.
229. Wang, T.F., G.B. Kasting, and J.M. Nitsche, *A multiphase microscopic diffusion model for stratum corneum permeability. I. Formulation, solution, and illustrative results for representative compounds.* Journal of Pharmaceutical Sciences, 2006. **95**(3): p. 620-648.
230. Rim, J.E., P.M. Pinsky, and W.W. van Osdol, *Finite element modeling of coupled diffusion with partitioning in transdermal drug delivery.* Annals of Biomedical Engineering, 2005. **33**(10): p. 1422-1438.
231. Anissimov, Y.G. and M.S. Roberts, *Diffusion modeling of percutaneous absorption kinetics: 2. Finite vehicle volume and solvent deposited solids.* Journal of Pharmaceutical Sciences, 2001. **90**(4): p. 504-520.
232. Guy, R.H. and J. Hadgraft, *A Theoretical Description Relating Skin Penetration to the Thickness of the Applied Medicament.* International Journal of Pharmaceutics, 1980. **6**(3-4): p. 321-332.
233. Frederick Frasch, H., *A Random Walk Model of Skin Permeation.* Risk Analysis, 2002. **22**(2): p. 265-276.
234. Tang, G.H., et al., *Electroosmotic flow and mixing in microchannels with the lattice Boltzmann method.* Journal of Applied Physics, 2006. **100**(9).
235. Hlushkou, D., D. Kandhai, and U. Tallarek, *Coupled lattice-Boltzmann and finite-difference simulation of electroosmosis in microfluidic channels.* International Journal for Numerical Methods in Fluids, 2004. **46**(5): p. 507-532.
236. Medvedev, D. and K. Kassner, *Lattice-Boltzmann scheme for dendritic growth in presence of convection.* Journal of Crystal Growth, 2005. **275**(1-2): p. E1495-E1500.

237. Qinjun Kang1, Peter C. Lichtner1 and David R. Janecky, *Lattice Boltzmann Method for Reacting Flows in Porous Media.* Advances in Applied Mathematics and Mechanics, 2010. **2**(5): p. 9.
238. Ayodele, S.G., D. Raabe, and F. Varnik, *Lattice Boltzmann Modeling of Advection-Diffusion-Reaction Equations: Pattern Formation Under Uniform Differential Advection.* Communications in Computational Physics, 2013. **13**(3): p. 741-756.
239. Yoshida, H. and M. Nagaoka, *Multiple-relaxation-time lattice Boltzmann model for the convection and anisotropic diffusion equation.* Journal of Computational Physics, 2010. **229**(20): p. 7774-7795.
240. Mohamad, A.A., *Lattice Boltzmann Method - Fundamentals and Engineering Applications with Computer Codes*. 2011: Springer.